

UCLA

UCLA Electronic Theses and Dissertations

Title

Towards High-Efficiency and Stable Metal Halide Perovskite Solar Cells: from Interior to Exterior

Permalink

<https://escholarship.org/uc/item/28r480v6>

Author

Zhao, Yepin

Publication Date

2021

Peer reviewed|Thesis/dissertation

UNIVERSITY OF CALIFORNIA

LOS ANGELES

Towards High-Efficiency and Stable Metal Halide Perovskite Solar Cells:

from Interior to Exterior

A dissertation submitted in partial satisfaction of the requirements

for the degree Doctor of Philosophy

in Materials Science and Engineering

by

Yepin Zhao

2021

© Copyright by

Yepin Zhao

2021

ABSTRACT OF THE DISSERTATION

Towards High-Efficiency and Stable Metal Halide Perovskite Solar Cells:

from Interior to Exterior

by

Yepin Zhao

Doctor of Philosophy in Materials Science and Engineering

University of California, Los Angeles, 2021

Professor Yang Yang, Chair

Metal halide perovskite solar cells have proven themselves as one of the most promising candidates to replace the currently well-commercialized silicon based solar cells. Because of its unique energy band structure, it has merits such as high defect-tolerance, favorable charge carrier mobility, and high absorption coefficient. However, the major issue that hinders the successful real-life application of the metal halide perovskite solar cell is its unsatisfactory stability. In Chapter One, I introduce the four basic elements that causing the instability of perovskite solar cells: light, heat, bias, and moisture. The perovskite material degradation mechanism behind each environment will be detailly illustrated. Ion migration suppression and device encapsulation can be regarded as the main

solutions to enhance the operational lifetime of the perovskite solar cells. From interior to exterior, in the following chapters, I introduce the strategies we developed that are proven to be powerful to improve the stability of the metal halide perovskite solar cells.

In Chapter Two, I introduce the first strategy of interior multivalent interstitial doping. It is a strategy originated inside the perovskite lattice. Cations with suitable sizes to occupy an interstitial site of perovskite crystals have been widely used to inhibit ion migration and promote performance and stability of perovskite optoelectronics. However, the interstitial doping accompanies inevitable lattice strain to impair long-range ordering and stability of the crystals to cause a sacrificial trade-off. In this chapter, I unravel the evident influence of the valence states of the interstitial cations on their efficacy to suppress the ion migration. Incorporation of a trivalent neodymium cation (Nd^{3+}) effectively mitigates the ion migration in the perovskite lattice with significantly reduced dosage (0.08%) compared to a widely used monovalent cation dopant (Na^+ , 0.45%). Less but better, the prototypical perovskite solar cells incorporated with Nd^{3+} exhibits significantly enhanced photovoltaic performance and operational stability.

In Chapter Three, I discuss the defect passivation of the perovskite crystal, which constitutes one of the most commonly used strategies to fabricate highly efficient perovskite solar cells (PSCs). The durability of the passivation effects under harsh operational conditions has not been extensively studied regardless of the weak and vulnerable secondary bonding between the molecular passivation agents and perovskite crystals. Here, we incorporated strategically designed passivating agents to investigate the effect of their interaction energies with the perovskite crystals and correlated these with the performance and longevity of the passivation effects. We unraveled that the passivation agents with a stronger interaction energy are advantageous not only for effective defect passivation,

but also to suppress defect migration. The prototypical PSCs treated with the optimal passivation agent exhibited superior performance and operational stability, retaining 81.9% and 85.3% of their initial performance under continuous illumination or nitrogen at 85 °C after 1008 hours, respectively while the reference device completely degraded during the time. This work provides important insights into designing operationally durable defect passivation agents for perovskite optoelectronic devices.

In Chapter Four, we focus on the perovskite grain and the grain boundary density. Intrinsically, detrimental defects accumulating at the surface and grain boundaries limit both the performance and stability of perovskite solar cells. Small molecules and bulkier polymers with functional groups are utilized to passivate these ionic defects but usually suffer from volatility and precipitation issues, respectively. Starting from the addition of small monomers in PbI_2 precursor, in this chapter, I introduce a polymerization-assisted grain growth (PAGG) strategy in the sequentially deposited method. With a polymerization process triggered during the PbI_2 film annealing, the bulkier polymers formed will be adhered to the grain boundaries, remaining the previously established interactions with PbI_2 . After perovskite formation, the polymers anchored on the boundaries can effectively passivate under-coordinated lead ions and reduce defect density. As a result, we obtain a champion power conversion efficiency (PCE) of 23.0%, together with a prolonged lifetime where 85.7% and 91.8% of the initial PCE remains after 504-hour continuous illumination and 2208-hour shelf storage, respectively.

In Chapter Five, I will go to the exterior of the perovskite solar cell and introduce a novel strategy of device encapsulation. Unstable nature against moisture is one of the major issues of metallic halide perovskite solar cell application. Thin-film encapsulation is known as a powerful

approach to notably enhance the operational stability of perovskite solar cells in humid environment. However, encapsulation layers with ideal gas barrier performance always require harsh fabrication conditions with high temperature and harmful precursors. For this reason, here we provide a mild encapsulation strategy to maintain the original performance of solar cell devices by utilization of ethylene glycol-induced immediate layer to minimize the damage of plasma-enhanced atomic layer deposition to perovskite solar cells. The organic-inorganic alternating encapsulation structure has exhibited a water vapor transmittance rate of $1.3 \times 10^{-5} \text{ g} \cdot \text{m}^{-2} \cdot \text{day}^{-1}$, which is the lowest value among the reported thin film encapsulation layers of perovskite solar cells. Our perovskite solar cells have survived at 80% relative humidity and 30 °C for over 2000 hours while preserving 96% of its initial performance.

The dissertation of Yepin Zhao is approved.

Yu Huang

Yunfeng Lu

Raman Aaswath Pattabhi

Yang Yang, Committee Chair

University of California, Los Angeles

2021

Table of Contents

Chapter 1 Introduction to the stability issues of perovskite solar cells.....	1
1.1 Current status of perovskite solar cells	1
1.2 Challenges of the perovskite solar cells	2
1.3 The four elements of perovskite solar cell instability	3
1.4 The major mechanism of perovskite photovoltaic instability and solution principles.....	5
References	6
Chapter 2 Interior multivalent interstitial doping	20
2.1 Introduction of the interior interstitial doping.....	20
2.2 The multivalent interstitial doping strategy	21
2.3 Strong interaction between the defects and the multivalent interstitial dopants	23
2.4 Impeded ion migration by multivalent interstitial doping.....	25
References	27
Chapter 3 Passivation of the charged defect with rational additive selection.....	36
3.1 Introduction of the charged defect passivation.....	36
3.2 Investigation of molecular interactions between additives and defects	37
3.3 Defect passivation effect based on the different additives	40
3.4 Photovoltaic performances of perovskite solar cells with the additives	42
3.5 Operational and thermal stability correlated with ion migration energetics	43

3.5 Summary and conclusion	45
References	46
Chapter 4 Polymerization-assisted grain growth strategy	59
4.1 Introduction of the polymerization-assisted grain growth (PAGG) strategy	59
4.2 Adduct formation and polymerization process	61
4.3 Intermolecular exchanging grain growth and film properties	63
4.4 Improved photovoltaic performance and stability using the PAGG strategy	64
4.5 Conclusions	66
References	67
Chapter 5 Hermetic Seal for Perovskite Solar Cells: An Improved Plasma Enhanced Atomic Layer Deposition Encapsulation	78
5.1 Introduction of plasma enhanced atomic layer deposition encapsulation	78
5.2. Experimental methods	80
5.3 Damage to perovskite solar cells during encapsulation process	83
5.4 Strategy for the encapsulation of perovskite solar cells	85
5.5 Properties of the encapsulation films	86
5.6 Application of the encapsulation on perovskite solar cells	87
5.7 Conclusions	88
References	89
Appendix A	99

Appendix B 140

List of Figures

Figure 1.1 | NREL Best research cell efficiency chart.

Figure 1.2 | The golden triangle of the solar cell performance.

Figure 1.3 | Comparison between single-junction silicon-based solar cell and single-junction perovskite solar cell.

Figure 1.4 | (A) Schematics of the evolution of the ion distribution within the perovskite layer sandwiched between the electron and hole selective contacts under solar cell working conditions: initial conditions, non-stabilized conditions on the timescale of minutes and the stabilized condition on the timescale of hours. (B) The evaporation mechanism of the ions in metal-halide perovskite material and the scheme of the degradation of perovskite materials under the sunlight.

Figure 1.5 | (A) Illustration of possible elementary microscopic mechanisms for ion transport mediated by the activated diffusion of charged point defects in perovskites. (B) Vacancy-assisted ion transport along the surface of perovskite. (C) Images of perovskite films heated at different temperatures for 70 min, respectively. (D) STEM-HAADF images of perovskite samples at different stages of heating.

Figure 1.6 | (A) Open circuit voltage of the device recorded after repeated poling by ± 2.5 V bias for more than 750 cycles. (B) In situ monitoring of the material change during the poling process.

Figure 1.7 | (A) Degradation model of perovskite films under partial hydration. (B) Proposed decomposition pathway of perovskite in the presence of a water molecule. (C) Photographs of MAPbI₃ films deposited on glass at different hydration time showing discoloration and AFM measurements.

Figure 1.8 | The consequences of intrinsic ion migration for each component layer in perovskite solar cells.

Figure 1.9 | Illustration of the ion migration pathways.

Figure 2.1 | (A) Theoretical models of iodide ion migration pathway in perovskite lattices without or with Nd^{3+} , Ca^{2+} , or Na^{+} at the interstitial site. (B) Relative energy landscapes of the system during the iodide ion migration. (C) a-FAPbI₃ (100) peaks from the XRD spectra of perovskite films as a function of Nd^{3+} , Ca^{2+} , and Na^{+} doping concentration from 0% to 5%. The arrows indicate a shift of the peak toward lower two theta angle with increasing dopant concentration (D) Comparison of the a-FAPbI₃, d-FAPbI₃, and PbI₂ phase variations from the XRD spectra of films with different Nd^{3+} , Ca^{2+} , and Na^{+} doping concentration.

Figure 2.2 | (A) Statistical PCEs of devices with different concentrations of Nd^{3+} , Ca^{2+} , or Na^{+} incorporation. The optimal concentrations to achieve the highest PCE for each dopant are highlighted. (B) J - V curves, (C) steady-state PCE measurement results and (D) EQE spectra of the best-performing devices for each condition. (E) SEM surface morphology of the perovskite films without or with the optimal cation doping concentration.

Figure 2.3 | (A) Interaction energies of Nd^{3+} , Ca^{2+} , or Na^{+} cations incorporated in the perovskite lattices with the negatively charged defects. (B) Time-resolved PL spectra of perovskite films without or with the optimal cation doping concentrations (insert: corresponding steady-state spectra of perovskite films). (C) Transient photovoltage (TPV) curves of perovskite films without or with the optimal cation doping concentrations. (D) PAS depth-profiling of perovskite films without or with the optimal cation doping concentrations. Solid lines are fitted plots. Shaded areas indicate the top

surface region of the films. (E) Average shape parameters in the bulk region extracted from the PAS measurement (F) tDOS in perovskite solar cells with or without cation incorporation.

Figure 2.4 | (A) Temperature-dependent conductivity of the lateral devices with Nd^{3+} , Ca^{2+} , or Na^{+} incorporations or without cation incorporation. Filled circles are measured data while dashed lines are fitted curves. (B, C) In situ PL images before and after applying an electric field of $150 \text{ mV}/\mu\text{m}$ under 440 nm illumination for 5 and 10 min for the lateral device based on (B) the reference film and (C) the film incorporated with $0.08\% \text{ Nd}^{3+}$. (D) Photo stability of perovskite solar cells without or with the optimal cation doping concentrations. (E) Thermal stability of perovskite solar cells without or with the optimal cation doping concentrations.

Figure 3.1 | Theoretical models of perovskite with molecular surface passivation of V_I defects with **a).** 2-aminoethylphosphonic acid (PA), **d).** hypotaurine (SA), and **g).** β -alanine (CA). FTIR spectra of **b)-c).** pure PA and PbI_2 film with PA, **e)-f).** pure SA and PbI_2 film with SA, and **h)-i).** pure CA and PbI_2 film with CA.

Figure 3.2 | **a)-d).** Atomic force microscopy (AFM) images of perovskite films with or without additives. **e).** Confocal laser scanning fluorescence microscopy (CLSM) images of perovskite films with or without additives. **f).** Time-resolved PL spectra of perovskite films with 2-aminoethylphosphonic acid (PA), hypotaurine (SA) and β -alanine additives (CA) or without additives.

Figure 3.3 | **a).** Space-charge-limited-current (SCLC) measurements of electron-only devices based on perovskite films with 2-aminoethylphosphonic acid (PA), hypotaurine (SA) and β -alanine additives (CA) or without additives. **b).** SCLC measurements of hole-only devices based on

perovskite films with or without additives. **c).** Device configurations of SCLC measurements. **d).** Defect density calculated from SCLC measurement with or without additives.

Figure 3.4 | a). *J-V* curves of perovskite solar cells with 2-aminoethylphosphonic acid (PA), hypotaurine (SA) and β -alanine additives (CA) or without additives under reverse scan direction. **b).** Incident photon-to-electron conversion efficiency (IPCE) curves of perovskite solar cells with or without additives. **c).** Stabilized power outputs (SPOs) of devices with or without additives. **d).** Transient photovoltage (TPV) curves of perovskite films with or without additives. **e).** Defect density calculated from the angular-frequency-dependent capacitance spectra with or without additives. **f).** Nyquist plots of perovskite solar cells with or without additives measured in the dark.

Figure 3.5 | a). Photo stability of perovskite solar cells with 2-aminoethylphosphonic acid (PA), hypotaurine (SA) and β -alanine additives (CA) or without additives. **b).** Thermal stability of perovskite solar cells with or without additives.

Figure 4.1 | Illustration of polymerization-assisted grain growth (PAGG) process and the binding energies between additives and PbI_2 molecules. (a) Schematic illustration of the polymerization-assisted grain growth (PAGG) process. (b-d) computational study of most favorable molecular configurations and binding energies between (b) the PbI_2 molecule and DMSO, (c) the PbI_2 molecules and DI monomer, (d) the PbI_2 molecules and DI dimer.

Figure 4.2 | Confirmation of polymerization process. (a) Fourier transform infrared spectra (FTIR) of the DI monomers, PbI_2 -DI film before and after the polymerization process, and perovskite film after the intermolecular exchanging process. (b,c) Photographs of the pure DI monomers (b) before and (c) after the polymerization process. (d,e) High-resolution transmission electron microscopy (HRTEM) images and Fast Fourier transform (FFT) analysis of the grain areas of the (d) PbI_2 -DI

sample after the polymerization process, and (e) perovskite sample after the intermolecular exchanging process.

Figure 4.3 | Intermolecular exchanging grain growth and film properties. (a) Schematic diagrams of perovskite crystallization kinetics of PbI_2 films without (black) and with (red) PAGG process. (b,c) Confocal laser scanning fluorescence microscopy (CLSM) images of PbI_2 films (b) without and (c) with PAGG process as a function of time (0s, 15s, 20s, 50s) of intermolecular exchanging process. The PbI_2 regions are shown in green while the perovskite phase is shown in red in the images. Scale bars indicate 10 μm . (d,e) Top-view scanning electron microscopy (SEM) images of perovskite film (d) without and (e) with PAGG process. (f) Cross-sectional SEM image of the solar cell device with perovskite film with PAGG process. (g) X-ray diffraction spectra (XRD) of the perovskite films without (black) and with (red) PAGG process. (h) Time-resolved photoluminescence (PL) spectra (Inset: steady-state PL spectra) of the perovskite films without (black) and with (red) PAGG process.

Figure 4.4 | Improved photovoltaic performance and stability using the PAGG strategy. (a) Current density–voltage (J–V) curves of perovskite solar cells without or with PAGG process. (b) IPCE curves of perovskite solar cells without (black) and with (red) PAGG process. (c) Transient photovoltage (TPV) decay of the perovskite solar cells without (black) and with (red) PAGG process. (d) Transient photocurrent (TPC) decay of the perovskite solar cells without (black) and with (red) PAGG process. (e) Evolution of the measured power conversion efficiencies (PCEs) of encapsulated perovskite solar cells without (black) and with (red) PAGG process under continuous illumination at open-circuit condition. (f) Evolution of the measured power conversion efficiencies (PCEs) of

unencapsulated perovskite solar cells without (black) and with (red) PAGG process exposed to ambient atmosphere at open-circuit and dark condition.

Figure 5.1. Damage of perovskite solar cells cause by the encapsulation temperature and precursors of atomic layer deposition. (a) Schematic diagram of the atomic layer deposition. (b) Degradation of perovskite solar cells caused by heating at different temperature. (c) XRD patterns of MaPbI_3 after O_2 plasma treatment for different intervals of time. AFM images of spiro-MeOTAD (d) before and (e) after O_2 plasma treatment. SEM images of the MaPbI_3 films (f) before and after the treatment with (g) O_2 plasma, (h) H_2O , and (i) EG.

Figure 5.2. Improved encapsulation strategy and its verification. (a) Schematic diagram of the encapsulation process: (I) molecular layer deposition of alucone on the perovskite solar cell, (II) plasma-assisted atomic layer deposition of Al_2O_3 on the alucone and (III) methyl groups in the alucone consumed the O_2 plasma generated by the PEALD process and protected the perovskite solar cells. (b) Time evolution of the methane by-product during the initial growth of MLD alucone monitored by *in-situ* QMS. (c) *In-situ* QCM and QMS results for the reaction between alucone and O_2 plasma. (d) Fourier-transform infrared spectra of alucone films before and after O_2 plasma treatment.

Figure 5.3. Characterization of the properties of encapsulation films. (a) Structure schematic diagram of the perovskite solar cell and cross-section SEM image of perovskite solar cell with encapsulation layer. (b) TEM image of barrier layer on the perovskite solar cells. (c) Remained efficiencies of perovskite solar cells with different cycles of alucone after O_2 plasma treatment. (d) Schematic diagram of the organic-inorganic nanolaminate structure showing the passivation of the defects and protection against water vapor permeation. (e) Leakage current of barrier layers as a function of voltage. (f) Water vapor transmission rate of different encapsulation structures under the same cycle number.

Figure 5.4. Stability tests of the encapsulated perovskite solar cells. Efficiency of 27 perovskite solar cells (a) before and (b) after encapsulation. Time evolution of normalized PCE for the perovskite solar cells with and without encapsulation (c) in water and (d) under a high-humidity environment.

List of Tables

Table 3.1 | Photoluminescence lifetimes and defect density of the films with 2-aminoethylphosphonic acid (PA), hypotaurine (SA) and β -alanine additives (CA) or without additives. Corresponding photovoltaic parameters of champion perovskite solar cells with or without additives. The PCE values in the parenthesis are the stabilized power out (SPO) of the devices.

Table 4.1 | Detailed photovoltaic parameters of champion perovskite solar cells with and without PAGG

Acknowledgments

I want to express my sincerest gratitude to my mentor and supervisor, Professor Yang Yang, for his support and guidance during these four years in UCLA. I have learnt tremendous knowledge from this brilliant research group, not only on being a proficient researcher, but also on being a better man. My view of the world has changed, and I am clearer about my life. The interactions with Professor Yang truly transformed me into a solid and sharper person than even before. It will be essential for me to face my future and the society.

I also want to express my thank to my committee: Professor Yu Huang, Professor Yunfeng Lu, and Professor Aaswath P. Raman, for their help and mentorship.

I would like to thank Professor Jin-Wook Lee from Sungkyunkwan University for his guidance of my perovskite research and Professor Tae-Hee Han from Hanyang University for his enlightenment at my initial stage of research. I thank Professor Guangwei Xu from University of Science and Technology of China for his help with my thin-film transistor research and Professor Pei Cheng from Sichuan University for his guidance on my organic photovoltaic research. They helped me to open the gate my Ph.D. research fields.

I also want to express my great gratitude to my wonderful friends and research partners, Dr. Pengcheng Zhu from Nanjing University, Dr. Minhuan Wang from Dalian University of Technology, Dr. Dong Meng and Miss Shu Huang from UCLA, for their genuine support and cooperation. We share so many unforgettable days and nights together, which are the golden moments of my life.

Besides, I want to thank Professor Yu Duan from Jilin University, Professor Ilhan Yavuz from University of Marmara, Professor Jia Zhu from Nanjing University, Professor Zipeng Zhao from

Beijing Institute of Technology, Professor Nam-Gyu Park from Sungkyunkwan University, Professor Jiming Bian from Dalian University of Technology, Professor Marc Weber from Washington State University, Professor Sang-Hoon Bae from Washington University in Saint Louis, Professor Jaime Marian, Professor Bruce Dunn and Professor Mark Goorsky from UCLA, for the cooperation and support provided by them. I thank Professor Zhao-Kui Wang from Soochow University, Prof. Zhenxing Li from China University of Petroleum, Professor Rui Wang from Westlake University, Professor Jingjing Xue from Zhejiang University, for the valuable discussion and great help.

I also want to thank Dr. Zhenyu Wang, Dr. Haoran Wang, Dr. Hangbo Yang, Dr. Quantan Wu, Dr. Tianyi Huang, Dr. Haowen Cheng, Miss Yuan Zhu, Mr. Shaun Tan, Mr. Ran Zheng, Dr. Le Cai, Dr. Sheng-Yung Chang, Anni Zhang, Mr. Yijie Huang, Mr. Daqian Bao, Mr. Yifang Zhou, Dr. Hao-Cheng Wang, Dr. Jiahui Zhu, Miss Zhiyu Zhao, Dr. Hao Wu, Dr. Chen Chen, Dr. Yunfei Liu, Mr. Ju-Hong Lee, Mr. Sung-Joon Lee for the help in my research.

This dissertation and the correlated works were supported by many brilliant minds. With all these helps from my mentors, partners, and friends, I improved much from four years ago. And I believe I can advance more in the future.

At the last, I want to thank my family, especially my grandparents, my parents, and my uncles. Their support and encouragement are the anchor of my life.

Chapter One is a version of *Acc. Mater. Res.*, **2021**, 2, 6, 447–457; Chapter Two is a version of *Nat. Mater.*, **2021**, in review; Chapter Three is a version of *J. Am. Chem. Soc.*, **2020**, 142(47), 20071-20079; Chapter Four is a version of *Advanced Materials*, **2020**, 32(17): 1907769; Chapter Five is a version of *Nano Energy*, **2020**, 69: 104375; All the permissions have been granted by the publishers

VITA

2017-2021 Materials Science and Engineering, Graduate Student Researcher, University of California, Los Angeles

2015-2017 Materials Science and Engineering, M.S., Carnegie Mellon University

2011-2015 Materials Physics, B.S., Nanjing University

Selected Publications

1. **Y. Zhao**, I. Yavuz, M. Wang, M. Weber, J.-H. Lee, S. Tan, T. Huang, D. Meng, R. Wang, J. Xue, Sung-Joon Lee, S.-H. Bae, A. Zhang, T.-H. Han, Y. Zhou, J. Bian, N.-G. Park, J.-W. Lee, Y. Yang, Significantly Suppressing Ion Migration in Metal Halide Perovskites via Trace of Multivalent Interstitial Doping, *Nat. Mater.* in review.
2. **Y. Zhao**, P. Cheng, H. Yang, M. Wang, D. Meng, Y. Zhu, R. Zheng, T. Li, A. Zhang, S. Tan, T. Huang, J. Bian, X. Zhan, Y. Yang, Towards High-Performance Semitransparent Organic Photovoltaics: Dual-Functional p-Type Soft Interlayer, *Adv. Mater.* In revision.
3. **Y. Zhao**[†], Q. Wu[†], G. Xu, K. Wang, Y. Wang, Z. Zhao, H. Wu, D. Bao, A. Zhang, R. Wang, Z. Lin, M. E. Liao, Z. Wang, L. Cai, Z. Wang, M. S. Goorsky, Y. Huang, Y. Yang, Solution-processed High-mobility and Stable Metal-oxide Thin-film Transistor with Self-assembled Vertical Electron-transporting Pathways, *ACS Nano*. Submitted.
4. **Y. Zhao**[†], Y. Zhu[†], H.-Wen Cheng, R. Zheng, D. Meng, Y. Yang, Tailored Key Parameters of Perovskite for High-Performance Photovoltaics, *Mater. Today Energy*, In Press.

5. **Y. Zhao**, P. Zhu, S. Huang, S. Tan, M. Wang, R. Wang, J. Xue, T.-H. Han, S.-J. Lee, A. Zhang, T. Huang, P. Cheng, D. Meng, J.-W. Lee, J. Marian, Y. Yang, Molecular Interaction Regulates the Performance and Longevity of Defect Passivation for Metal Halide Perovskite Solar Cells. *J. Am. Chem. Soc.* 142(47), 20071-20079 (2020).
6. **Y. Zhao**, Z. Wang, Dr. G. Xu, L. Cai, T-H Han, A. Zhang, Q. Wu, R. Wang, T. Huang, P. Cheng, S.-Y. Chang, D. Bao, Z. Zhao, M. Wang, Y. Huang, Y. Yang, High Performance Indium-Gallium-Zinc Oxide Thin Film Transistor via Interface Engineering. *Adv. Funct. Mater.* 30(34): 2003285 (2020)
7. **Y. Zhao**, P. Zhu, M. Wang, S. Huang, Z. Zhao, S. Tan, T. Han, J. Lee, T. Huang, R. Wang, J. Xue, D. Meng, Y. Huang, J. Marian, J. Zhu, Y. Yang, A polymerization-assisted grain growth strategy for efficient and stable perovskite solar cells. *Adv. Mater.* 32, 1907769 (2020).
8. **Y. Zhao**, Z. Wang, R. Yuan, Y. Lin, J. Yan, J. Zhang, Z. Lu, D. Luo, J. Pietrasik, M. R. Bockstaller, K. Matyjaszewski, ZnO/carbon hybrids derived from polymer nanocomposite precursor materials for pseudocapacitor electrodes with high cycling stability. *Polymer* 137, 370-377 (2018).
9. **Y. Zhao**, M. P. Li, S. Liu, M. F. Islam, Superelastic pseudocapacitors from freestanding graphene-coated carbon nanotube aerogels. *ACS Appl. Mater. Interfaces* 9, 23810-23819 (2017).

([†]Equal contributions)

Chapter 1 Introduction to the stability issues of perovskite solar cells

1.1 Current status of perovskite solar cells

Energy crisis has continuously become the main issue of the entire human society for decades. It is urgent to figure out feasible substitutes of the conventional energy resources. Solar cell or photovoltaic (PV), a technology that can directly convert sunlight to electricity, has been considered as one of the most promising and cost-effective clean energy techniques that benefit the environment. So far, silicon-based PVs are dominated the market due to the mature fabrication techniques and their relatively high-power conversion efficiency (PCE) and excellent stability.

Metal halide perovskite solar cells have proven themselves as one of the most promising candidates to replace the currently well-commercialized silicon based solar cells. Because of its unique energy band structure, the metal-halide perovskite material has merits such as high defect-tolerance, favorable charge carrier mobility, and high absorption coefficient. Metal-halide perovskite solar cells have prevailed in the landscape of the third-generation photovoltaic technologies due to their ease-of-processing and superior optoelectronic properties. This unique chemical structure leads to desirable optical and electronic properties for photovoltaic applications, such as large absorption coefficient, tunable band gap, and long carrier lifetime due to its defect tolerance. The typical structure of a photovoltaic perovskite is ABX_3 , where A refers to a monovalent cation such as methylammonium (MA^+), cesium (Cs^+), or formamidinium (FA^+); B refers to a divalent cation such as Pb^{2+} or Sn^{2+} ; and X refers to a halide anion. In general, a perovskite PV device consists of an active layer of perovskite absorber, which is sandwiched between a hole transporting layer (HTL) an electron transporting layer (ETL). In the past few years, metal halide perovskite PV cells have been a major focus of current PV research owing to

their intriguing optoelectronic performances. The record PCE of perovskite PV cells has unprecedentedly increased from an initial 3.8% to 25.5% (**Figure 1.1**).¹⁻⁵ In the beginning, the strategies to improve the PCEs mainly focused on developing an effective method to grow a smooth and continuous polycrystalline film.⁶⁻¹⁰ After the improvement of baseline PCE of the perovskite PVs, various techniques were employed to reduce the defects of perovskite formed at grain boundaries and surfaces, further pushing the PCEs of perovskite PV devices to over 20%.¹¹⁻¹⁸ In the meantime, the discovery of suitable and low-cost interfacial materials such as electron-transporting materials and hole-transporting materials has also appealed to the attention of the perovskite research community to accelerate the commercialization of the perovskite PVs.¹⁹⁻²¹

1.2 Challenges of the perovskite solar cells

However, when we determine the general performances of a solar cell device, there are three major elements we need to consider: the cost, the efficiency, and the lifetime (**Figure 1.2**).²² As shown in **Figure 1.3**, the levelized cost of electricity of the silicon-based solar cell is 5.50 cents per watt, while the one of the perovskite solar cell is 4.34 cents per watt.²³ It indicates that the cost of the perovskite solar cells is comparable or even lower than the silicon ones. As for the efficiency, the certified PCE of the single-junction silicon-based solar cell is 26.1% while the certified PCE of the single-junction perovskite solar cell is 25.5%.¹ As describe before, the efficiency of the perovskite solar cells is also close to the silicon ones now. However, if we compare the lifetime of the silicon-based solar cell and the perovskite solar cell, there is a huge difference that the lifetime of the perovskite devices is typically shorter than one year, while the silicon-based ones can survive over decades. We can clearly see that the major issue that hinders the successful real-life application of the metal halide perovskite solar cell is its unsatisfactory stability.

1.3 The four elements of perovskite solar cell instability

There are the four basic elements that causing the instability of perovskite solar cells: light, heat, bias, and moisture. Here, we detailly illustrate the perovskite material degradation mechanism behind each environment. As shown in **Figure 1.4A**, in the halide lattice within the perovskite with ionic vacancies, at the beginning, there is a stoichiometric amount of anion and cation vacancies, which are randomly distributed in the perovskite lattice. After the device was exposed to light, halide vacancies migrate to the interface with hole selective contact, leaving the relatively immobile cation vacancies behind. Also, cation vacancies form an additional Debye layer at the interface with the electron selective contact.²⁴ As shown in **Figure 1.4B**, when the ions concentrate at the interface of the device, iodide ions will become iodide vapor and the MA^+ cations will be become methyl amine.^{25,26} This mechanism of ion migration will accelerate the decomposition of the perovskite materials.

As for the heat influences on the perovskite materials, as shown in **Figure 1.5A**, the mechanism is similar as the light influences.²⁷ Basically, the elevated heat provides extra energy of the ion migration, which in other words, facilitate the ion migration inside of the perovskite film. As shown in **Figure 1.5B**, researchers can observe MABr vacancy-assisted ion transport along the surface. These consecutive STM images showed the mobility of the vacancies along the perovskite surface.²⁸ Other researchers also investigated the stability of devices by heating the perovskite films for 70 min at 25 °C, 85 °C, 100 °C, 150 °C, and 15 min at 200 °C and 3 min at 250 °C (**Figure 1.5C**).²⁹ With the increase of heat treatment temperature, the color of perovskite films changed gradually from black to yellow. Similarly, the color has the same trend with the increased heat treatment time at high temperature of 250 °C. Also, they found the PCE of the fabricated perovskite solar cells exhibited a nearly linear reduction, which implied that temperature

greatly influenced the stability of the perovskite devices. Besides, researchers also took Z-contrast images, where the brightness of a given pixel is proportional to the average atomic number and thickness.³⁰ We can observe from the images that as we heat the perovskite samples at higher temperature, the degradation of the perovskite materials become more obvious and severe. All these experiments confirmed the heat as one of the major elements that causes the instability of the perovskite solar cells.

The influences of the bias on the perovskite materials are also similar as the ones of light and heat. It is still originated from the ion migration. The directional potential inside of the perovskite grains accelerate the migration of the ions. As shown in **Figure 1.6A**, a typical device was switched more than 750 times with the V_{OC} in the first ten and last ten poling cycles.³¹ After positive poling, V_{OC} showed switching fatigue from 0.73 V to 0.21 V. Besides, as transparency of the perovskite film was monitored in situ under an optical microscope (**Figure 1.6B**). The perovskite stripe area close to the anode became increasingly transparent, and the morphology in this area was completely different from other areas, with many pinholes appearing, indicating the drift of ions from the anode side.³¹

As for the moisture influences, the mechanism will be different from the others. As shown in **Figure 1.7A**, when exposed into high humidity environment, a large number of hydrated crystals appear between grains due to the faster diffusion of water molecules along grain boundaries.³² The water molecule will be the catalyst that degrade the perovskite materials (**Figure 1.7B**). The irreversible degradation of the perovskite layer is a problem for the lifetime of photovoltaic cells, and it is compounded by the nature of the by-products.³³ Also, from the atomic force microscope (AFM) measurements of the perovskite films in the high humidity environment, the roughness of film surface increases with exposure time, and the color changes continuously

during the hydration process. A large number of needle-shaped crystallizations appear after 90 minutes, while crack depth on surface increases.³²

1.4 The major mechanism of perovskite photovoltaic instability and solution principles

From the discussion above, we can draw the conclusion that the major causes of the instability of the perovskite solar cells are the ion migration and moisture attack from the outer environment. Hence, effective methods that hinder the intrinsic ion migration and extrinsically encapsulate the devices should be developed. Besides the mechanism mentioned above, the ion migration has some other effects on the perovskite solar cell device. As shown in **Figure 1.8**, the ion migration will create more defects and accelerate the phase separation of the perovskite film. Also, if the ions go into the transport layers or even electrodes, the devices will lose the functionality.³⁴ To mitigate the ion migration of the perovskite materials, we should start from the ion migration pathways of the perovskite film. As shown in **Figure 1.9**, the bulk point defects, the surface and grain boundaries of the crystal grain are the major pathways of the ion migration. In addition, the local lattice distortion caused by mesoporous scaffold confinement, accumulated charges, dissolved clusters due to absorbed molecules, and strains due to piezoelectric effect can also contribute to the ion migration.³⁵

From the understanding of the mechanism of the instability of the perovskite solar cells, we came up with four effective strategies from interior to exterior: 1. Increase the energy barrier of ion migration; 2. Nullify charged defect and lower the defect density; 3. Reduce grain boundary density to minimize ion migration pathways; 4. High-quality encapsulation. In the following chapters, I will introduce these strategies and the resulted improvements of the perovskite solar cell devices.

References

- (1) <https://www.nrel.gov/pv/assets/pdfs/best-research-cell-efficiencies.20200104.pdf>. Best Research-Cell Efficiency Chart.
- (2) Cai, M.; Wu, Y.; Chen, H.; Yang, X.; Qiang, Y.; Han, L. Cost-Performance Analysis of Perovskite Solar Modules. *Adv. Sci.* **2017**, *4* (1).
- (3) Yoshikawa, K.; Kawasaki, H.; Yoshida, W.; Irie, T.; Konishi, K.; Nakano, K.; Uto, T.; Adachi, D.; Kanematsu, M.; Uzu, H.; Yamamoto, K. Silicon Heterojunction Solar Cell with Interdigitated Back Contacts for a Photoconversion Efficiency over 26%. *Nat. Energy* **2017**, *2* (5).
- (4) Li, Z.; Zhao, Y.; Wang, X.; Sun, Y.; Zhao, Z.; Li, Y.; Zhou, H.; Chen, Q. Cost Analysis of Perovskite Tandem Photovoltaics. *Joule* **2018**, *2* (8), 1559–1572.
- (5) Kojima, A.; Teshima, K.; Shirai, Y.; Miyasaka, T. Organometal Halide Perovskites as Visible-Light Sensitizers for Photovoltaic Cells. *J. Am. Chem. Soc.* **2009**.
- (6) Kim, H. S.; Lee, C. R.; Im, J. H.; Lee, K. B.; Moehl, T.; Marchioro, A.; Moon, S. J.; Humphry-Baker, R.; Yum, J. H.; Moser, J. E.; Grätzel, M.; Park, N. G. Lead Iodide Perovskite Sensitized All-Solid-State Submicron Thin Film Mesoscopic Solar Cell with Efficiency Exceeding 9%. *Sci. Rep.* **2012**, *2* (1), 591.
- (7) Green, M. A.; Ho-Baillie, A.; Snaith, H. J. The Emergence of Perovskite Solar Cells. *Nature Photonics*. Nature Publishing Group July 27, 2014, pp 506–514.
- (8) Xiao, M.; Huang, F.; Huang, W.; Dkhissi, Y.; Zhu, Y.; Etheridge, J.; Gray-Weale, A.; Bach, U.; Cheng, Y. B.; Spiccia, L. A Fast Deposition-Crystallization Procedure for

- Highly Efficient Lead Iodide Perovskite Thin-Film Solar Cells. *Angew. Chemie - Int. Ed.* **2014**, *53* (37), 9898–9903.
- (9) Stranks, S. D.; Snaith, H. J. Metal-Halide Perovskites for Photovoltaic and Light-Emitting Devices. *Nature Nanotechnology*. May 7, **2015**, pp 391–402.
- (10) Nie, W.; Tsai, H.; Asadpour, R.; Blancon, J. C.; Neukirch, A. J.; Gupta, G.; Crochet, J. J.; Chhowalla, M.; Tretiak, S.; Alam, M. A.; Wang, H. L.; Mohite, A. D. High-Efficiency Solution-Processed Perovskite Solar Cells with Millimeter-Scale Grains. *Science* (80-.). **2015**, *347* (6221), 522–525.
- (11) Jeon, N. J.; Noh, J. H.; Yang, W. S.; Kim, Y. C.; Ryu, S.; Seo, J.; Seok, S. Il. Compositional Engineering of Perovskite Materials for High-Performance Solar Cells. *Nature* **2015**, *517* (7535), 476–480.
- (12) Bi, D.; Yi, C.; Luo, J.; Décoppet, J. D.; Zhang, F.; Zakeeruddin, S. M.; Li, X.; Hagfeldt, A.; Grätzel, M. Polymer-Templated Nucleation and Crystal Growth of Perovskite Films for Solar Cells with Efficiency Greater than 21%. *Nat. Energy* **2016**, *1* (10), 16142.
- (13) Zheng, X.; Chen, B.; Dai, J.; Fang, Y.; Bai, Y.; Lin, Y.; Wei, H.; Zeng, X. C.; Huang, J. Defect Passivation in Hybrid Perovskite Solar Cells Using Quaternary Ammonium Halide Anions and Cations. *Nat. Energy* **2017**, *2* (7), 17102.
- (14) Zong, Y.; Zhou, Y.; Zhang, Y.; Li, Z.; Zhang, L.; Ju, M. G.; Chen, M.; Pang, S.; Zeng, X. C.; Padture, N. P. Continuous Grain-Boundary Functionalization for High-Efficiency Perovskite Solar Cells with Exceptional Stability. *Chem* **2018**, *4* (6), 1404–1415.
- (15) Ran, C.; Xu, J.; Gao, W.; Huang, C.; Dou, S. Defects in Metal Triiodide Perovskite

- Materials towards High-Performance Solar Cells: Origin, Impact, Characterization, and Engineering. *Chemical Society Reviews*. The Royal Society of Chemistry June 18, 2018, pp 4581–4610. <https://doi.org/10.1039/c7cs00868f>.
- (16) Tong, J.; Song, Z.; Kim, D. H.; Chen, X.; Chen, C.; Palmstrom, A. F.; Ndione, P. F.; Reese, M. O.; Dunfield, S. P.; Reid, O. G.; Liu, J.; Zhang, F.; Harvey, S. P.; Li, Z.; Christensen, S. T.; Teeter, G.; Zhao, D.; Al-Jassim, M. M.; Van Hest, M. F. A. M.; Beard, M. C.; Shaheen, S. E.; Berry, J. J.; Yan, Y.; Zhu, K. Carrier Lifetimes of >1 Us in Sn-Pb Perovskites Enable Efficient All-Perovskite Tandem Solar Cells. *Science (80-.)*. **2019**, *364* (6439), 475–479. <https://doi.org/10.1126/science.aav7911>.
- (17) Wang, R.; Mujahid, M.; Duan, Y.; Wang, Z. K.; Xue, J.; Yang, Y. A Review of Perovskites Solar Cell Stability. *Advanced Functional Materials*. John Wiley & Sons, Ltd February 12, 2019, p 1808843.
- (18) Jiang, Q.; Zhao, Y.; Zhang, X.; Yang, X.; Chen, Y.; Chu, Z.; Ye, Q.; Li, X.; Yin, Z.; You, J. Surface Passivation of Perovskite Film for Efficient Solar Cells. *Nat. Photonics* **2019**, *13* (7), 460–466.
- (19) Jung, E. H.; Jeon, N. J.; Park, E. Y.; Moon, C. S.; Shin, T. J.; Yang, T. Y.; Noh, J. H.; Seo, J. Efficient, Stable and Scalable Perovskite Solar Cells Using Poly(3-Hexylthiophene). *Nature*. Nature Publishing Group March 27, 2019, pp 511–515.
- (20) Christians, J. A.; Schulz, P.; Tinkham, J. S.; Schloemer, T. H.; Harvey, S. P.; Tremolet De Villers, B. J.; Sellinger, A.; Berry, J. J.; Luther, J. M. Tailored Interfaces of Unencapsulated Perovskite Solar Cells for >1,000 Hour Operational Stability. *Nat. Energy* **2018**, *3* (1), 68–74.

- (21) Jeon, N. J.; Na, H.; Jung, E. H.; Yang, T. Y.; Lee, Y. G.; Kim, G.; Shin, H. W.; Il Seok, S.; Lee, J.; Seo, J. A Fluorene-Terminated Hole-Transporting Material for Highly Efficient and Stable Perovskite Solar Cells. *Nat. Energy* **2018**, *3* (8), 682–689.
- (22) Meng, L.; You, J.; Yang, Y. Addressing the Stability Issue of Perovskite Solar Cells for Commercial Applications. *Nature communications* **2018**, *9*, 1-4.
- (23) Li, Z.; Zhao, Y.; Wang, X.; Sun, Y.; Zhao, Z.; Li, Y.; Zhou, H.; Chen, Q. Cost Analysis of Perovskite Tandem Photovoltaics. *Joule* **2018**, *2*, 1559-1572.
- (24) Domanski, K.; Roose, B.; Matsui, T.; Saliba, M.; Turren-Cruz, S.-H.; Correa-Baena, J.-P.; Carmona, C. R.; Richardson, G.; Foster, J. M.; De Angelis, F. Migration of Cations Induces Reversible Performance Losses over Day/Night Cycling in Perovskite Solar Cells. *Energy & Environmental Science* **2017**, *10*, 604-613.
- (25) Ito, S.; Tanaka, S.; Manabe, K.; Nishino, H. Effects of Surface Blocking Layer of Sb₂S₃ on Nanocrystalline TiO₂ for CH₃NH₃PbI₃ Perovskite Solar Cells. *The Journal of Physical Chemistry C* **2014**, *118*, 16995-17000.
- (26) Chen, Q.; De Marco, N.; Yang, Y. M.; Song, T.-B.; Chen, C.-C.; Zhao, H.; Hong, Z.; Zhou, H.; Yang, Y. Under the Spotlight: The Organic–Inorganic Hybrid Halide Perovskite for Optoelectronic Applications. *Nano Today* **2015**, *10*, 355-396.
- (27) Walsh, A.; Stranks, S. D. Taking Control of Ion Transport in Halide Perovskite Solar Cells. *ACS Energy Letters* **2018**, *3*, 1983-1990.
- (28) Stecker, C.; Liu, K.; Hieulle, J.; Ohmann, R.; Liu, Z.; Ono, L. K.; Wang, G.; Qi, Y. Surface Defect Dynamics in Organic–Inorganic Hybrid Perovskites: From Mechanism to Interfacial Properties. *ACS nano* **2019**, *13*, 12127-12136.

- (29) Meng, Q.; Chen, Y.; Xiao, Y. Y.; Sun, J.; Zhang, X.; Han, C. B.; Gao, H.; Zhang, Y.; Yan, H. Effect of Temperature on the Performance of Perovskite Solar Cells. *Journal of Materials Science: Materials in Electronics* **2021**, *32*.
- (30) Divitini, G.; Cacovich, S.; Matteocci, F.; Cinà, L.; Di Carlo, A.; Ducati, C. In Situ Observation of Heat-Induced Degradation of Perovskite Solar Cells. *Nature Energy* **2016**, *1*, 1-6.
- (31) Xiao, Z.; Yuan, Y.; Shao, Y.; Wang, Q.; Dong, Q.; Bi, C.; Sharma, P.; Gruverman, A.; Huang, J. Giant Switchable Photovoltaic Effect in Organometal Trihalide Perovskite Devices. *Nature materials* **2015**, *14*, 193-198.
- (32) Zhang, C. X.; Shen, T.; Guo, D.; Tang, L. M.; Yang, K.; Deng, H. X. Reviewing and Understanding the Stability Mechanism of Halide Perovskite Solar Cells. *InfoMat* **2020**, *2*, 1034-1056.
- (33) Wang, D.; Wright, M.; Elumalai, N. K.; Uddin, A. Stability of Perovskite Solar Cells. *Solar Energy Materials and Solar Cells* **2016**, *147*, 255-275.
- (34) Bi, E.; Song, Z.; Li, C.; Wu, Z.; Yan, Y. Mitigating Ion Migration in Perovskite Solar Cells. *Trends in Chemistry* **2021**.
- (35) Yuan, Y.; Huang, J. Ion Migration in Organometal Trihalide Perovskite and Its Impact on Photovoltaic Efficiency and Stability. *Accounts of chemical research* **2016**, *49*, 286-293.

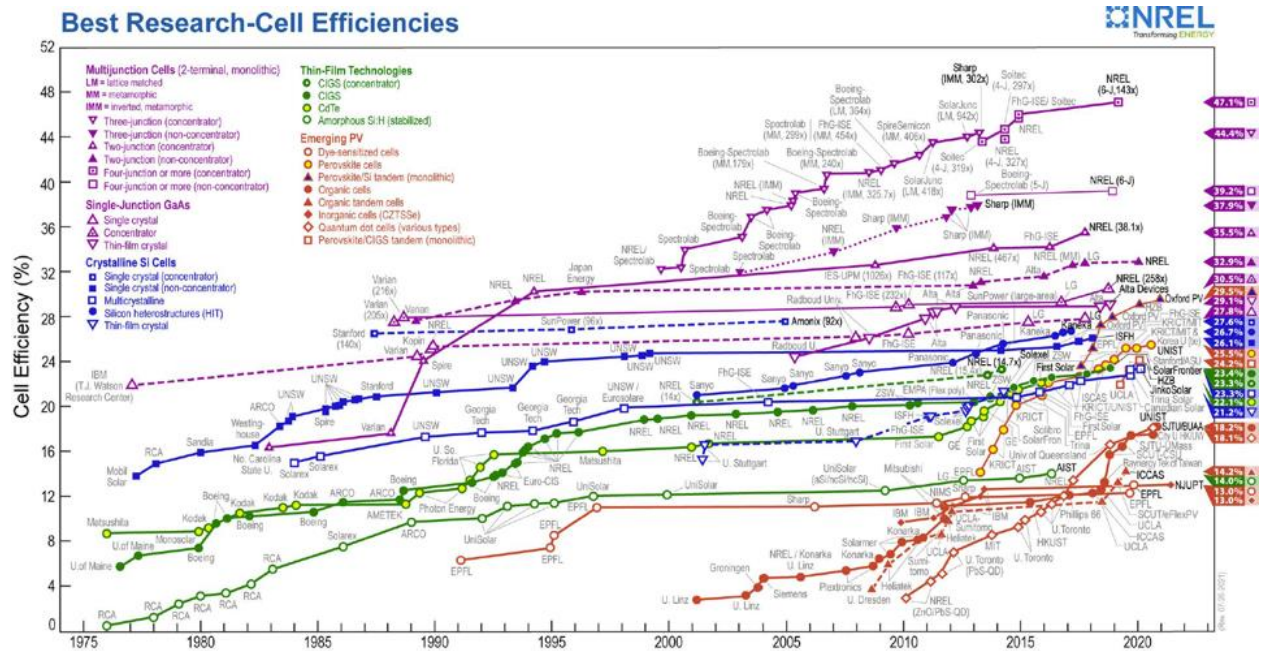


Figure 1.1 | NREL Best research cell efficiency chart.¹

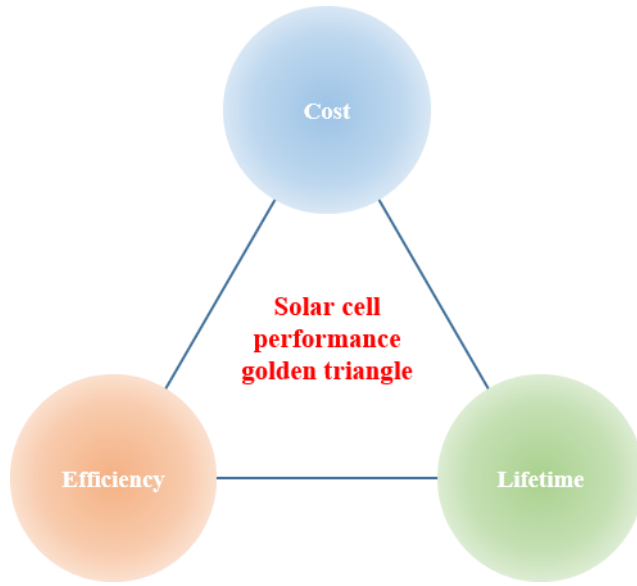


Figure 1.2 | The golden triangle of the solar cell performance.²²

Comparison between single-junction devices

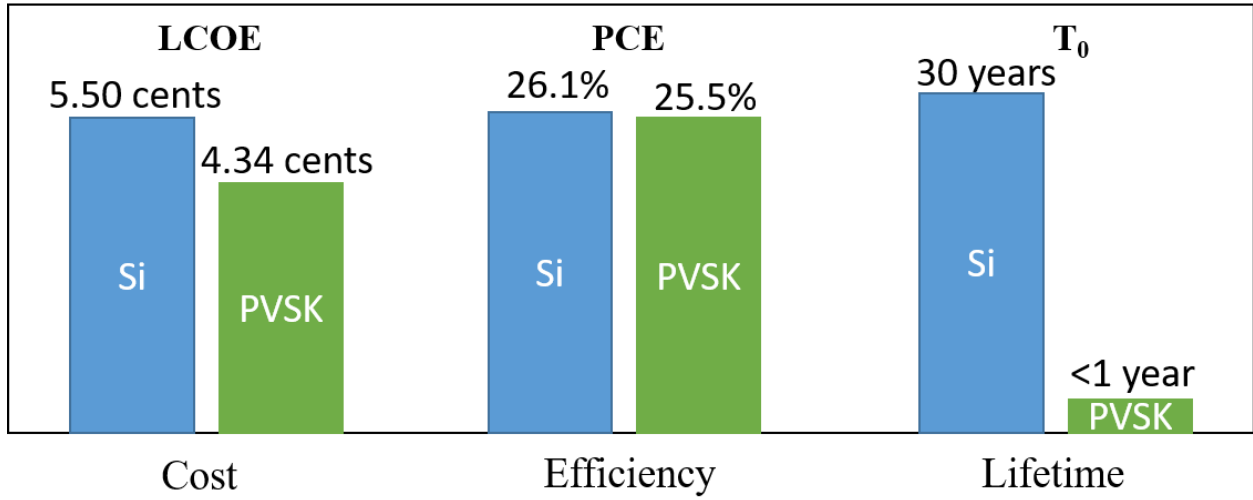


Figure 1.3 | Comparison between single-junction silicon-based solar cell and single-junction perovskite solar cell.^{1,23}

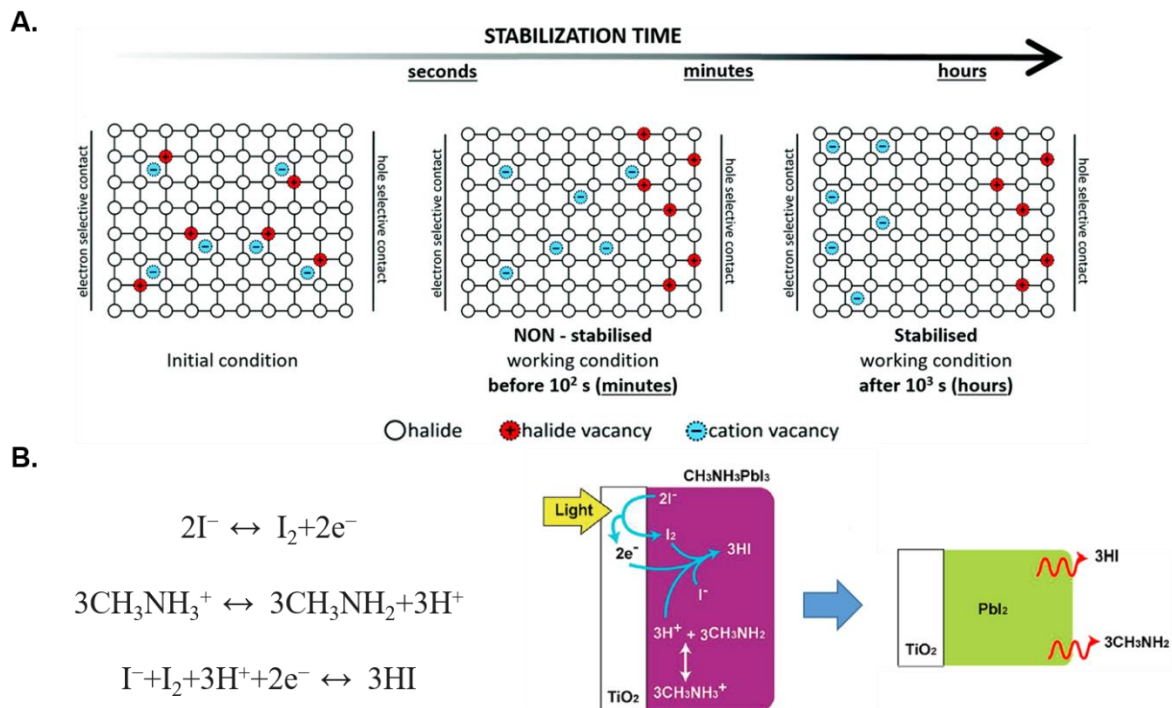


Figure 1.4 | (A) Schematics of the evolution of the ion distribution within the perovskite layer sandwiched between the electron and hole selective contacts under solar cell working conditions: initial conditions, non-stabilized conditions on the timescale of minutes and the stabilized condition on the timescale of hours. (B) The evaporation mechanism of the ions in metal-halide perovskite material and the scheme of the degradation of perovskite materials under the sunlight.^{24,25,26}

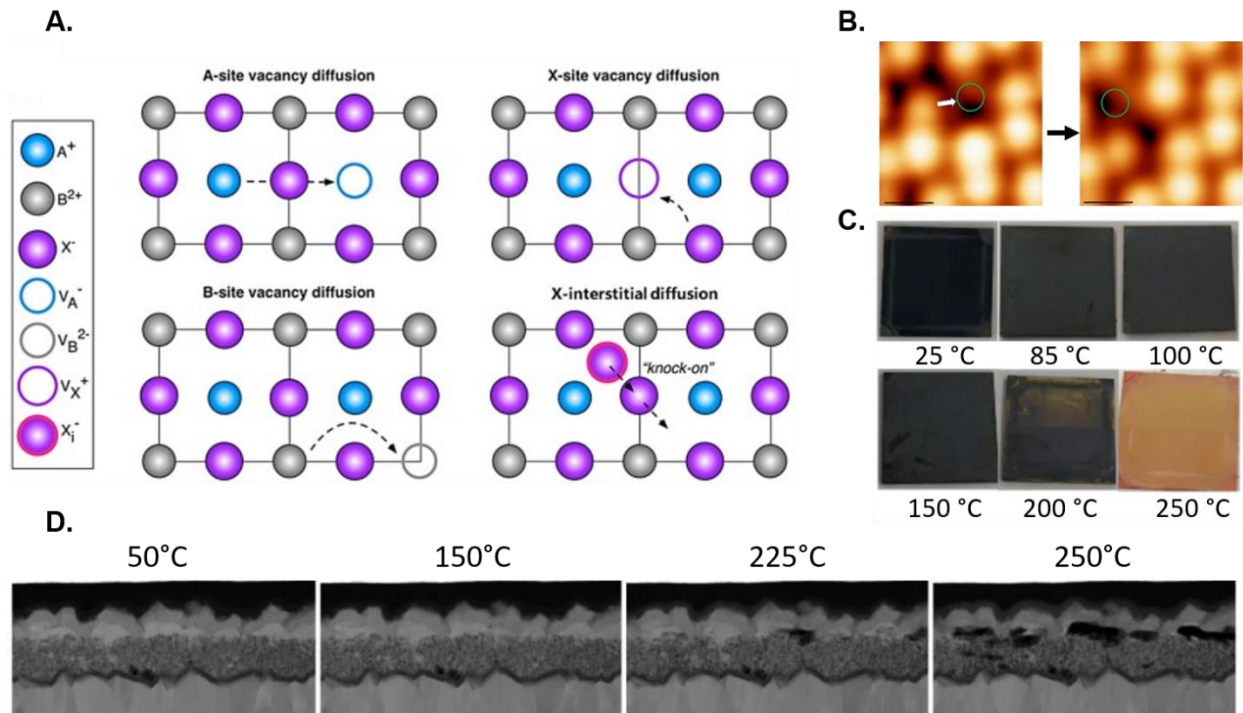


Figure 1.5 | (A) Illustration of possible elementary microscopic mechanisms for ion transport mediated by the activated diffusion of charged point defects in perovskites. (B) Vacancy-assisted ion transport along the surface of perovskite. (C) Images of perovskite films heated at different temperatures for 70 min, respectively. (D) STEM-HAADF images of perovskite samples at different stages of heating.^{27,28,29,30}

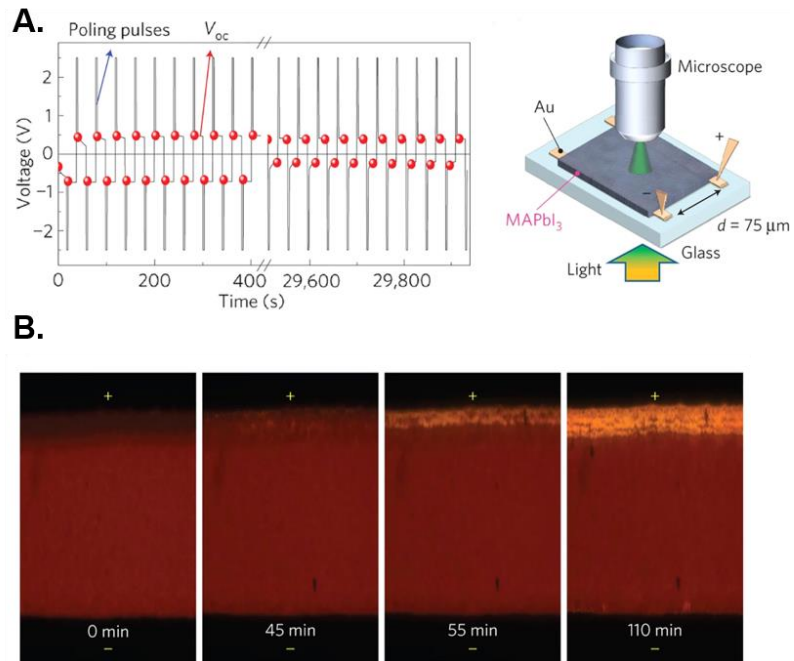


Figure 1.6 | (A) Open circuit voltage of the device recorded after repeated poling by ± 2.5 V bias for more than 750 cycles. (B) In situ monitoring of the material change during the poling process.³¹

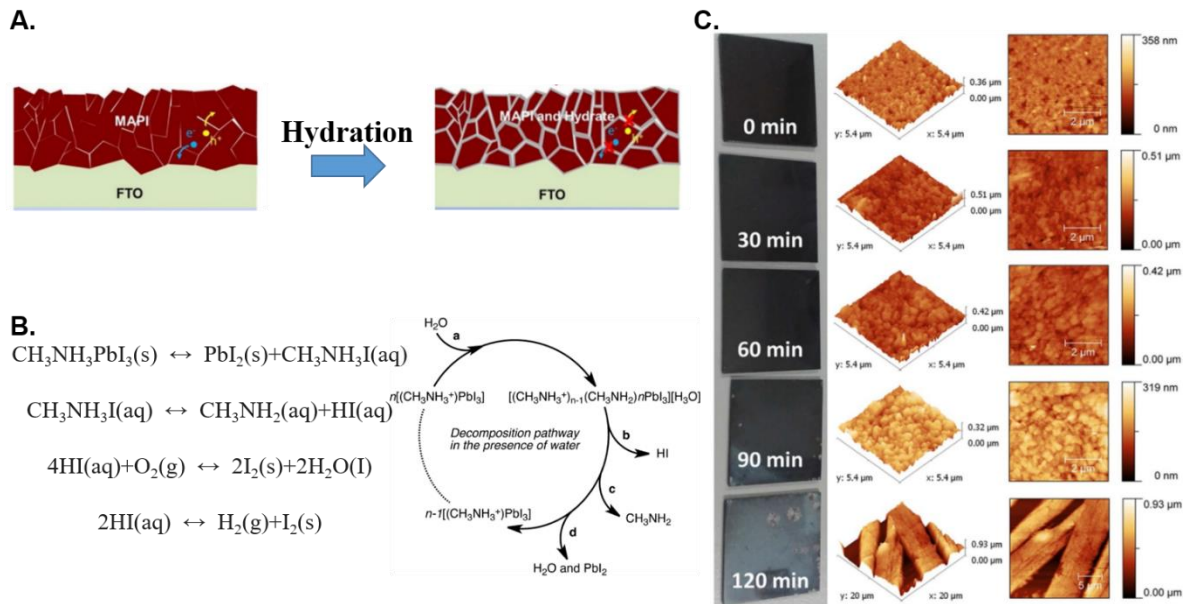


Figure 1.7 | (A) Degradation model of perovskite films under partial hydration. (B) Proposed decomposition pathway of perovskite in the presence of a water molecule. (C) Photographs of MAPbI₃ films deposited on glass at different hydration time showing discoloration and AFM measurements.^{32,33}

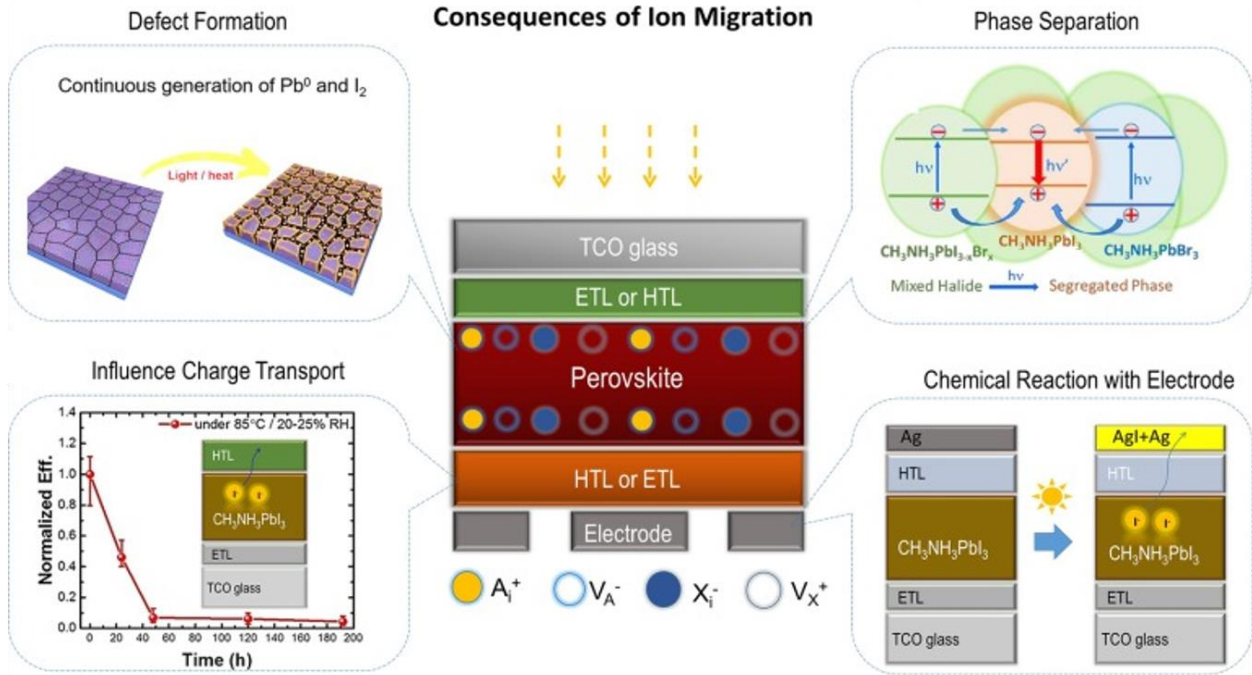


Figure 1.8 | The consequences of intrinsic ion migration for each component layer in perovskite solar cells.³⁴

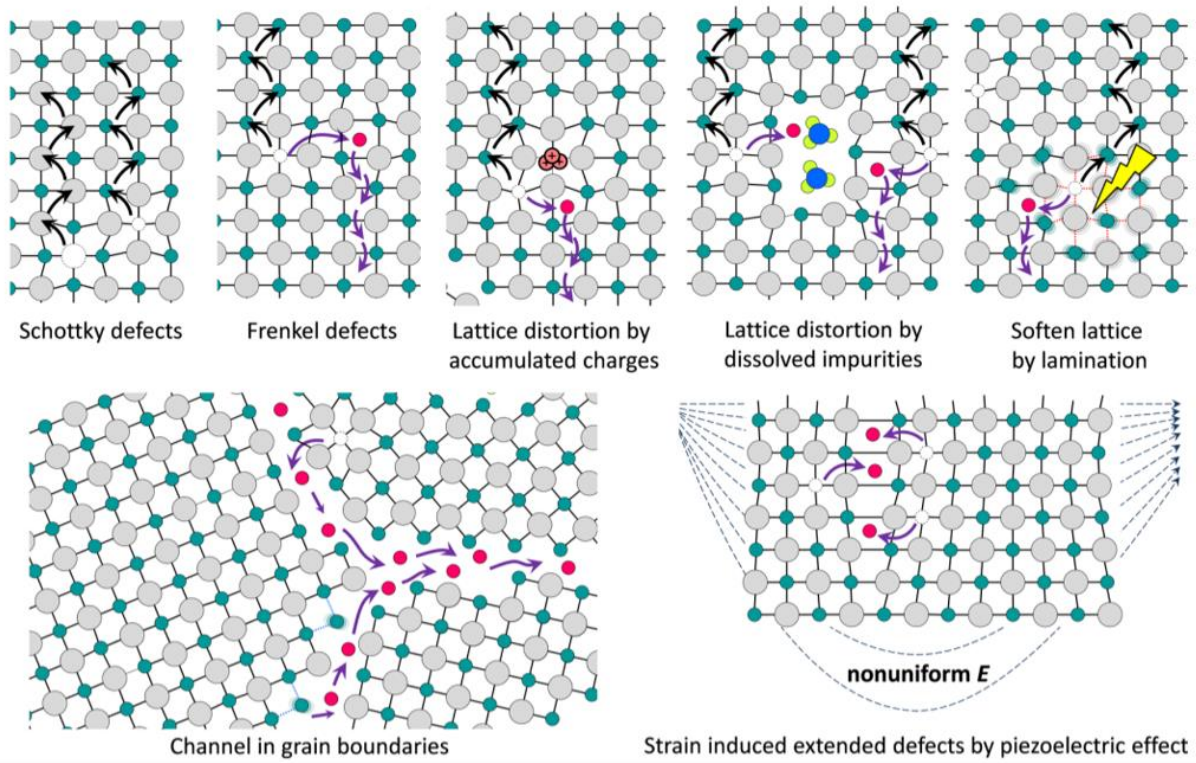


Figure 1.9 | Illustration of the ion migration pathways.³⁵

Chapter 2 Interior multivalent interstitial doping

2.1 Introduction of the interior interstitial doping

Organometal halide perovskite solar cells have experienced eye-catching improvements in its power conversion efficiency (PCE) ¹⁻³. To implement its final step to the commercialization, functional longevity becomes the dernier continent to conquer ⁴⁻⁸. The displacement of the ions and/or charged defects in the perovskite layer has been recognized as the major origin of device performance degradation under its working environment with electric field, heat, and excess charge carriers ⁹⁻¹⁴. Therefore, the suppression of the ion migration should be the key to promote the operational stability of the perovskite solar cells.

Interstitial doping of Alkali metal cations such as lithium (Li^+), sodium (Na^+), potassium (K^+) or rubidium (Rb^+) have been widely used to inhibit the migration of halide ions to relieve current-voltage hysteresis and improve operational stability¹⁵⁻¹⁷. However, the interstitial doping possibly distorts perovskite lattice and induces strain that undermines long-range ordering and stability of the desired phase ^{1, 18-19}. Perhaps for this reason, state-of-the-art record efficiency devices did not incorporate this approach. Hence, there has been a strong need to develop a new approach for preventing these side effects while maximizing the benign ion migration inhibition effect to promote both performance and the operational stability of the perovskite solar cells. Here, we demonstrate an efficient interstitial doping strategy based on trivalent neodymium cation (Nd^{3+}) to prominently prevent the halide migration in the perovskite lattice with a minimal dose addition. Compared with cations with similar ionic radii but the lower valences, i.e. calcium (Ca^{2+}) and sodium cations (Na^+), the higher valence state of Nd^{3+} provides better capability to obstruct the

halide migration and is proven to superiorly passivate the negatively charged defects in the perovskite lattice with substantially less dopant concentration.

2.2 The multivalent interstitial doping strategy

Effective ionic radii of Na^+ , Ca^{2+} and Nd^{3+} are 102, 100 and 98.3 pm, respectively. Compared to iodide anion (I^-), Nd^{3+} , Ca^{2+} , and Na^+ have cation to anion size ratios of 0.447, 0.455, and 0.464, respectively, and thus octahedral (O_h) geometry with 6 coordination is expected as 'A' site cation in ABX_3 perovskite²⁰. However, their radii are much smaller than those of CH_3NH_3^+ (MA^+ , 217 pm) or $\text{HC}(\text{NH}_2)_2^+$ (FA^+ , 253pm)²¹, and thus expected to occupy O_h interstitial sites rather than substitution of existing MA^+ or FA^+ . We simulated the effect of the different interstitial cations on iodide ion migration energetics to the nearby iodine vacancy (V_I) in perovskite crystal cells (**Figure 2.1A, Supplementary Note 1**). Each migration route was divided into eighteen steps and the relative energy differences compared with the initial stage are recorded in **Figure 2.1B**. Without the interstitial cation, the energy barrier for the V_I migration was only about 0.37 eV. The presence of Nd^{3+} enhances the energy barrier significantly (2.80 eV), and Ca^{2+} (0.81 eV) and Na^+ (0.43 eV) are followed. Considering the similar sizes of the cations, the distinction of the ion migration impedance capability might be majorly related to the valence states of the cations. Nd^{3+} with three positive charges are more likely to restrict the motion of negative iodide ions due to stronger electrostatic attraction force. This impeded halide migration by the cation doping is favorable for the stability enhancement and hysteresis elimination of the perovskite solar cell devices.

Regardless of the beneficial ion migration mitigation effect, the interstitial cation doping can introduce tensile strain to the perovskite lattice that can potentially destabilize the lattice^{1, 18-}

¹⁹. In X-ray diffraction (XRD) measurement in **Figure 2.1C**, the progressive shift of the (100) orientation peak of a-FAPbI₃ to lower two theta angle with increasing cation dopant concentration supports interstitial incorporation of the cation and thus induced lattice volume expansion due to the tensile strain. According to Williamson-Hall analysis (**Figure A2.1-A2.4, Table B2.1-B2.3** and **Supplementary Note 2**), the lattice strain rapidly rises even with relatively low dopant concentration (<1%, by molar ratio), and then decreases with further addition probably due to relaxation by generation of dislocations, grain boundaries or secondary phases. From XRD patterns in **Figure 2.1D**, as dopant concentration reaches 1%, it was noticed that the intensity of (001) a-FAPbI₃ peak is reduced while that of (001) PbI₂ peak intensifies. Further increase in dopant concentration to 5% induces the appearance of (010) non-perovskite δ -FAPbI₃ peak, indicating destabilization of the a-FAPbI₃ perovskite phase as the concentration of the interstitial dopants increases. Scanning electron microscopic (SEM) images in **Figure A2.5** also showed that grain size of the film generally decreases with the addition of higher amount of cation dopant. Such generation of defects or secondary phase can rather degrade the performance and stability of the device. Thus, despite of the beneficial ion migration mitigation effect, minimal dopant concentration will be preferred to minimize the sacrificial trade-off.

In **Figure 2.2A**, we assessed the photovoltaic performances of the devices with the addition of different cations. Noticeably, the optimal doping concentrations for the highest power conversion efficiencies (PCEs) were varied depending on the cations; 0.08%, 0.25%, and 0.45% for Nd³⁺, Ca²⁺ and Na⁺, respectively. With 0.08% Nd³⁺ doping, a distinct enhancement in the average PCE was achieved from 20.56±0.49 to 23.31±0.29% while 0.25% Ca²⁺ and 0.45% Na⁺ doping result in average PCEs of 22.07±0.35 and 22.05±0.19%, respectively. The open-circuit voltages (V_{OCs}), short-circuit current densities (J_{SCs}) and fill factors (FFs) were largely improved

by the cation addition (**Figure A2.6-A2.8** and **Table B2.4-B2.6**). Negligible current-voltage hysteresis was observed for the device with the Nd^{3+} dopants whereas the Ca^{2+} and Na^+ dopants can only partially reduce the hysteresis observed from the reference device (**Figure 2.2B**). The device with 0.08% Nd^{3+} dopant showed the best PCE of 23.68% with V_{OC} of 1.173 V, J_{SC} of 25.38 mA/cm^2 , and FF of 79.55%. The stabilized PCE is also improved from 19.56 (reference) to 23.10, 22.23 and 21.81% with Nd^{3+} , Ca^{2+} and Na^+ doping, respectively (**Figure 2.2C** and **Table B2.7**). External quantum efficiency (EQE) spectra of the devices were compared in **Figure 2.2D**. An integrated J_{SC} of 25.12 mAcm^{-2} from the Nd^{3+} doped device matched well with the value measured from the J - V scan (<5% discrepancy), whereas that of the control device (24.06 mA cm^{-2}) showed relatively large discrepancy of 6.7%, probably due to pronounced J - V hysteresis. **Figure 1.2E** compares the surface morphology of the perovskite films incorporated with different cation dopants. While overall grain sizes of the films are comparable, closer inspection of the images revealed that small particulates are segregated on the surface of the films with 0.25% Ca^{2+} and 0.45% Na^+ . We speculate relatively higher strain (>0.19%, **Table B2.2** and **B2.3**) induced by 0.25% Ca^{2+} and 0.45% Na^+ might cause clustering and segregation of the dopant on the crystal surface and/or grain boundary, which might limit performance enhancement by sacrificial trade-off²². On the other hand, the film with 0.08% Nd^{3+} showed neat surface comparable to the reference film, and thus the side effects are probably minimized.

2.3 Strong interaction between the defects and the multivalent interstitial dopants

The interstitial cations are likely to interact with negatively charged defects. We investigate the interaction energies of the different cations with the defects including iodine-formamidinium antisites (I_{FA}), lead vacancies (V_{Pb}), formamidinium vacancies (V_{FA}) and iodine-lead antisites (I_{Pb})

based on the density functional theory (DFT) calculations (models are shown in **Figure A2.9**). As summarized in **Figure 2.3A**, the interaction energies between the defects and Nd^{3+} was the highest and those for Ca^{2+} and Na^+ are followed. Considering the similar cation radii, the higher valence charge probably contributes to relatively stronger interaction energies of the Nd^{3+} with the negatively charged intrinsic defects. The stronger interaction energy of the Nd^{3+} might enable more effective defect mitigation with the minimal dosage for the less side effects (e.g. strain, defects, dopant segregation) and thus higher PCE of the device. The time-resolved photoluminescence (TRPL) decay curves of the films with the optimized dopant concentration are compared with that of the reference film in **Figure 2.3B**. The curves were fitted to a single exponential decay model to quantify the PL lifetime (**Table B2.7**). Overall, we observed an elongation of the PL lifetime for the films with the three cations compared with the reference perovskite film; the PL lifetimes of the Nd^{3+} (7.75 μs), Ca^{2+} (5.47 μs), and Na^+ (4.78 μs) films were significantly longer than that of the reference sample (1.68 μs). Regardless of the least addition amount, the most largely elongated PL lifetime for the film with Nd^{3+} supports the effectiveness of the Nd^{3+} dopant for mitigation of the defects. The trend in PL lifetimes correlated with the enhanced steady-state PL intensity (inset of **Figure 2.3B**). On the other hand, the cation-containing films showed no noticeable difference in their PL peak positions and absorption spectra (**Figure A2.10**). We further investigate charge recombination kinetics in the corresponding devices by the transient photovoltage (TPV) decay measurement shown in **Figure 2.3C**. The fitted time constants for reference, Nd^{3+} -, Ca^{2+} - and Na^+ -incorporated devices were 0.50, 0.86, 0.79, and 0.65 ms, respectively, which in line with the trend observed from the measured PL lifetimes.

Positron annihilation spectroscopy (PAS) was employed to compare the density of negatively or neutral charged defects in the films. The positively charged positrons are implanted

from the perovskite surface, which is annihilated upon interaction with electrons from a free lattice site or after trapping at negatively charged or neutral (but not positive) vacancies and/or interstitial defects to emit two gamma photons²³. The shape parameter is extracted from the doppler broadening of the gamma-ray spectrum, and it increases with the increasing density of negatively charged or neutral defects. By changing the kinetic energy of the incident positron, we were able to investigate the depth-dependent defect density of the films incorporated with different cations (**Figure 2.3D**). The results show that the shape parameters of the films with the cations doping in the bulk (mean depth between 10 nm and 500 nm, shaded region in **Figure 2.3D**) is lower than that of the reference film, indicating a decreased density of negatively charged or neutral defects in the bulk region by the cation doping. The average shape parameters of different films in the bulk region are compared in **Figure 2.3E**. The lowest shape parameter of the perovskite film with Nd³⁺ closely correlates with the TRPL and TPV measurements. We further cross-checked the trap density by measuring the total density of states (tDOS) for the as-fabricated devices incorporated with different cations using angular frequency-dependent capacitance measurement. As shown in **Figure 2.3F**, the density of in-gap states for the devices with Nd³⁺, Ca²⁺ and Na⁺ dopants are decreases compared with the reference device where the tendency in the measured trap density coincides with the PL and PAS measurements.

2.4 Impeded ion migration by multivalent interstitial doping

To experimentally verify the effect of the different cation dopants on the ion migration energetics, we performed a temperature-dependent conductivity measurement on lateral perovskite devices with structure of Au/perovskite (100 μm)/Au. The activation energy (E_a) for ion migration can be extracted by linear fitting of the data based on the Nernst–Einstein equation given by

$\sigma(T) = \frac{\sigma_0}{T} \exp\left(\frac{-E_a}{k_b T}\right)$, where $\sigma(T)$ is the conductivity as a function of temperature T , σ_0 is a constant, k_b is Boltzmann constant¹². The E_a was extracted from the slope of the fitted lines at relatively higher temperature (**Figure 2.4A**). The calculated E_a for the film incorporated with Nd^{3+} , Ca^{2+} , and Na^+ were 0.812 eV, 0.703 eV, and 0.626 eV, respectively, which are substantially higher than that of the reference film (0.425 eV). The trend of the measured E_a s also agrees well with the simulation results. The in-situ PL measurement was performed using the lateral device under 440 nm illumination and applied an electric field of 150 mV/ μm to visualize the ion migration (**Figure 2.4B and Figure 2.4C**). As time passes, an obvious PL quenching from the reference film is observed and worsens rapidly. The PL quenching is attributed to the destroyed stoichiometry and/or structure of the crystals due to pronounced migration of charged defects in the reference film²⁴. By contrast, the bright PL signal of the film incorporated with Nd^{3+} remains unchanged even after applying the bias voltage for the 10 minutes, indicating the migration of the charged defects is significantly suppressed by the addition of 0.08 % Nd^{3+} .

To investigate the operational stability of the solar cell devices, we exposed the encapsulated devices to continuous illumination under ambient atmosphere and open-circuit condition (**Figure 2.4D**). Versus maximum power point tracking, the performance degradation is expected to be more accelerated under the open-circuit condition²⁵. Notably, the encapsulated device incorporated with Nd^{3+} maintained 84.3% of its initial PCE after continuous illumination for 2002 hours while the PCE of the reference device degraded to 0% of the initial PCE. Incorporation of Ca^{2+} and Na^+ also improved the operational stability to retain 68.0% and 48.6% of their initial PCEs, respectively. To further explore the thermal stability of the devices, we kept the unencapsulated devices in a nitrogen-filled glove box at 85 °C. After 2002 hours, the reference device completely degraded while the Nd^{3+} , Ca^{2+} , and Na^+ incorporated devices retained 86.4%,

72.7% and 60.3% of their initial PCEs, respectively. The observed improvement in both photo and thermal stability of the devices indicates that incorporation of an interstitial cation with the stronger interaction with the charged defects is beneficial for the mitigation of defect while minimizing the side effects. Thus, regardless of the defect (impurity) tolerant nature of the perovskite, this study highlights the importance of minimizing the dosage of the interstitial dopant to maximize both photovoltaic performance and operational stability of perovskite optoelectronics.

References

- 1 Kim, G., Min, H., Lee, K. S., Yoon, S. M. & Seok, S. I. Impact of strain relaxation on performance of α -formamidinium lead iodide perovskite solar cells. *Science* **370**, 108-112 (2020).
- 2 Jeong, M. *et al.* Stable perovskite solar cells with efficiency exceeding 24.8% and 0.3-V voltage loss. *Science* **369**, 1615-1620 (2020).
- 3 Zheng, X. *et al.* Managing grains and interfaces via ligand anchoring enables 22.3%-efficiency inverted perovskite solar cells. *Nature Energy* **5**, 131-140 (2020).
- 4 Lin, Y.-H. *et al.* A piperidinium salt stabilizes efficient metal-halide perovskite solar cells. *Science* **369**, 96-102 (2020).
- 5 Liu, Z. *et al.* A holistic approach to interface stabilization for efficient perovskite solar modules with over 2,000-hour operational stability. *Nature Energy* **5**, 596-604 (2020).
- 6 Tan, H. *et al.* Efficient and stable solution-processed planar perovskite solar cells via contact passivation. *Science* **355**, 722-726 (2017).

- 7 Jung, E. H. *et al.* Efficient, stable and scalable perovskite solar cells using poly (3-hexylthiophene). *Nature* **567**, 511-515 (2019).
- 8 Wang, L. *et al.* A Eu³⁺-Eu²⁺ ion redox shuttle imparts operational durability to Pb-I perovskite solar cells. *Science* **363**, 265-270 (2019).
- 9 Yuan, Y. & Huang, J. Ion migration in organometal trihalide perovskite and its impact on photovoltaic efficiency and stability. *Accounts of chemical research* **49**, 286-293 (2016).
- 10 Calado, P. *et al.* Evidence for ion migration in hybrid perovskite solar cells with minimal hysteresis. *Nature communications* **7**, 1-10 (2016).
- 11 Tan, S. *et al.* Steric impediment of ion migration contributes to improved operational stability of perovskite solar cells. *Advanced Materials* **32**, 1906995 (2020).
- 12 Lee, J.-W., Kim, S.-G., Yang, J.-M., Yang, Y. & Park, N.-G. Verification and mitigation of ion migration in perovskite solar cells. *APL materials* **7**, 041111 (2019).
- 13 Zhang, H. *et al.* Phase segregation due to ion migration in all-inorganic mixed-halide perovskite nanocrystals. *Nature communications* **10**, 1-8 (2019).
- 14 Boyd, C. C., Cheacharoen, R., Leijtens, T. & McGehee, M. D. Understanding degradation mechanisms and improving stability of perovskite photovoltaics. *Chemical reviews* **119**, 3418-3451 (2018).
- 15 Abdi-Jalebi, M. *et al.* Maximizing and stabilizing luminescence from halide perovskites with potassium passivation. *Nature* **555**, 497-501 (2018).
- 16 Son, D.-Y. *et al.* Universal approach toward hysteresis-free perovskite solar cell via defect engineering. *Journal of the American Chemical Society* **140**, 1358-1364 (2018).

- 17 Cao, J., Tao, S. X., Bobbert, P. A., Wong, C. P. & Zhao, N. Interstitial occupancy by extrinsic alkali cations in perovskites and its impact on ion migration. *Advanced Materials* **30**, 1707350 (2018).
- 18 Jones, T. W. *et al.* Lattice strain causes non-radiative losses in halide perovskites. *Energy & Environmental Science* **12**, 596-606 (2019).
- 19 Zhao, J. *et al.* Strained hybrid perovskite thin films and their impact on the intrinsic stability of perovskite solar cells. *Science advances* **3**, eaao5616 (2017).
- 20 Callister, W. D. *Fundamentals of materials science and engineering*. Vol. 471660817 (Wiley London, 2000).
- 21 Kim, J. Y., Lee, J.-W., Jung, H. S., Shin, H. & Park, N.-G. High-efficiency perovskite solar cells. *Chemical Reviews* **120**, 7867-7918 (2020).
- 22 Yan, M., Cannon, R. & Bowen, H. Space charge, elastic field, and dipole contributions to equilibrium solute segregation at interfaces. *Journal of Applied Physics* **54**, 764-778 (1983).
- 23 Tan, S. *et al.* Shallow Iodine Defects Accelerate the Degradation of α -Phase Formamidinium Perovskite. *Joule* **4**, 2426-2442 (2020).
- 24 Kim, S.-G. *et al.* Potassium ions as a kinetic controller in ionic double layers for hysteresis-free perovskite solar cells. *Journal of Materials Chemistry A* **7**, 18807-18815 (2019).
- 25 Domanski, K., Alharbi, E. A., Hagfeldt, A., Grätzel, M. & Tress, W. Systematic investigation of the impact of operation conditions on the degradation behaviour of perovskite solar cells. *Nature Energy* **3**, 61-67 (2018).

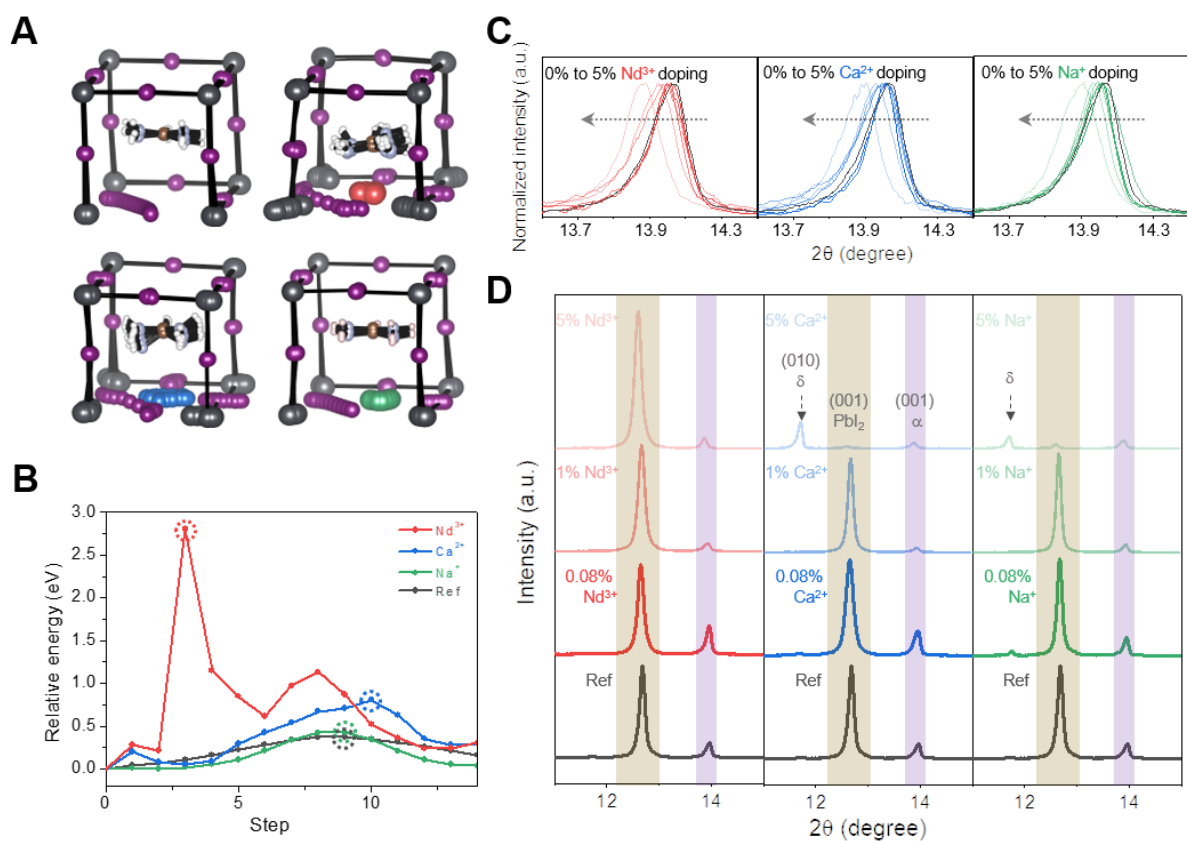


Figure 2.1 | (A) Theoretical models of iodide ion migration pathway in perovskite lattices without or with Nd^{3+} , Ca^{2+} , or Na^{+} at the interstitial site. (B) Relative energy landscapes of the system during the iodide ion migration. (C) a-FAPbI₃ (100) peaks from the XRD spectra of perovskite films as a function of Nd^{3+} , Ca^{2+} , and Na^{+} doping concentration from 0% to 5%. The arrows indicate a shift of the peak toward lower two theta angle with increasing dopant concentration (D) Comparison of the a-FAPbI₃, d-FAPbI₃, and PbI₂ phase variations from the XRD spectra of films with different Nd^{3+} , Ca^{2+} , and Na^{+} doping concentration.

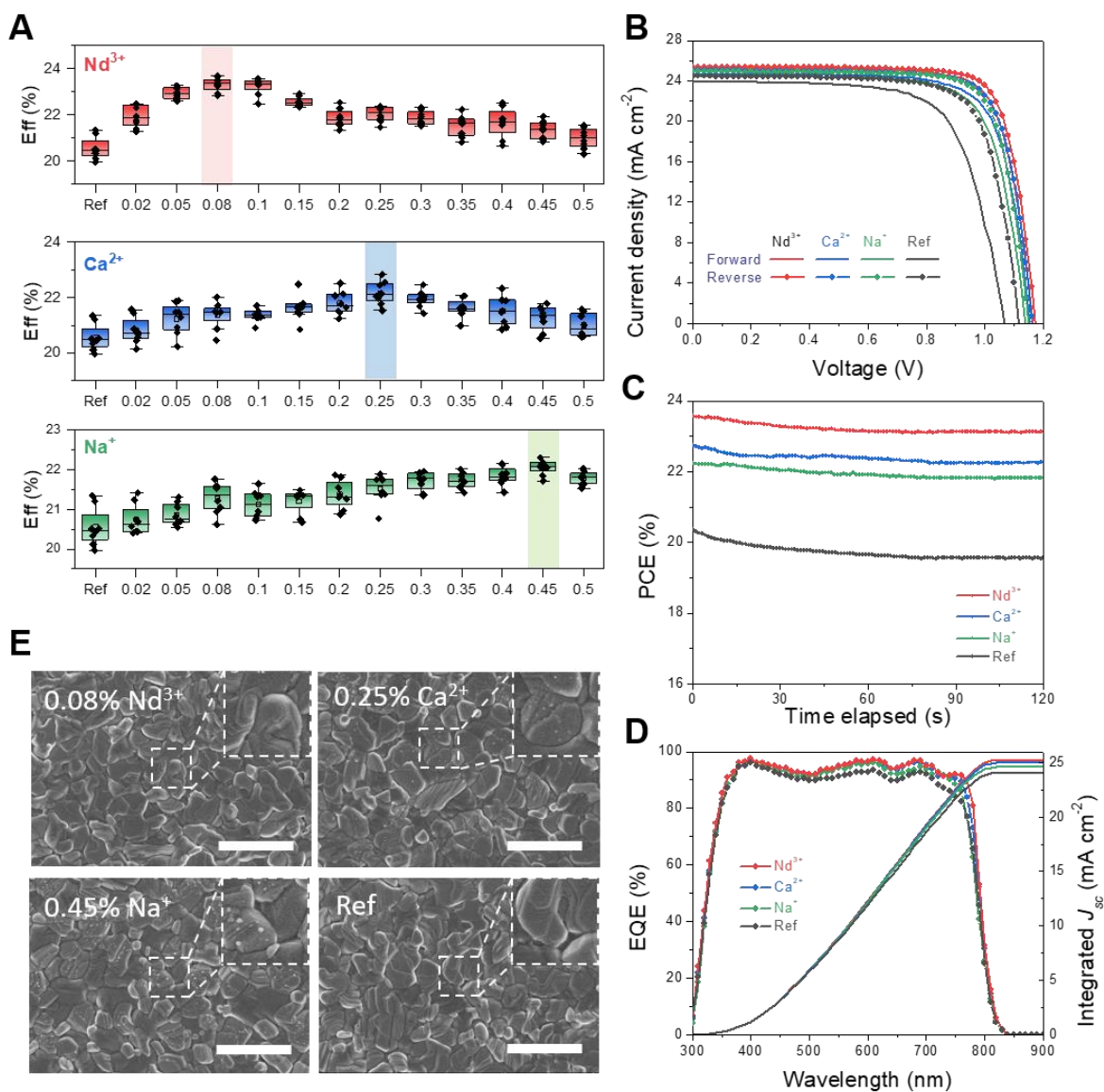


Figure 2.2 | (A) Statistical PCEs of devices with different concentrations of Nd^{3+} , Ca^{2+} , or Na^+ incorporation. The optimal concentrations to achieve the highest PCE for each dopant are highlighted. (B) J - V curves, (C) steady-state PCE measurement results and (D) EQE spectra of the best-performing devices for each condition. (E) SEM surface morphology of the perovskite films without or with the optimal cation doping concentration.

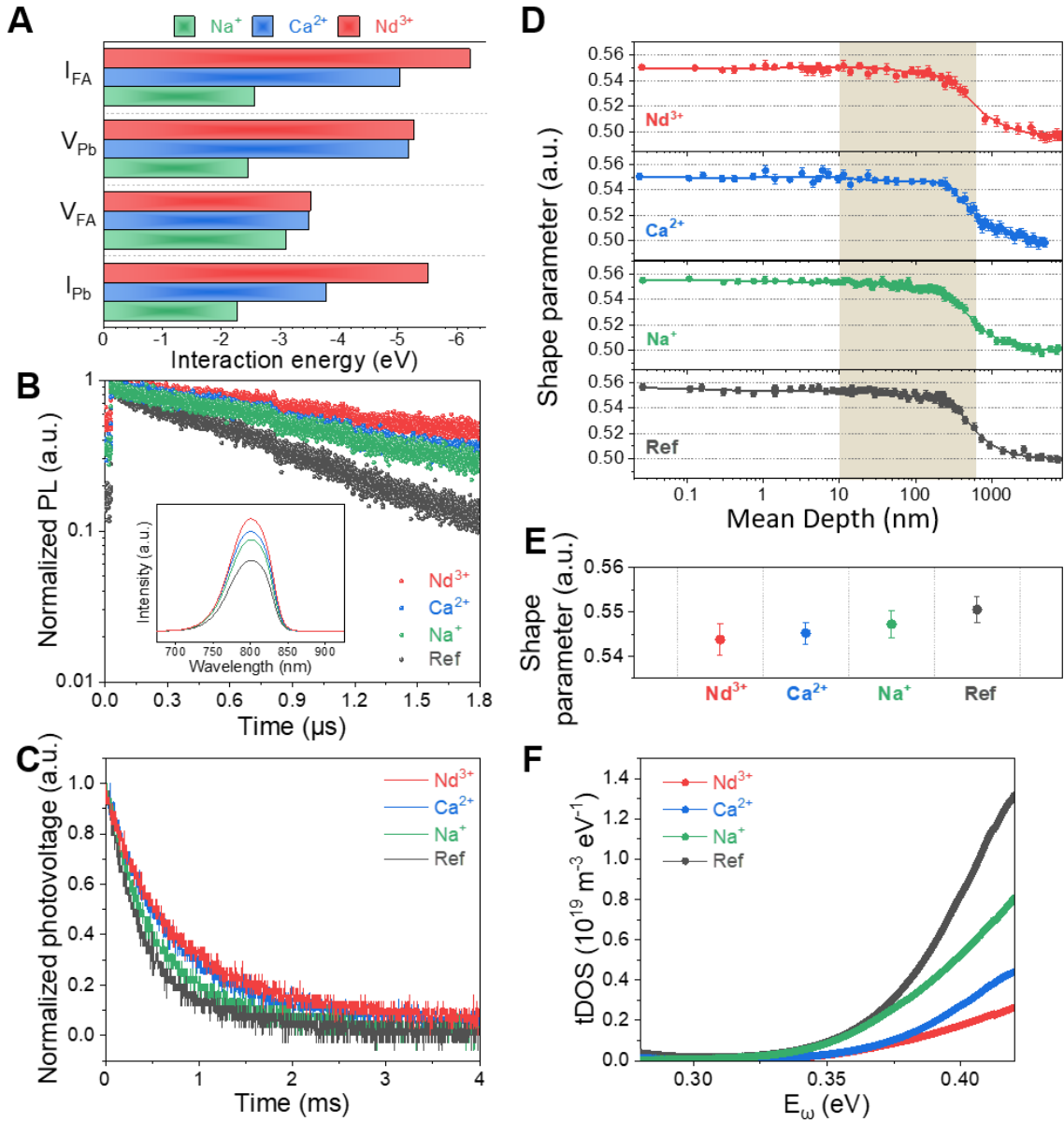


Figure 2.3 | (A) Interaction energies of Nd^{3+} , Ca^{2+} , or Na^+ cations incorporated in the perovskite lattices with the negatively charged defects. (B) Time-resolved PL spectra of perovskite films without or with the optimal cation doping concentrations (insert: corresponding steady-state spectra of perovskite films). (C) Transient photovoltage (TPV) curves of perovskite films without or with the optimal cation doping concentrations. (D) PAS depth-profiling of perovskite films without or with the optimal cation doping concentrations. Solid lines are fitted plots. Shaded areas

indicate the top surface region of the films. (E) Average shape parameters in the bulk region extracted from the PAS measurement (F) tDOS in perovskite solar cells with or without cation incorporation.

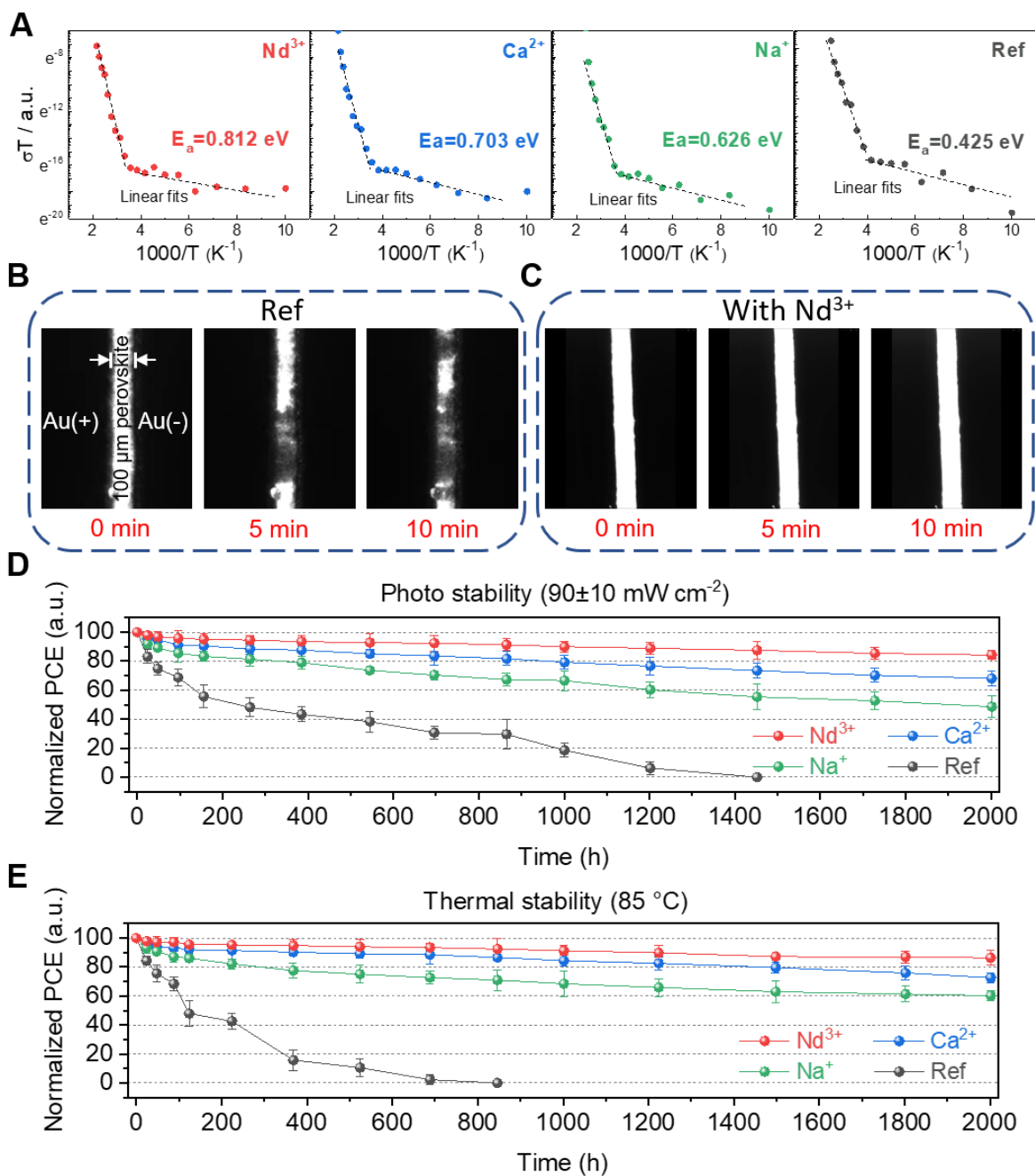


Figure 2.4 | (A) Temperature-dependent conductivity of the lateral devices with Nd^{3+} , Ca^{2+} , or Na^+ incorporations or without cation incorporation. Filled circles are measured data while dashed lines are fitted curves. (B, C) In situ PL images before and after applying an electric field of 150 $\text{mV}/\mu\text{m}$ under 440 nm illumination for 5 and 10 min for the lateral device based on (B) the

reference film and **(C)** the film incorporated with 0.08% Nd³⁺. **(D)** Photo stability of perovskite solar cells without or with the optimal cation doping concentrations. **(E)** Thermal stability of perovskite solar cells without or with the optimal cation doping concentrations.

Chapter 3 Passivation of the charged defect with rational additive selection

3.1 Introduction of the charged defect passivation

Metal halide perovskites have proven to be a competitive candidate as the light harvesting material in photovoltaic (PV) devices owing to their high defect tolerance, strong light absorption and excellent charge carrier transport ability.²⁶⁻³² In recent years, impressive advances have been achieved to increase the power conversion efficiency (PCE) of perovskite solar cells to a certified value of 25.2%.³³

Nevertheless, the poor stability of perovskite solar cells remains a major challenge, restraining its practical application.³⁴⁻³⁸ Thus, tremendous efforts have been made to enhance the operational longevity of perovskite solar cells, including encapsulation,³⁹⁻⁴⁰ phase stabilization,^{11, 41-42} interface engineering,⁴³⁻⁴⁵ and grain boundary passivation.⁴⁶⁻⁴⁸ Among these methods, defect passivation constitutes one of the most commonly used strategies to improve the stability of the perovskite solar cells.³⁷ The migration of charged defects in ionic perovskite crystals was found to be one of the critical factors deteriorating the operational stability of perovskite solar cells.⁴⁹ Such charged defects were reported to be effectively eliminated by the introduction of molecular passivation agents that neutralize the defects by secondary bonding.⁵⁰⁻⁵²

For instance, molecular additives with amino groups were widely utilized to passivate negatively charged defects due to its ability to interact with the defects via hydrogen bonding, while Lewis base additives with electron donating functional groups were frequently incorporated to coordinate with positively charged defects.⁵³⁻⁵⁵ Although numerous defect passivation molecules have been suggested,⁵⁶⁻⁶⁵ the lack of systematic studies on the role of different functional groups have hindered the establishment of general design rules for the passivation

molecules. Furthermore, the durability of the passivation effects has not been seriously considered regardless of the weak and vulnerable secondary bonding between the molecules and perovskite crystals. Such secondary bonding might be easily broken under the harsh operational conditions of the solar cells to degrade their passivation effects and result in diffusion and unintended reactions of the additives to severely undermine the operational stability of perovskite solar cells.

Herein, we incorporated strategically designed passivating agents to investigate the effect of their functional groups and thus interaction energies with the perovskite crystals, and correlate these with the performance and longevity of the passivation effects. Structurally similar amphiphilic amino acids with different Lewis base functional groups were chosen: 2-aminoethylphosphonic acid ($C_2H_8NO_3P$), 2-aminoethanesulfinic acid (hypotaurine, $C_2H_7NO_2S$), and 3-aminopropionic acid (β -alanine, $C_3H_7NO_2$). First-principles density-functional theory (DFT) calculations were utilized to simulate the interactions between the molecular additives and defective perovskite crystals, which were then experimentally verified by infrared spectroscopy and optoelectronic characterizations. The correlation between the molecular interactions, performance, and stability of the devices were further studied by fabricating the perovskite solar cells. Our device incorporated with the molecular additive with the strongest interaction energy with the perovskite demonstrated the best PCE of 22.35%, compared to the 20.46% of the reference device, and superior operational and thermal stability.

3.2 Investigation of molecular interactions between additives and defects

The molecular structures of the passivation agents adopted in this study are shown in **Figure A3.1**. Generally, all three additives have double-bonded Lewis base oxygen functional groups of either carbonyl (C=O), sulfinyl (S=O), or phosphonate (P=O) groups on one side of the molecule, and a

primary amino (NH_2) group on the other side. Due to the different Lewis base functional groups, we supposed that their interaction energies with positively charged defects might be different.

We first performed first-principles DFT calculations to investigate the interaction energies of the passivation agents with positively charged intrinsic defects in the perovskite crystals. Among the intrinsic defects, we selected two positively charged defects; iodine vacancies (V_I) and lead-iodine antisites (Pb_I). V_I was reported to have relatively low formation energy, so its equilibrium concentration in the film is expected to be high.⁶⁶⁻⁶⁸ Furthermore, although theoretical calculations suggest that V_I is shallow, it is susceptible to migrate under device operational conditions due to its relatively low activation energy for migration.⁶⁹ On the other hand, Pb_I has relatively higher formation energy and activation energy for migration, but is known to contribute to deep-level charge carriers traps, which could be detrimental to device performance by inducing non-radiative recombination losses. Based on the DFT calculations, the most stable configurations of the molecules to interact with V_I are first shown in **Figure 3.1a, d, g** and **A3.2**. As expected, the interactions are mainly dominated by the Lewis base $\text{P}=\text{O}$, $\text{S}=\text{O}$, and $\text{C}=\text{O}$ groups between the molecules and the crystal defects. Hereafter, we denote 2-aminoethylphosphonic acid, hypotaurine and β -alanine as PA, SA, and CA, respectively. The interaction energy between the V_I and PA, SA, and CA were calculated to be 1.09 eV, 0.66 eV, and 0.53 eV, respectively. The calculated interaction energy of PA, SA, and CA with Pb_I were 1.34 eV, 0.69 eV, and 0.43 eV, respectively, following the same trend as their interactions with V_I (**Figure A3.3** and **A3.4**).

We supposed that the difference in the interaction energies may have arose due to the different Lewis base functional groups of the molecules, which affects their coordination with positively charged defects. For confirmation of this hypothesis, we further investigated the molecular interactions between the additives and Lewis acid PbI_2 by using a combination of DFT calculations

and Fourier transform infrared (FT-IR) spectroscopy. The FT-IR spectroscopy measurements were performed on the pure additives (molecules) or PbI₂ films incorporated with the additives. From the FT-IR spectra of molecular CA, we observed the typical C=O stretching vibration mode at 1721 cm⁻¹ (**Figure 3.1h, i**). For the spectra of the CA-PbI₂ film (CA incorporated into PbI₂), a downwards shift to 1707 cm⁻¹ was observed, likely due to electron delocalization from the C=O group when a Lewis base-acid adduct formed. This is evidence for the interaction between the oxygen in the C=O group with PbI₂. Similarly, the S=O vibration stretch of molecular SA was 1326 cm⁻¹, and shifted to 1313 cm⁻¹ for SA-PbI₂ (**Figure 3.1e, f**). However, both shifts are evidently smaller than the shift of the P=O stretch corresponding to the spectra of PA and PA-PbI₂ films from 1143 cm⁻¹ to 1118 cm⁻¹ (**Figure 3.1b, c**). This probably indicates a much stronger interaction between PA and PbI₂ as a consequence of the stronger Lewis base character of PA. As a supplement to the FTIR data, we used X-ray photoelectron spectroscopy (XPS) analysis to further confirm the interaction between the additives and PbI₂. High-resolution XPS patterns of all the films showed two main peaks of Pb 4f. The peaks of the reference film without additive at 138.38 eV and 143.26 eV correspond to the Pb 4f 7/2 and Pb 4f 5/2, respectively (**Figure A3.5**). Meanwhile, the films with PA, SA, and CA additives had the peaks at 138.62 eV and 143.52 eV, 138.56 eV and 143.44 eV, and 138.47 eV and 143.37 eV, respectively. The peaks from Pb 4f shifted to higher binding energies in the film with additives, indicating the interaction between the additives and the Pb atoms. The shift of the film with PA was the largest among the ones with additives, which agrees with the results from FTIR measurement that the interaction between PA and PbI₂ is stronger than the others. This result is consistent with the atomic distances obtained from theoretical modeling of the Lewis acid-base adducts, where the distances between the oxygens in C=O, S=O, and P=O groups and Pb atoms were 2.36 Å, 2.42 Å and 2.58 Å, respectively.

The same trend in binding energy between the additives and PbI_2 was observed when we investigated the adduct formation in the precursor solutions (**Figure A3.6**). The corresponding adduct interaction energies with PA, SA, and CA are 1.07 eV, 0.89 eV, and 0.39 eV, respectively.

Compared to the electronegativity of atomic sulfur (2.58, Pauling scale) and carbon (2.55), atomic phosphor has a much lower electronegativity (2.19), which indicates its lower tendency to attract electrons from the adjacent oxygen. Therefore, the stronger localized negative charge on the oxygen might contribute to the higher interaction energy of PA with positively charged V_I . For CA and SA, although the electronegativity of sulfur and carbon atoms are similar, the sulfur atom in SA has an additional lone pair electron in its outermost shell, which repel the electron cloud towards the oxygen atom to result in the higher interaction energy of SA with Lewis acids (for example, lead ions) and positively charge defects than that of CA.

3.3 Defect passivation effect based on the different additives

To check the defect passivation effects of the three discussed additives, perovskite films without and with the additives were fabricated. Atomic force microscopy (AFM) images of the perovskite films in **Figure 3.2a-d** show that the morphology of all films was similar. The slightly larger grain sizes of the films with additives should attributed to the interaction between the additives and precursors during the crystallization of the perovskite. The photoluminescence (PL) intensity of the films incorporated with the additives was obviously higher than that of the bare film as shown in the confocal laser scanning fluorescence microscopy (CLSM) images in **Figure 3.2e**. All the additive-containing films showed enhanced steady-state PL intensity without any noticeable shifts in their peak positions (**Figure A3.7**). The peak steady-state PL intensity of the PA-, SA-, and CA-incorporated films were measured to be 9.91×10^6 , 8.45×10^6 , and 6.76×10^6 , which were all

significantly enhanced relative to that of the bare film (5.75×10^6). To elucidate the origin of the enhanced PL intensity, the time-resolved PL (TRPL) decay of the films was measured in **Figure 3.2f**. The decay curves were fitted to a single exponential decay model to quantify the PL lifetime. The fitted parameters are summarized in **Table 3.1**. Overall, we observed an elongation of the PL lifetime for the films with the three additives compared with the reference perovskite film; the PL lifetimes of the PA (2.89 μ s), SA (1.58 μ s), and CA (0.95 μ s) films were significantly longer than that of reference sample (0.51 μ s). The elongated PL lifetime indicates a reduced defect density with incorporation of any of the additives, promoting charge carrier transport with reduced non-radiative recombination loss.⁷⁰ Notably, the measured PL intensity and lifetime are closely correlated with the calculated interaction energy, implying that the molecular interaction strength plays a vital role in the defect passivation effectiveness.

Further, we utilized the space-charge-limited-current (SCLC) technique to quantify the defect density in the perovskite films incorporated with the different passivation agents. Electron-only devices with a structure of ITO/SnO₂/perovskite/PCBM/Ag and hole-only devices with a structure of ITO/perovskite/Au were both fabricated for this (**Figure 3.3c**). The corresponding current-voltage curves for both device types are shown in **Figure 3.3a, b**. The trap density (N_t) can be calculated from the equation $V_{TFL} = \frac{eN_t L^2}{2\epsilon\epsilon_0}$, where e is the elementary charge, L the perovskite film thickness, ϵ the relative dielectric constant, ϵ_0 the vacuum permittivity and V_{TFL} the trap-filling voltage. Accordingly, the electron and hole trap densities close to the VBM and CBM are calculated and summarized in **Figure 3.3d** and **Table 3.1**. The perovskite films passivated by PA show the lowest values in both cases ($2.40 \times 10^{15} \text{ cm}^{-3}$ for electron defects and $2.28 \times 10^{15} \text{ cm}^{-3}$ for hole defects), significantly lower than that of the reference sample without any additives ($8.04 \times 10^{15} \text{ cm}^{-3}$ for electron defects and $9.48 \times 10^{15} \text{ cm}^{-3}$ for hole defects), which was followed by

SA and CA films. The SCLC results supports our previous discussion that the elongated PL lifetime with incorporation of the additives is due to the reduced defect density of the films.

3.4 Photovoltaic performances of perovskite solar cells with the additives

Complete solar cell devices were fabricated with SnO₂ as the electron transport layer and spiro-OMeTAD as the hole transport layer. We compared the photovoltaic performance of the devices incorporated with either PA, SA, or CA (**Figure 3.4a**). The measured photovoltaic parameters are summarized in **Table 3.1**. We noticed a distinct improvement in open-circuit voltage (V_{oc}) and fill factor (FF) with incorporation of the amino-acid additives. The devices containing PA, SA, and CA achieved averaged V_{OC} s of 1.148 V, 1.140 V, and 1.126 V, respectively, and averaged FF of 78.66%, 77.23%, and 76.75%, respectively. These parameters are considerably higher than the reference devices without any additives (V_{OC} :1.109 V, FF: 75.27%). The enhancements in V_{OC} and FF might have originated from the defect passivation by the additives in the perovskite layer, which led to reduced charge carrier recombination and more efficient charge transport.⁷¹ Furthermore, a close correlation between the performance enhancement, defect density and interaction energies was observed. The corresponding incident photon-to-electron conversion efficiency (IPCE) curves were presented in **Figure 3.4b**, where the integrated current densities from the IPCE spectrum were 23.89 mA/cm², 24.29 mA/cm², 24.25 mA/cm², and 24.14 mA/cm², for the reference devices and devices incorporated with PA, SA, and CA, respectively. These values match well with the J_{SC} values obtained from the J - V scans with less than 2.6% discrepancy. The PA devices achieved a stabilized power output (SPO) of 22.17%, while the reference, SA, and CA devices had SPOs of 20.01%, 21.27%, and 20.44%, respectively (**Figure 3.4c**). The transient photovoltage (TPV) decay curves under open-circuit condition show substantially longer charge-recombination lifetimes for

the devices with passivation agents (**Figure 3.4d**). The fitted time constants for reference, PA-, SA-, and CA-incorporated devices were 0.17 ms, 0.65 ms, 0.47 ms, and 0.36 ms, respectively. The observed trend matches that of the PL lifetime, defect density and performance enhancement.

We further utilized thermal admittance spectroscopy to cross-check the observed defect density trend in the devices. The trap density was estimated from the angular-frequency-dependent capacitance according to the following equation: $N_T = -\frac{V_{bi}}{qW} \frac{dC}{d\omega} \frac{\omega}{kT}$, where V_{bi} is the built-in potential, C is the capacitance, ω is the angular frequency, q is the elementary charge, W is the perovskite depletion width, k is the Boltzmann constant and T is the temperature. The calculated trap densities are shown in **Figure 3.4e**, where the PA-incorporated device exhibited the lowest values, followed by SA, CA, and reference samples, consistent with the results obtained from the SCLC measurements. Electrochemical impedance spectroscopy (EIS) characterizations were performed to investigate the carrier transport processes at the interface (**Figure 3.4f**). In the Nyquist plot, the radius of the first semicircle is generally assigned to charge transport resistance (R_{CT}).⁷² The radius of the first semicircle is systematically reduced with stronger interaction energy (PA<SA<CA<reference), indicating the facilitated charge transport with better defect passivation, which probably contributed to the enhanced FF.

3.5 Operational and thermal stability correlated with ion migration energetics

To investigate the effects of the amino-acid agents on the operational stability of the solar cell devices, we exposed the encapsulated devices to continuous illumination under open-circuit condition. Defect migration is expected to be the most severe under open-circuit condition (versus maximum power point tracking) due to the uncompensated built-in potential induced by illumination.²⁵ After 1008 h of exposure, the reference device almost completely degraded: 0% of

its initial PCE. Notably, the encapsulated device incorporated with PA maintained 81.9% of its initial PCE after continuous illumination for 1008 hours while the devices incorporated with SA and CA retained 50.1% and 37.9% of the initial PCEs, respectively (**Figure 3.5a**). To further investigate the thermal stability of the devices, we kept the unencapsulated devices in a nitrogen filled glove box at 85 °C. After 1008 hours, we observed that the devices incorporated with PA maintained the highest PCE (retaining 85.3% of its initial PCE) relative to the other devices (**Figure 3.5b**). The reference, SA-, and CA-incorporated devices retained 0%, 48.5%, and 24.2% of their initial PCEs, respectively. The observed trend in device stability indicates that the passivation agents with a stronger interaction with the perovskite crystals might be beneficial not only for defect passivation, but also for suppression of defect migration during the elongated stress tests under such harsh operational conditions. The strongly coordinated charged defects by the passivation agents probably remained impervious to the potential gradient due to its compensated charge and higher effective mass.

To verify the effect of the additives on the ion migration energetics, we investigated the ion migration properties of the films with and without the additives via direct current (DC) temperature-dependent conductivity measurements on lateral perovskite devices with structure of Au/perovskite (100 μm)/Au (**Figure A3.8**). The activation energy (E_a) of ion migration can be extracted by linear fitting of the data based on the Nernst–Einstein equation given by $\sigma(T) = \frac{\sigma_0}{T} \exp\left(\frac{-E_a}{k_b T}\right)$, where $\sigma(T)$ is the conductivity as a function of temperature T , σ_0 is a constant, k_b is Boltzmann constant. The E_a for ion migration was extracted from the slope of the fitted lines at relatively higher temperature. The calculated E_a for the films incorporated with PA, SA, CA were 0.68 eV, 0.63 eV, and 0.59 eV, respectively, which are substantially higher than that of the reference film (0.27 eV). The higher activation energy of ion migration indicates defect migration

in the perovskite films is hindered by the additives, which can be attributed to strengthened interaction between the defects and passivation agents. The trend of the measured E_a agrees well with the operational and thermal stability of the devices; the passivation agents more inhibitory to the defect migration provide more enhanced longevity of the devices under continuous illumination and heat.

3.5 Summary and conclusion

In this work, we utilized three different amino-acid molecules with similar structures but different functional groups to investigate the correlation between their interaction energies with perovskite crystal defects, and correlate these with the resultant performance and stability of the defect passivation effect on the devices. It was found that different functional groups regulate the molecular interactions between the passivation agents and crystal defects to affect the interaction energy. Molecular PA, with its stronger localized negative charge on its electron donating oxygen atom, exhibited higher interaction energy with positively charged defects, resulting in a greater passivation effect to reduce the defect density in the perovskite film. Owing to the reduced defect density, the device incorporated with PA demonstrated significantly improved PCE of 22.35%, compared to the 20.46% of the reference device. More importantly, we found that the stronger interaction of the passivation agents is beneficial for the longevity of the passivation effect under device operational conditions. The devices with PA, with the strongest interaction energy, retained 81.9% and 85.3% of their initial PCE under continuous illumination or nitrogen at 85 °C after 1008 hours, respectively, while the reference device completely degraded during the time. We can conclude that for the additives with confirmed passivation effect to the perovskite crystals and similar molecular structures, the interaction energy should play a crucial role to determine the

longevity of the passivation effect. Meanwhile, further research should be implemented to figure out the favorable molecular structure for effective and durable passivation of perovskite defects. Our work highlights the importance of considering the interaction energy to design operationally durable defect passivation agents for perovskite optoelectronics.

References

1. Lee, M. M.; Teuscher, J.; Miyasaka, T.; Murakami, T. N.; Snaith, H. J., Efficient hybrid solar cells based on meso-superstructured organometal halide perovskites. *Science* **2012**, *338* (6107), 643-647.
2. Yang, W. S.; Park, B.-W.; Jung, E. H.; Jeon, N. J.; Kim, Y. C.; Lee, D. U.; Shin, S. S.; Seo, J.; Kim, E. K.; Noh, J. H., Iodide management in formamidinium-lead-halide-based perovskite layers for efficient solar cells. *Science* **2017**, *356* (6345), 1376-1379.
3. Stranks, S. D.; Eperon, G. E.; Grancini, G.; Menelaou, C.; Alcocer, M. J.; Leijtens, T.; Herz, L. M.; Petrozza, A.; Snaith, H. J., Electron-hole diffusion lengths exceeding 1 micrometer in an organometal trihalide perovskite absorber. *Science* **2013**, *342* (6156), 341-344.
4. Xing, G.; Mathews, N.; Sun, S.; Lim, S. S.; Lam, Y. M.; Grätzel, M.; Mhaisalkar, S.; Sum, T. C., Long-range balanced electron-and hole-transport lengths in organic-inorganic CH₃NH₃PbI₃. *Science* **2013**, *342* (6156), 344-347.
5. Dong, Q.; Fang, Y.; Shao, Y.; Mulligan, P.; Qiu, J.; Cao, L.; Huang, J., Electron-hole diffusion lengths > 175 μm in solution-grown CH₃NH₃PbI₃ single crystals. *Science* **2015**, *347* (6225), 967-970.

6. Park, N.-G., Perovskite solar cells: an emerging photovoltaic technology. *Materials today* **2015**, *18* (2), 65-72.
7. Jung, H. S.; Park, N. G., Perovskite solar cells: from materials to devices. *small* **2015**, *11* (1), 10-25.
8. <https://www.nrel.gov/pv/assets/pdfs/best-research-cell-efficiencies.20190802.pdf>.
9. Yang, Y.; You, J., Make perovskite solar cells stable. *Nature News* **2017**, *544* (7649), 155.
10. Park, N. G., Research direction toward scalable, stable, and high efficiency perovskite solar cells. *Advanced Energy Materials* **2020**, *10* (13), 1903106.
11. Lee, J.-W.; Bae, S.-H.; De Marco, N.; Hsieh, Y.-T.; Dai, Z.; Yang, Y., The role of grain boundaries in perovskite solar cells. *Materials Today Energy* **2018**, *7*, 149-160.
12. Gao, F.; Zhao, Y.; Zhang, X.; You, J., Recent progresses on defect passivation toward efficient perovskite solar cells. *Advanced Energy Materials* **2020**, *10* (13), 1902650.
13. Zhao, Y.; Ma, F.; Gao, F.; Yin, Z.; Zhang, X.; You, J., Research progress in large-area perovskite solar cells. *Photonics Research* **2020**, *8* (7), A1-A15.
14. Lee, Y. I.; Jeon, N. J.; Kim, B. J.; Shim, H.; Yang, T. Y.; Seok, S. I.; Seo, J.; Im, S. G., A low-temperature thin-film encapsulation for enhanced stability of a highly efficient perovskite solar cell. *Advanced Energy Materials* **2018**, *8* (9), 1701928.
15. Wang, H.; Zhao, Y.; Wang, Z.; Liu, Y.; Zhao, Z.; Xu, G.; Han, T.-H.; Lee, J.-W.; Chen, C.; Bao, D., Hermetic seal for perovskite solar cells: An improved plasma enhanced atomic layer deposition encapsulation. *Nano Energy* **2020**, *69*, 104375.
16. Lee, J.-W.; Dai, Z.; Han, T.-H.; Choi, C.; Chang, S.-Y.; Lee, S.-J.; De Marco, N.; Zhao, H.; Sun, P.; Huang, Y., 2D perovskite stabilized phase-pure formamidinium perovskite solar cells. *Nature communications* **2018**, *9* (1), 3021.

17. Jodlowski, A. D.; Roldán-Carmona, C.; Grancini, G.; Salado, M.; Ralaiarisoa, M.; Ahmad, S.; Koch, N.; Camacho, L.; De Miguel, G.; Nazeeruddin, M. K., Large guanidinium cation mixed with methylammonium in lead iodide perovskites for 19% efficient solar cells. *Nature Energy* **2017**, *2* (12), 972-979.
18. Tan, S.; Yavuz, I.; De Marco, N.; Huang, T.; Lee, S. J.; Choi, C. S.; Wang, M.; Nuryyeva, S.; Wang, R.; Zhao, Y., Steric Impediment of Ion Migration Contributes to Improved Operational Stability of Perovskite Solar Cells. *Advanced Materials* **2020**, *32* (11), 1906995.
19. Chen, W.; Wu, Y.; Yue, Y.; Liu, J.; Zhang, W.; Yang, X.; Chen, H.; Bi, E.; Ashraful, I.; Grätzel, M., Efficient and stable large-area perovskite solar cells with inorganic charge extraction layers. *Science* **2015**, *350* (6263), 944-948.
20. Jiang, Q.; Zhao, Y.; Zhang, X.; Yang, X.; Chen, Y.; Chu, Z.; Ye, Q.; Li, X.; Yin, Z.; You, J., Surface passivation of perovskite film for efficient solar cells. *Nature Photonics* **2019**, *13* (7), 460-466.
21. Yang, D.; Yang, R.; Wang, K.; Wu, C.; Zhu, X.; Feng, J.; Ren, X.; Fang, G.; Priya, S.; Liu, S. F., High efficiency planar-type perovskite solar cells with negligible hysteresis using EDTA-complexed SnO₂. *Nature communications* **2018**, *9* (1), 1-11.
22. Wang, R.; Xue, J.; Meng, L.; Lee, J.-W.; Zhao, Z.; Sun, P.; Cai, L.; Huang, T.; Wang, Z.; Wang, Z.-K., Caffeine Improves the Performance and Thermal Stability of Perovskite Solar Cells. *Joule* **2019**, *3* (6), 1464-1477.
23. Zhao, Y.; Zhu, P.; Wang, M.; Huang, S.; Zhao, Z.; Tan, S.; Han, T. H.; Lee, J. W.; Huang, T.; Wang, R., A Polymerization-Assisted Grain Growth Strategy for Efficient and Stable Perovskite Solar Cells. *Advanced Materials* **2020**, *32* (17), 1907769.

24. Niu, T.; Lu, J.; Munir, R.; Li, J.; Barrit, D.; Zhang, X.; Hu, H.; Yang, Z.; Amassian, A.; Zhao, K., Stable High-Performance Perovskite Solar Cells via Grain Boundary Passivation. *Advanced Materials* **2018**, *30* (16), 1706576.
25. Lee, J. W.; Park, N. G., Chemical Approaches for Stabilizing Perovskite Solar Cells. *Advanced Energy Materials* **2020**, *10* (1), 1903249.
26. Han, T.-H.; Lee, J.-W.; Choi, C.; Tan, S.; Lee, C.; Zhao, Y.; Dai, Z.; De Marco, N.; Lee, S.-J.; Bae, S.-H., Perovskite-polymer composite cross-linker approach for highly-stable and efficient perovskite solar cells. *Nature communications* **2019**, *10* (1), 520.
27. Lee, J.-W.; Bae, S.-H.; Hsieh, Y.-T.; De Marco, N.; Wang, M.; Sun, P.; Yang, Y., A bifunctional lewis base additive for microscopic homogeneity in perovskite solar cells. *Chem* **2017**, *3* (2), 290-302.
28. Niu, T.; Lu, J.; Tang, M.-C.; Barrit, D.; Smilgies, D.-M.; Yang, Z.; Li, J.; Fan, Y.; Luo, T.; McCulloch, I., High performance ambient-air-stable FAPbI₃ perovskite solar cells with molecule-passivated Ruddlesden–Popper/3D heterostructured film. *Energy & Environmental Science* **2018**, *11* (12), 3358-3366.
29. Wang, R.; Mujahid, M.; Duan, Y.; Wang, Z. K.; Xue, J.; Yang, Y., A review of perovskites solar cell stability. *Advanced Functional Materials* **2019**, *29* (47), 1808843.
30. Yang, S.; Dai, J.; Yu, Z.; Shao, Y.; Zhou, Y.; Xiao, X.; Zeng, X. C.; Huang, J., Tailoring passivation molecular structures for extremely small open-circuit voltage loss in perovskite solar cells. *Journal of the American Chemical Society* **2019**, *141* (14), 5781-5787.
31. Wang, R.; Xue, J.; Wang, K.-L.; Wang, Z.-K.; Luo, Y.; Fenning, D.; Xu, G.; Nuryyeva, S.; Huang, T.; Zhao, Y., Constructive molecular configurations for surface-defect passivation of perovskite photovoltaics. *Science* **2019**, *366* (6472), 1509-1513.

32. Kim, M.; Motti, S. G.; Sorrentino, R.; Petrozza, A., Enhanced solar cell stability by hygroscopic polymer passivation of metal halide perovskite thin film. *Energy & Environmental Science* **2018**, *11* (9), 2609-2619.
33. Peng, J.; Khan, J. I.; Liu, W.; Ugur, E.; Duong, T.; Wu, Y.; Shen, H.; Wang, K.; Dang, H.; Aydin, E., A Universal Double-Side Passivation for High Open-Circuit Voltage in Perovskite Solar Cells: Role of Carbonyl Groups in Poly (methyl methacrylate). *Advanced Energy Materials* **2018**, *8* (30), 1801208.
34. Li, B.; Zhang, Y.; Fu, L.; Yu, T.; Zhou, S.; Zhang, L.; Yin, L., Surface passivation engineering strategy to fully-inorganic cubic CsPbI₃ perovskites for high-performance solar cells. *Nature communications* **2018**, *9* (1), 1-8.
35. Tai, Q.; Guo, X.; Tang, G.; You, P.; Ng, T. W.; Shen, D.; Cao, J.; Liu, C. K.; Wang, N.; Zhu, Y., Antioxidant grain passivation for air-stable tin-based perovskite solar cells. *Angewandte Chemie International Edition* **2019**, *58* (3), 806-810.
36. Chen, W.; Wang, Y.; Pang, G.; Koh, C. W.; Djurišić, A. B.; Wu, Y.; Tu, B.; Liu, F. z.; Chen, R.; Woo, H. Y., Conjugated Polymer-Assisted Grain Boundary Passivation for Efficient Inverted Planar Perovskite Solar Cells. *Advanced Functional Materials* **2019**, *29* (27), 1808855.
37. Huang, Z.; Hu, X.; Liu, C.; Meng, X.; Huang, Z.; Yang, J.; Duan, X.; Long, J.; Zhao, Z.; Tan, L., Water-Resistant and Flexible Perovskite Solar Cells via a Glued Interfacial Layer. *Advanced Functional Materials* **2019**, *29* (37), 1902629.
38. Gao, L.; Huang, S.; Chen, L.; Li, X.; Ding, B.; Huang, S.; Yang, G., Excellent stability of perovskite solar cells by passivation engineering. *Solar RRL* **2018**, *2* (8), 1800088.

39. Zhang, H.; Wu, Y.; Shen, C.; Li, E.; Yan, C.; Zhang, W.; Tian, H.; Han, L.; Zhu, W. H., Efficient and stable chemical passivation on perovskite surface via bidentate anchoring. *Advanced Energy Materials* **2019**, *9* (13), 1803573.
40. Zhang, Y.; Grancini, G.; Fei, Z.; Shirzadi, E.; Liu, X.; Oveisi, E.; Tirani, F. F.; Scopelliti, R.; Feng, Y.; Nazeeruddin, M. K., Auto-passivation of crystal defects in hybrid imidazolium/methylammonium lead iodide films by fumigation with methylamine affords high efficiency perovskite solar cells. *Nano Energy* **2019**, *58*, 105-111.
41. Tavakoli, M. M.; Bi, D.; Pan, L.; Hagfeldt, A.; Zakeeruddin, S. M.; Grätzel, M., Adamantanes enhance the photovoltaic performance and operational stability of perovskite solar cells by effective mitigation of interfacial defect states. *Advanced Energy Materials* **2018**, *8* (19), 1800275.
42. Liu, N.; Yam, C., First-principles study of intrinsic defects in formamidinium lead triiodide perovskite solar cell absorbers. *Physical Chemistry Chemical Physics* **2018**, *20* (10), 6800-6804.
43. Petrus, M. L.; Schlipf, J.; Li, C.; Gujar, T. P.; Giesbrecht, N.; Müller-Buschbaum, P.; Thelakkat, M.; Bein, T.; Hüttner, S.; Docampo, P., Capturing the sun: A review of the challenges and perspectives of perovskite solar cells. *Advanced Energy Materials* **2017**, *7* (16), 1700264.
44. Wang, F.; Bai, S.; Tress, W.; Hagfeldt, A.; Gao, F., Defects engineering for high-performance perovskite solar cells. *npj Flexible Electronics* **2018**, *2* (1), 1-14.
45. Eames, C.; Frost, J. M.; Barnes, P. R.; O'regan, B. C.; Walsh, A.; Islam, M. S., Ionic transport in hybrid lead iodide perovskite solar cells. *Nature communications* **2015**, *6*, 7497.
46. Shi, D.; Adinolfi, V.; Comin, R.; Yuan, M.; Alarousu, E.; Buin, A.; Chen, Y.; Hoogland, S.; Rothenberger, A.; Katsiev, K., Low trap-state density and long carrier diffusion in organolead trihalide perovskite single crystals. *Science* **2015**, *347* (6221), 519-522.

47. Park, N.-G.; Grätzel, M.; Miyasaka, T.; Zhu, K.; Emery, K., Towards stable and commercially available perovskite solar cells. *Nature Energy* **2016**, *1* (11), 1-8.
48. Galatopoulos, F.; Savva, A.; Papadas, I. T.; Choulis, S. A., The effect of hole transporting layer in charge accumulation properties of pin perovskite solar cells. *APL Materials* **2017**, *5* (7), 076102.
49. Domanski, K.; Alharbi, E. A.; Hagfeldt, A.; Grätzel, M.; Tress, W., Systematic investigation of the impact of operation conditions on the degradation behaviour of perovskite solar cells. *Nature Energy* **2018**, *3* (1), 61-67.

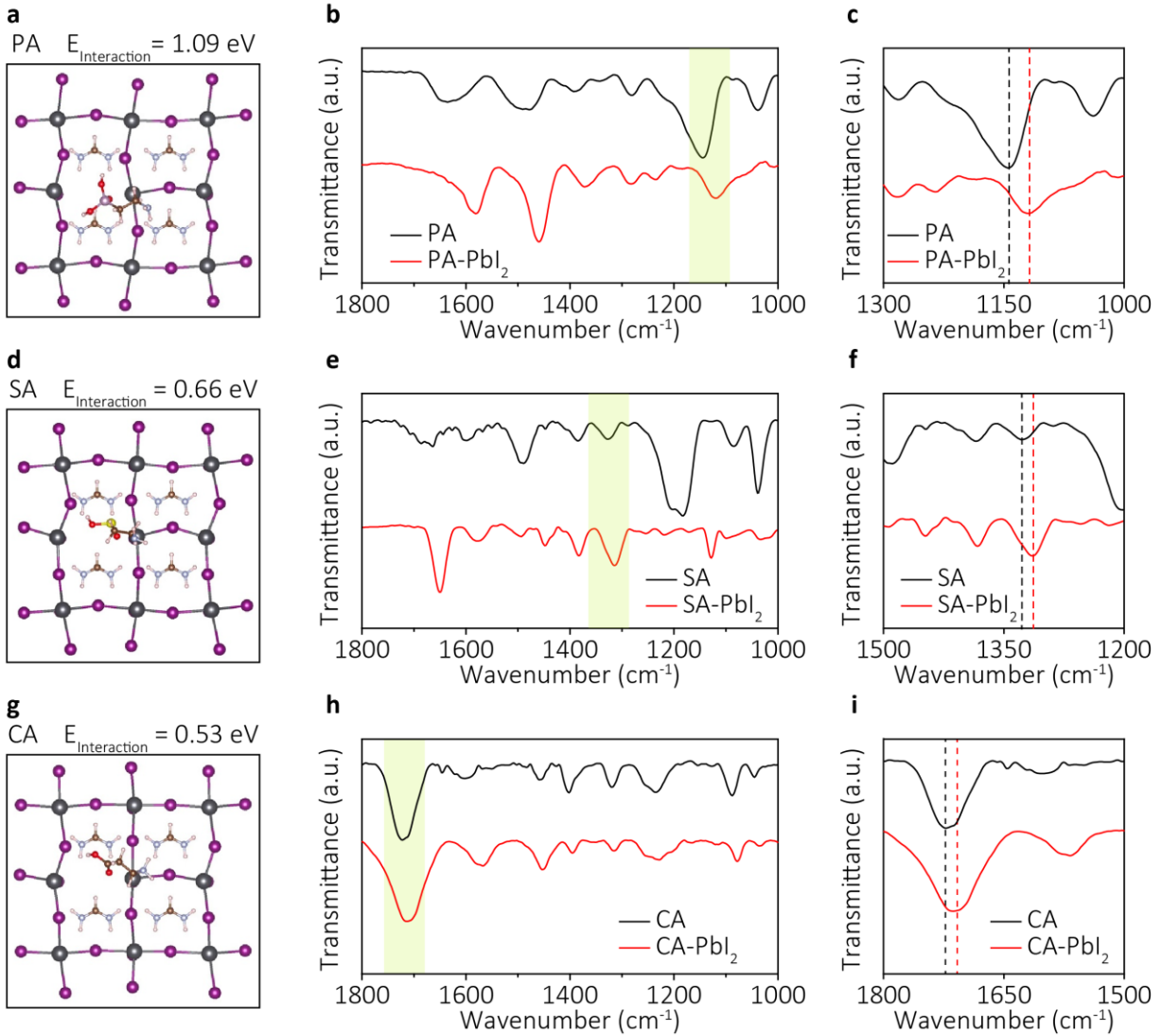


Figure 3.1 | Theoretical models of perovskite with molecular surface passivation of V_I defects with **a).** 2-aminoethylphosphonic acid (PA), **d).** hypotaurine (SA), and **g).** β -alanine (CA). FTIR spectra of **b)-c).** pure PA and PbI₂ film with PA, **e)-f).** pure SA and PbI₂ film with SA, and **h)-i).** pure CA and PbI₂ film with CA.

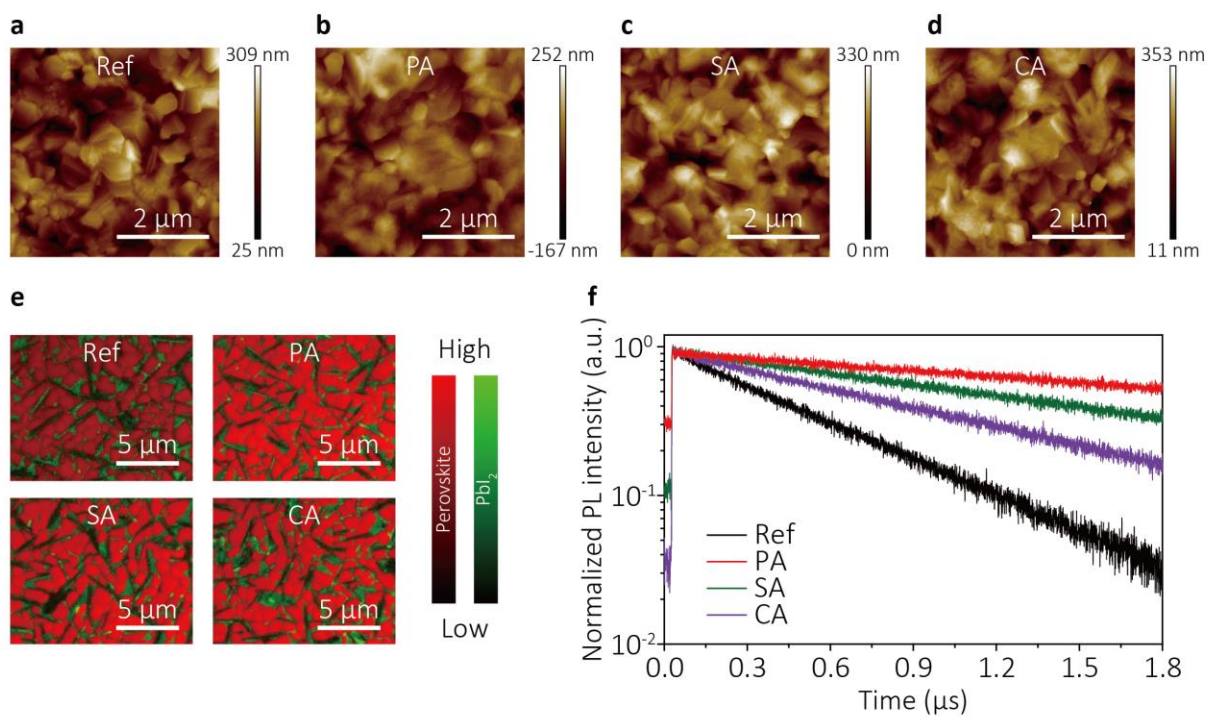


Figure 3.2 | a)-d). Atomic force microscopy (AFM) images of perovskite films with or without additives. **e).** Confocal laser scanning fluorescence microscopy (CLSM) images of perovskite films with or without additives. **f).** Time-resolved PL spectra of perovskite films with 2-aminoethylphosphonic acid (PA), hypotaaurine (SA) and β -alanine additives (CA) or without additives.

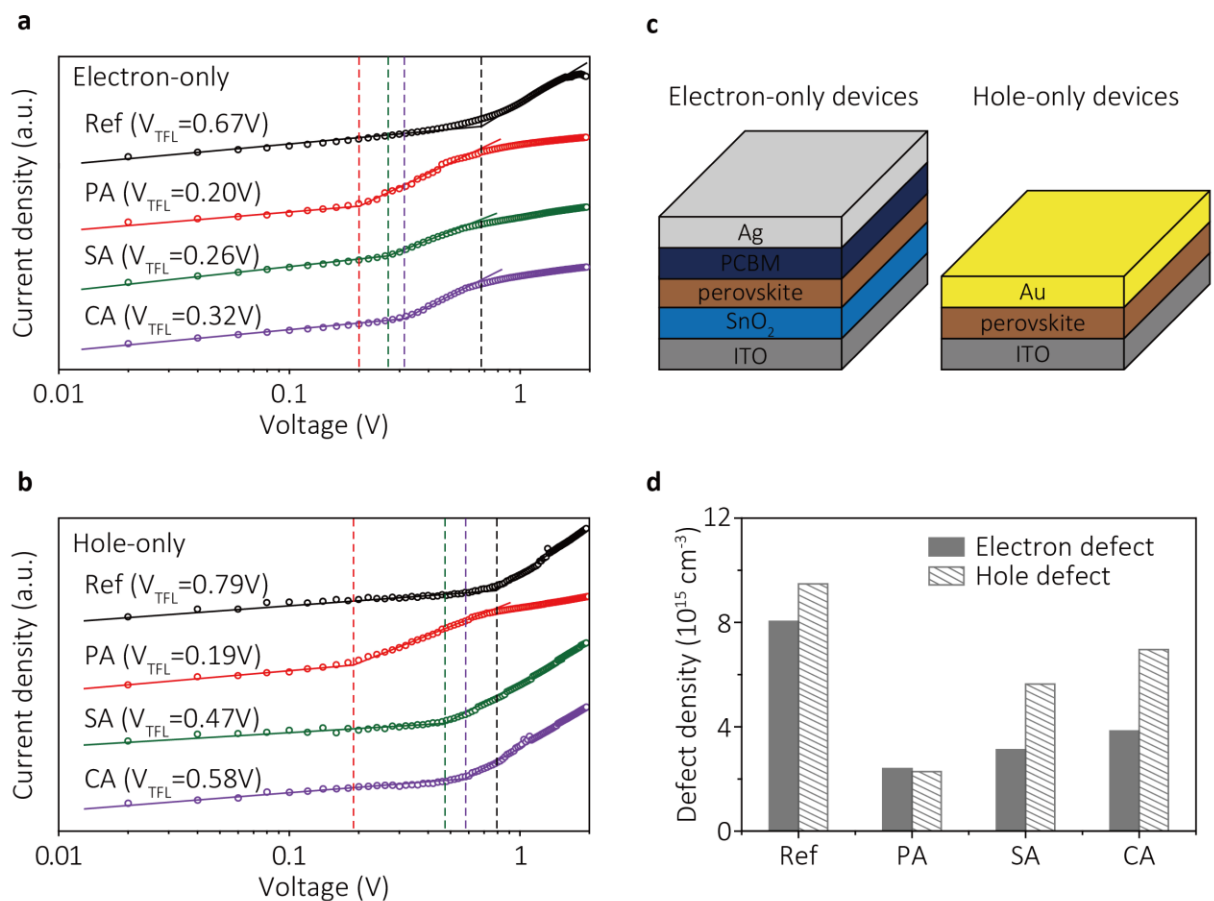


Figure 3.3 | a). Space-charge-limited-current (SCLC) measurements of electron-only devices based on perovskite films with 2-aminoethylphosphonic acid (PA), hypotaurine (SA) and β -alanine additives (CA) or without additives. **b).** SCLC measurements of hole-only devices based on perovskite films with or without additives. **c).** Device configurations of SCLC measurements. **d).** Defect density calculated from SCLC measurement with or without additives.

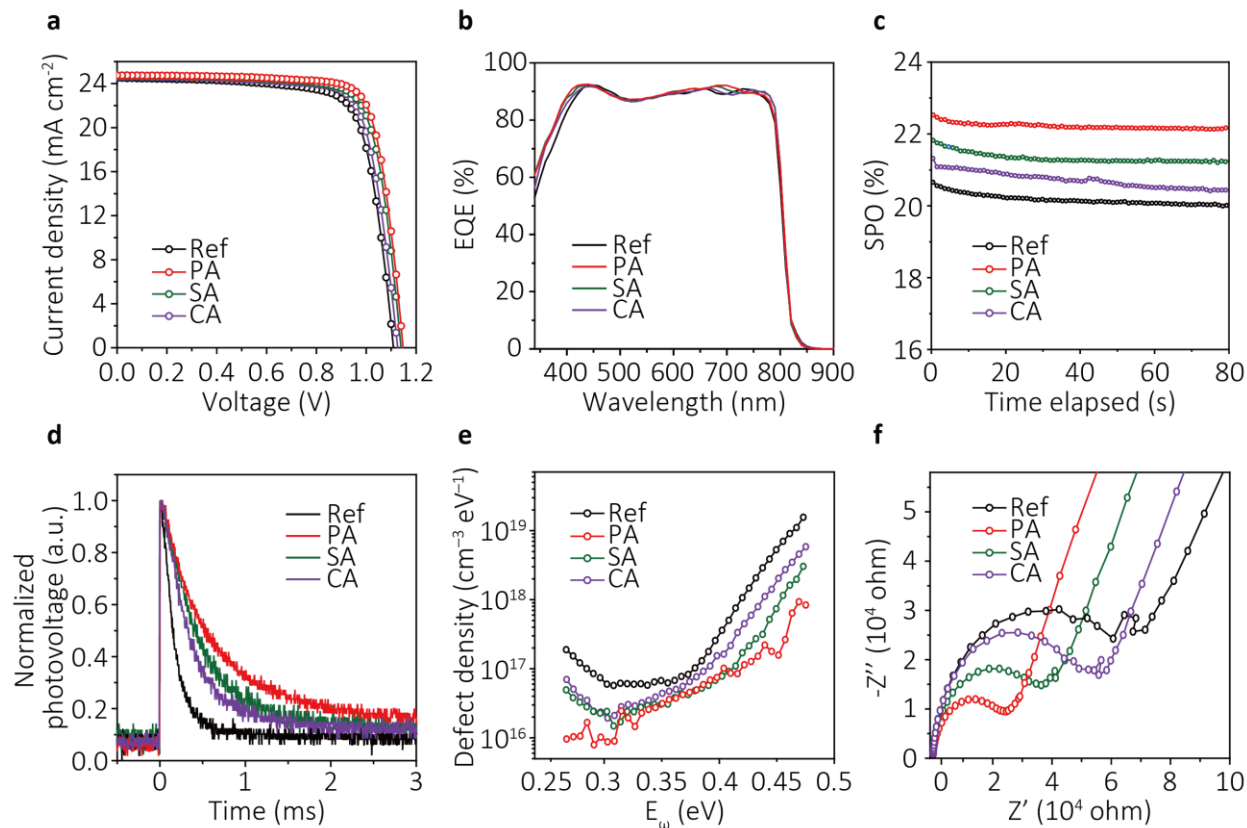


Figure 3.4 | a). *J-V* curves of perovskite solar cells with 2-aminoethylphosphonic acid (PA), hypotaaurine (SA) and β -alanine additives (CA) or without additives under reverse scan direction. **b).** Incident photon-to-electron conversion efficiency (IPCE) curves of perovskite solar cells with or without additives. **c).** Stabilized power outputs (SPOs) of devices with or without additives. **d).** Transient photovoltage (TPV) curves of perovskite films with or without additives. **e).** Defect density calculated from the angular-frequency-dependent capacitance spectra with or without additives. **f).** Nyquist plots of perovskite solar cells with or without additives measured in the dark.

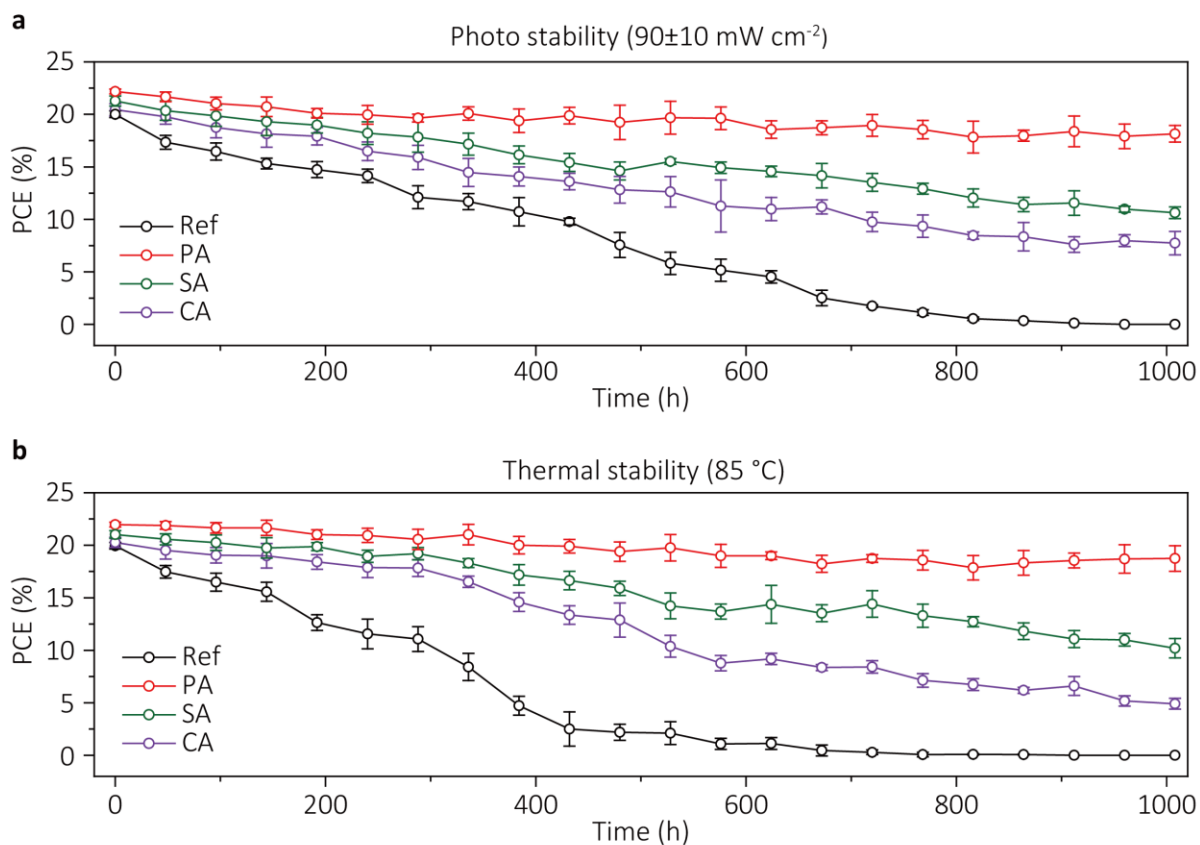


Figure 3.5 | a). Photo stability of perovskite solar cells with 2-aminoethylphosphonic acid (PA), hypotaurine (SA) and β -alanine additives (CA) or without additives. **b).** Thermal stability of perovskite solar cells with or without additives.

Table 3.1 | Photoluminescence lifetimes and defect density of the films with 2-aminoethylphosphonic acid (PA), hypotaurine (SA) and β -alanine additives (CA) or without additives. Corresponding photovoltaic parameters of champion perovskite solar cells with or without additives. The PCE values in the parenthesis are the stabilized power out (SPO) of the devices.

Devices	PL lifetime (μs)	defect density ($\times 10^{15} \text{cm}^{-3}$)		V_{oc} (V)	J_{sc} (mA cm^{-2})	FF (%)	PCE (%)
		electron	hole				
Reference	0.51	8.04	9.48	1.109	24.51	75.27	20.46 (20.01)
w/ PA	2.89	2.40	2.28	1.148	24.75	78.66	22.35 (22.17)
w/ SA	1.58	3.12	5.64	1.140	24.69	77.23	21.74 (21.27)
w/ CA	0.95	3.84	6.96	1.126	24.60	76.75	21.26 (20.44)

Chapter 4 Polymerization-assisted grain growth strategy

4.1 Introduction of the polymerization-assisted grain growth (PAGG) strategy

In the past decade, photovoltaic (PV) devices based on organometal halide perovskites have drawn significant attention since the pioneering work of the first all-solid-state perovskite solar cell in 2012.^{26-28, 73-74} Perovskite materials have properties that rival those of conventional semiconductors due to its long charge carrier diffusion length,^{28-30, 70} high absorption coefficients,^{31, 75-76} ease of fabrication,⁷⁷ and so on. Remarkable advances through compositional modulation, crystallization control and interface engineering have been made on improving the PV performance, promoting the PCE to a certified value of 25.2%.³³ Though the remarkable efficiency is comparable with traditional PV technology based on silicon (Si) or gallium arsenide (GaAs), the long-term stability against moisture, light, and heat lags behind and remains an obstacle towards commercialization.^{32, 34} Thus, extending the performance longevity is urgent for organometal halide perovskite solar cells at this stage.⁷⁸

Though device encapsulation and interface engineering have been proven to be effective to improve the stability of the perovskite devices externally,^{39, 79} improving the inherently unstable nature of perovskite materials should still be considered as the main approach to be investigated.⁸⁰⁻

⁸¹ Previous researches have demonstrated that the low formation energy of detrimental defects especially at the surface and grain boundaries is responsible for perovskite deterioration.^{70, 77, 82-84}

Therefore, it is expected that passivation efforts to mitigate and reduce these defects will be beneficial to improve the device longevity and efficiency simultaneously. Among all defect types, under-coordinated lead ions (Pb^{2+}) is shown to have relatively low formation energy and is one of the common origins of trap density.⁸⁵ From previous literature, defect passivation agents with lone-

pair electrons on nitrogen, oxygen or sulfur (such as pyridine, thiophene and urea) have been utilized to coordinate with these positively charged defects of perovskite.^{46, 86} However, these commonly used small molecules usually suffer from high volatility and disorderliness, which limits their practical applications in harsh environments.⁵⁰ As an alternative approach, the substitution of small molecules by polymers with similar functional groups is promising considering their low volatility. In previous works, there have been several attempts to apply polymeric additives to perovskite solar cells.^{50, 56, 87-94} For example, Zuo et al. demonstrated that the incorporation of poly (4-vinylpyridine) (PVP) additives into the perovskite film is an effective strategy to improve both the device efficiency and the stability.⁸² Bi et al. utilized poly(methyl methacrylate) (PMMA) as a template to control perovskite nucleation and crystal growth and fabricated solar cells with PCE up to 21.6%.⁹⁰ However, due to the relatively strong interaction between polymers and PbI_2 , precipitation in perovskite precursor solution has been seen,^{82, 89, 94} which could act as the initiating points for the crystallization of the perovskite. These will increase nuclei centers and decrease grain size consequentially, leading to the unsatisfied passivation effect. Herein, we introduce a polymerization-assisted grain growth (PAGG) strategy to obtain efficient perovskite solar cells with long-term stability. Starting from a sequentially deposited method, monomers added in the PbI_2 precursor first enables sufficient interaction between their carbonyl groups and the PbI_2 . During the following PbI_2 annealing process, an in-situ polymerization process is triggered, leaving the as-formed bulkier polymers adhered onto the grain boundaries with previously established interaction. When reacting with formamidinium iodide (FAI), there will be a higher energy barrier for forming the perovskite crystals due to the sufficient polymer- PbI_2 interaction, contributing to the enlarged crystal grains. In addition, carbonyl groups of polymers at the boundaries will target at the under-coordinated Pb^{2+} and efficiently reduce the trap

density, contributing to an increased PCE to 23.0%. Effective passivation, together with the hydrophobic nature of the polymer selected, will largely retard degradation rate, resulting in prominent improvements of stability.

4.2 Adduct formation and polymerization process

Dimethyl itaconate (DI) with C=C and C=O functional groups was chosen as the monomers due to its moderate volatility since monomers with low boiling points will rapidly volatilize before the polymerization process. The proper amount of DI was added into the PbI₂ precursor, along with 0.01 % molar ratio of azobisisobutyronitrile (AIBN) added as the initiator, which fast decomposes at high temperature (150°C, the annealing temperature of perovskite) and does not remain in the final perovskite films.⁹⁵⁻⁹⁶ Due to the lone electron pairs from the oxygen atoms of the ester groups, the DI monomers can act as a Lewis base to form an adduct with PbI₂ in the precursor, and the interaction is preserved after the spin-coating of the PbI₂ film (**Figure 4.1a**). During the PbI₂ annealing process, the DI monomer underwent polymerization where the C=C bonds of the monomers were cleaved and then subsequently relinked with adjacent monomers to form polymer, without sacrificing the interaction with Pb²⁺ by the C=O groups. Thus, the small DMSO molecules could be inserted into the PbI₂ interlayers, but the bulkier polymers were expelled to the grain boundaries (**Figure 4.1a**). When reacting with the organic molecule FAI, the energy barrier for the exchange of DMSO by FAI is relatively small compared to the exchange of the polymer, which is proved by the simulation in Figure 1b-d. The binding energies (defined as $E_{\text{molecule-PbI}_2} - E_{\text{molecule}} - E_{\text{PbI}_2}$) of DMSO-PbI₂, DI monomer-PbI₂ and DI dimer-PbI₂ are -0.83 eV, -1.05 eV, -1.61eV, respectively, showing an enlarged value for DI with PbI₂ compared to DMSO. For this reason, it is more difficult for DI polymer to be exchanged from the structure by FAI.

We firstly performed Fourier-transform infrared (FTIR) spectroscopy measurements to detect the polymerization process of the DI monomers before and after the annealing process. From Figure 2a, the pure DI monomers exhibit the characteristic peaks of the C=O (around 1737 cm^{-1}), C=C (around 1636 cm^{-1}), and =CH₂ (around 898 cm^{-1}) groups,⁹⁴ which all retain in the PbI₂ film with DI. After the annealing step of PbI₂, the C=C stretch and =CH₂ bend both vanish, indicating a complete polymerization transformation. Photographs of pure DI before and after polymerization are shown in **Figure 4.2b** and **2c** for further confirmation, where the polymerized product visually appeared as a transparent solid-state elastomer (**Figure 4.2c**), while the DI monomers before polymerization were in a liquid state (**Figure 4.2b**). After the formation of the PbI₂ film, FAI solution in IPA was spin-casted on the film to induce the intermolecular exchange to form the perovskite phase.⁹⁷ The resultant perovskite film also shows the same C=O stretch, demonstrating the preservation of the polymer after the two-step process (**Figure 4.2a**). This crystallization process is mainly related to the exchange of DMSO molecules with the FAI molecules (**Figure 4.1a**). Due to the large size of the polymerized DI and also the strong interaction with Pb²⁺, it will be much harder for the FAI to exchange with the polymer molecules. Therefore, nuclei formation and thus perovskite crystallization occurs in regions without polymer with priority, enabling the polymers to remain unreacted at the grain boundaries. This process was confirmed with the high-resolution transmission electron microscopy (HRTEM) images of PbI₂ films after the polymerization and the as-converted perovskite films (**Figure 4.2d,e**, respectively). An amorphous area is clearly distinguishable between the contiguous grains, indicating the gathering of polymer molecules between them, which is consistent with the previous findings with polymer additives.⁵⁰

⁹⁴ The Fast Fourier Transform (FFT) images and lattice distances for PbI₂ and perovskite grains are also shown, demonstrating a plane distance of 3.7 \AA and 3.2 \AA . They match well with the (100)

reflection of the hexagonal PbI_2 phase and the (001) reflection of the cubic perovskite phase, respectively.^{41,98} These immobile polymers are suitable to serve as the passivation agent along the grain boundaries by interacting with the under-coordinated Pb^{2+} without introducing more defects inside the grain interior, which is probable in some other cases for small additives.

4.3 Intermolecular exchanging grain growth and film properties

We further tracked the perovskite grain growth process in-situ using confocal laser scanning fluorescence microscopy (CLSM) measurement, starting from the pure PbI_2 or PbI_2 -DI (after polymerization) films (denoted as green) to the final perovskite films (denoted as red) (**Figure 4.3b,c**). After the drop-casting of the diluted FAI/IPA solution on the as-prepared PbI_2 films, a reduced amount of nucleation sites and a retarded crystallization process were observed for our PAGG process compared to the control one, which could be explained by the increased energy barrier for the substitution of the polymer by the FAI molecules (Figure 3a). As a result, larger grains and reduced grain boundaries were obtained using the PAGG strategy, confirmed by the scanning electron microscopy (SEM) images shown in Figure 3d and 3e, respectively. The average grain size of the control sample is about $0.75 \mu\text{m}$ (Figure 3d) while the target one is about $1.25 \mu\text{m}$ (**Figure 4.3e**), as corroborated by the AFM images shown in the Supporting Information (**Figure A4.1**). The cross-sectional SEM image of the target sample in Figure 3f further confirms the large size distribution, showing no grain boundaries along the charge transport direction perpendicular to the substrates. The enlarged grain sizes, together with the long-range ordering with the polymers, contributed to the better crystallinity, as proved by the X-ray diffraction (XRD) studies. The intensity of the (001) peak located at 13.9° is enhanced by 1.34 fold, indicating the improved crystallinity and orientation. The DI polymers with the $\text{C}=\text{O}$ groups effectively passivated the

defects accumulated at the grain boundary regions, resulting in the better optoelectrical properties, which were investigated by photoluminescence (PL) spectroscopy. The steady-state PL shows a 1.72-fold enhancement in intensity without a noticeable shift of the peak positions (insert of **Figure 4.3h**). The time-resolved PL (TRPL) decay of the films was also measured to better compare the trap density of the films (**Figure 4.3h**). In the figure, circles indicate measured data while solid lines indicate the fitted curves with a bi-exponential decay model.⁵⁰ In this model, the faster decay components are attributed to defect-assisted non-radiative recombination, while the slower decay components are assigned to bimolecular radiative recombination in the bulk.⁵⁰ The fitted parameters of the average PL lifetime is summarized in Fig. 3h. The film fabricated with PAGG process demonstrated an increased fast-decay lifetime τ_1 of 130 ns, compared to that of the control perovskite film of 67 ns. Furthermore, the slow-decay lifetime τ_2 was also enhanced, from 161 ns (control film) to 370 ns (PAGG), exhibiting a longer charge carrier lifetime within the bulk crystals. The increased lifetime suggests a lower defect density of the film which mainly originates from two factors, reduced grain boundaries due to the enlarged grain sizes and efficient passivation effect by the polymer.

4.4 Improved photovoltaic performance and stability using the PAGG strategy

The photovoltaic performance of the perovskite solar cells with a device architecture of ITO/SnO₂/perovskite/spiro-OMeTAD/Ag (**Figure 4.3f**) with and without the PAGG process are compared (**Figure 4.4a**). With the sequentially deposited method, the control device had a short circuit current density (J_{sc}) of 24.6 mA cm⁻², an open-circuit voltage (V_{oc}) of 1.096 V, and a fill factor (FF) of 77.5%, which resulted in a power conversion efficiency (PCE) of 20.9% at reverse scan. In contrast, the addition of 1.0 mol% of the additives (**Figure A4.2**) increased all the

parameters to achieve a J_{sc} of 24.9 mA cm^{-2} , a V_{oc} of 1.145 V , and an FF of 80.6% . These led to an enhanced power conversion efficiency (PCE) to 23.0% at reverse scan. Detailed photovoltaic parameters are summarized in Table 1. The increased V_{oc} and FF are attributed to a decreased defect density by the polymer that reduced the non-radiative recombination originating from the defects along the grain boundaries. The slight increase of J_{sc} value is due to the better charge extraction in the target devices, as indicated by the higher EQE values shown in Figure 4a. The two IPCE curves display similar trends, where the integrated current densities from the IPCE spectrum are 24.4 mA/cm^2 and 24.0 mA/cm^2 , matching with the J_{sc} values obtained from the I-V scans. We then measured the transient photovoltage (TPV) decay under the open-circuit condition to characterize the charge-recombination lifetime of the control and target devices (**Figure 4.4c**). The charge carrier lifetime of the target device is substantially longer than that of the control, consistent with the reduced non-radiative recombination from the PL results (**Figure 4.3h**). We also measured the transient photocurrent (TPC) decay under the short-circuit condition to study the charge transfer process (**Figure 4.4d**). The slightly reduced lifetime indicates a more efficient charge extraction and transfer process of our devices employing PAGG strategy.

To verify the passivation function of the resultant polymer to retard the decomposition process of the perovskite films, we used XRD to investigate the stability of the films under different harsh environments. As seen from Figure S3, after 250-hour storage in a 70% humidity environment, the control films obviously decomposed compared to that with PAGG process. The perovskite (001) peak to PbI_2 (100) peak intensity ratio was enhanced from 0.063 for the control film to 0.96 for the PAGG target film. This significant difference clearly shows the stabilization effect from the PAGG process attributed to the hydrophobic nature of the formed polymer. The thermal stability was also improved, confirmed by comparing the XRD spectra of the films heated at $85 \text{ }^\circ\text{C}$ in a

nitrogen atmosphere for 350 hours (**Figure A4.4**). These various stability tests under different harsh environments demonstrate improved stability as a result of the polymerization-assisted crystallization. To quantitatively confirm the stability enhancement of devices, photostability and shelf stability of control and PAGG treated solar cells were both measured. To test the photostability of the devices, we encapsulated the devices and put them under 1-sun illumination with open-circuit condition. During the illumination, 35-40% relative humidity and temperature of 40 °C were maintained. As shown in Figure 4e, the average PCE of the control device degraded rapidly and retained only 14.1 % of its initial value. In contrast, the device treated with PAGG process retained 85.7 % of its initial PCE after 504-hour continuous illumination. In addition, the shelf stability of devices with PAGG process was also enhanced, maintaining 91.8% of its initial value after 2208-hour storage in ambient condition without encapsulation, while only 32.6% remained in control devices. This significant difference further demonstrates the much-improved environmental stability of our devices with PAGG strategy.

4.5 Conclusions

In summary, we introduce a polymerization-assisted method to obtain perovskite solar cells improved performance and stability. By incorporating the DI monomers into the PbI_2 solution and initiating the polymerization process during the annealing step, we successfully maintained the merits of the polymer additive, and at the same time ensured sufficient adduct formation between the additive and the precursor. By utilizing the intermolecular exchange process of the two-step method, we proved that the polymer gathered at the perovskite grain boundaries, which effectively reduced the possible defects by the carbonyl groups. The enlarged grains with the lower defect density improved the PCE to 23.0 % of our champion target device and achieved significantly

improved photo and shelf stability. This work provides valuable insights into improving both performance and operational longevity of perovskite solar cells.

References

- [1] H.-S. Kim, C.-R. Lee, J.-H. Im, K.-B. Lee, T. Moehl, A. Marchioro, S.-J. Moon, R. Humphry-Baker, J.-H. Yum, J. E. Moser, *Scientific reports* **2012**, 2, 591.
- [2] M. M. Lee, J. Teuscher, T. Miyasaka, T. N. Murakami, H. J. Snaith, *Science* **2012**, 338, 643.
- [3] W. S. Yang, B.-W. Park, E. H. Jung, N. J. Jeon, Y. C. Kim, D. U. Lee, S. S. Shin, J. Seo, E. K. Kim, J. H. Noh, *Science* **2017**, 356, 1376.
- [4] S. D. Stranks, G. E. Eperon, G. Grancini, C. Menelaou, M. J. Alcocer, T. Leijtens, L. M. Herz, A. Petrozza, H. J. Snaith, *Science* **2013**, 342, 341.
- [5] N. Ahn, D.-Y. Son, I.-H. Jang, S. M. Kang, M. Choi, N.-G. Park, *Journal of the American Chemical Society* **2015**, 137, 8696.
- [6] G. Xing, N. Mathews, S. Sun, S. S. Lim, Y. M. Lam, M. Grätzel, S. Mhaisalkar, T. C. Sum, *Science* **2013**, 342, 344.
- [7] D. Shi, V. Adinolfi, R. Comin, M. Yuan, E. Alarousu, A. Buin, Y. Chen, S. Hoogland, A. Rothenberger, K. Katsiev, *Science* **2015**, 347, 519.
- [8] Q. Dong, Y. Fang, Y. Shao, P. Mulligan, J. Qiu, L. Cao, J. Huang, *Science* **2015**, 347, 967.
- [9] Q. Lin, A. Armin, R. C. R. Nagiri, P. L. Burn, P. Meredith, *Nature Photonics* **2015**, 9, 106.
- [10] N.-G. Park, *Materials today* **2015**, 18, 65.
- [11] Z. Yang, Y. Deng, X. Zhang, S. Wang, H. Chen, S. Yang, J. Khurgin, N. X. Fang, X. Zhang, R. Ma, *Advanced Materials* **2018**, 30, 1704333.

- [12] J.-W. Lee, H.-S. Kim, N.-G. Park, *Accounts of chemical research* **2016**, *49*, 311.
- [13] <https://www.nrel.gov/pv/assets/pdfs/best-research-cell-efficiencies.20190802.pdf>.
- [14] Y. Yang, J. You, *Nature News* **2017**, *544*, 155.
- [15] H. S. Jung, N. G. Park, *small* **2015**, *11*, 10.
- [16] T. Leijtens, G. E. Eperon, N. K. Noel, S. N. Habisreutinger, A. Petrozza, H. J. Snaith, *Advanced Energy Materials* **2015**, *5*, 1500963.
- [17] Y. I. Lee, N. J. Jeon, B. J. Kim, H. Shim, T. Y. Yang, S. I. Seok, J. Seo, S. G. Im, *Advanced Energy Materials* **2018**, *8*, 1701928.
- [18] Y. Lv, P. Xu, G. Ren, F. Chen, H. Nan, R. Liu, D. Wang, X. Tan, X. Liu, H. Zhang, *ACS applied materials & interfaces* **2018**, *10*, 23928.
- [19] D. W. de Quilettes, S. M. Vorpahl, S. D. Stranks, H. Nagaoka, G. E. Eperon, M. E. Ziffer, H. J. Snaith, D. S. Ginger, *Science* **2015**, *348*, 683.
- [20] S. Y. Leblebici, L. Leppert, Y. Li, S. E. Reyes-Lillo, S. Wickenburg, E. Wong, J. Lee, M. Melli, D. Ziegler, D. K. Angell, *Nature Energy* **2016**, *1*, 16093.
- [21] Y. Wang, T. Wu, J. Barbaud, W. Kong, D. Cui, H. Chen, X. Yang, L. Han, *Science* **2019**, *365*, 687.
- [22] Y. Wu, A. Islam, X. Yang, C. Qin, J. Liu, K. Zhang, W. Peng, L. Han, *Energy & Environmental Science* **2014**, *7*, 2934.
- [23] L. Zuo, H. Guo, D. W. deQuilettes, S. Jariwala, N. De Marco, S. Dong, R. DeBlock, D. S. Ginger, B. Dunn, M. Wang, *Science advances* **2017**, *3*, e1700106.
- [24] Y. Kutes, Y. Zhou, J. L. Bosse, J. Steffes, N. P. Padture, B. D. Huey, *Nano letters* **2016**, *16*, 3434.

- [25] J. Xue, R. Wang, K.-L. Wang, Z.-K. Wang, I. Yavuz, Y. Wang, Y. Yang, X. Gao, T. Huang, S. Nuryyeva, *Journal of the American Chemical Society* **2019**, *141*, 13948.
- [26] X. Zheng, B. Chen, J. Dai, Y. Fang, Y. Bai, Y. Lin, H. Wei, X. C. Zeng, J. Huang, *Nature Energy* **2017**, *2*, 17102.
- [27] N. K. Noel, A. Abate, S. D. Stranks, E. S. Parrott, V. M. Burlakov, A. Goriely, H. J. Snaith, *ACS nano* **2014**, *8*, 9815.
- [28] R. Wang, J. Xue, L. Meng, J.-W. Lee, Z. Zhao, P. Sun, L. Cai, T. Huang, Z. Wang, Z.-K. Wang, *Joule* **2019**, *3*, 1464.
- [29] T.-H. Han, J.-W. Lee, C. Choi, S. Tan, C. Lee, Y. Zhao, Z. Dai, N. De Marco, S.-J. Lee, S.-H. Bae, *Nature communications* **2019**, *10*, 520.
- [30] J. Xu, A. Buin, A. H. Ip, W. Li, O. Voznyy, R. Comin, M. Yuan, S. Jeon, Z. Ning, J. J. McDowell, *Nature communications* **2015**, *6*, 7081.
- [31] C.-Y. Chang, C.-Y. Chu, Y.-C. Huang, C.-W. Huang, S.-Y. Chang, C.-A. Chen, C.-Y. Chao, W.-F. Su, *ACS applied materials & interfaces* **2015**, *7*, 4955.
- [32] Y. Zhao, J. Wei, H. Li, Y. Yan, W. Zhou, D. Yu, Q. Zhao, *Nature communications* **2016**, *7*, 10228.
- [33] D. Bi, C. Yi, J. Luo, J.-D. Décoppet, F. Zhang, S. M. Zakeeruddin, X. Li, A. Hagfeldt, M. Grätzel, *Nature Energy* **2016**, *1*, 16142.
- [34] J. Jiang, Q. Wang, Z. Jin, X. Zhang, J. Lei, H. Bin, Z. G. Zhang, Y. Li, S. Liu, *Advanced Energy Materials* **2018**, *8*, 1701757.
- [35] Y. Zong, Y. Zhou, Y. Zhang, Z. Li, L. Zhang, M.-G. Ju, M. Chen, S. Pang, X. C. Zeng, N. P. Padture, *Chem* **2018**, *4*, 1404.

- [36] M. Kim, S. G. Motti, R. Sorrentino, A. Petrozza, *Energy & Environmental Science* **2018**, *11*, 2609.
- [37] X. Li, M. I. Dar, C. Yi, J. Luo, M. Tschumi, S. M. Zakeeruddin, M. K. Nazeeruddin, H. Han, M. Grätzel, *Nature chemistry* **2015**, *7*, 703.
- [38] X. Li, W. Zhang, Y.-C. Wang, W. Zhang, H.-Q. Wang, J. Fang, *Nature communications* **2018**, *9*, 3806.
- [39] S. Guo, W. Wan, C. Chen, W. Chen, *Journal of thermal analysis and calorimetry* **2013**, *113*, 1169.
- [40] X.-R. Li, X.-L. Wang, H. Koseki, *Journal of hazardous materials* **2008**, *159*, 13.
- [41] W. S. Yang, J. H. Noh, N. J. Jeon, Y. C. Kim, S. Ryu, J. Seo, S. I. Seok, *Science* **2015**, *348*, 1234.
- [42] M. Zhong, S. Zhang, L. Huang, J. You, Z. Wei, X. Liu, J. Li, *Nanoscale* **2017**, *9*, 3736.
- [43] J.-W. Lee, Z. Dai, T.-H. Han, C. Choi, S.-Y. Chang, S.-J. Lee, N. De Marco, H. Zhao, P. Sun, Y. Huang, *Nature communications* **2018**, *9*, 3021.

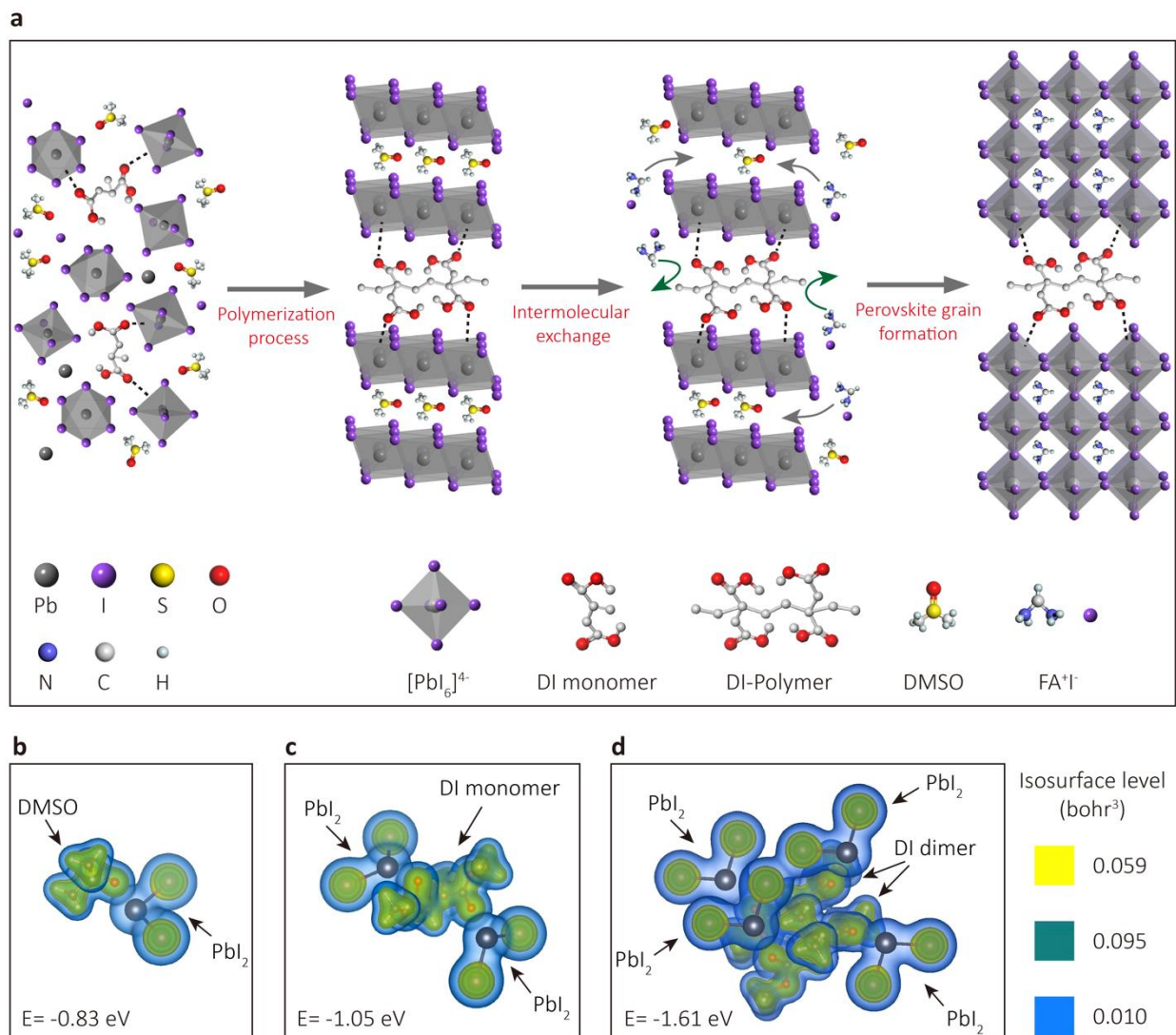


Figure 4.1 | Illustration of polymerization-assisted grain growth (PAGG) process and the binding energies between additives and PbI₂ molecules. (a) Schematic illustration of the polymerization-assisted grain growth (PAGG) process. **(b-d)** computational study of most favorable molecular configurations and binding energies between **(b)** the PbI₂ molecule and DMSO, **(c)** the PbI₂ molecules and DI monomer, **(d)** the PbI₂ molecules and DI dimer.

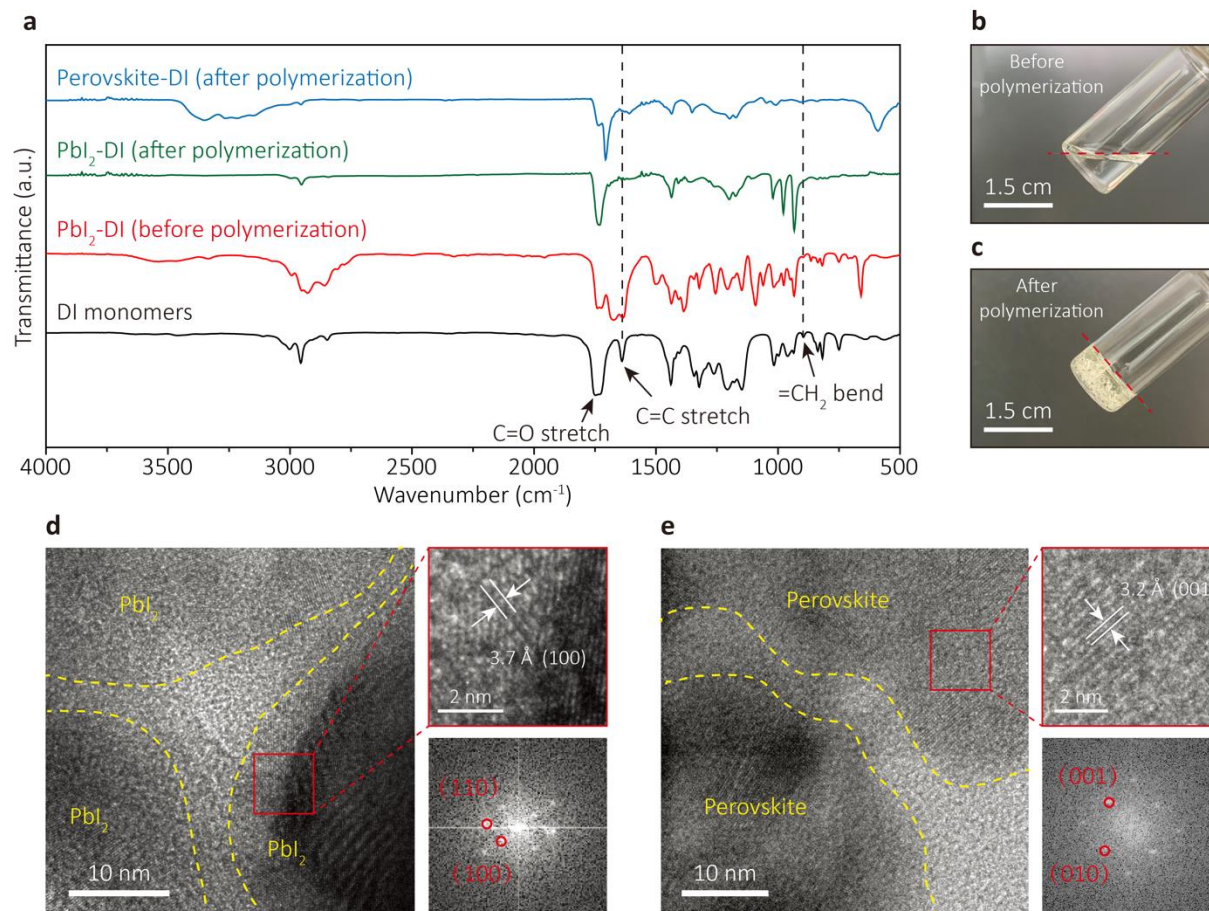


Figure 4.2 | Confirmation of polymerization process. (a) Fourier transform infrared spectra (FTIR) of the DI monomers, PbI₂-DI film before and after the polymerization process, and perovskite film after the intermolecular exchanging process. (b,c) Photographs of the pure DI monomers (b) before and (c) after the polymerization process. (d,e) High-resolution transmission electron microscopy (HRTEM) images and Fast Fourier transform (FFT) analysis of the grain areas of the (d) PbI₂-DI sample after the polymerization process, and (e) perovskite sample after the intermolecular exchanging process.

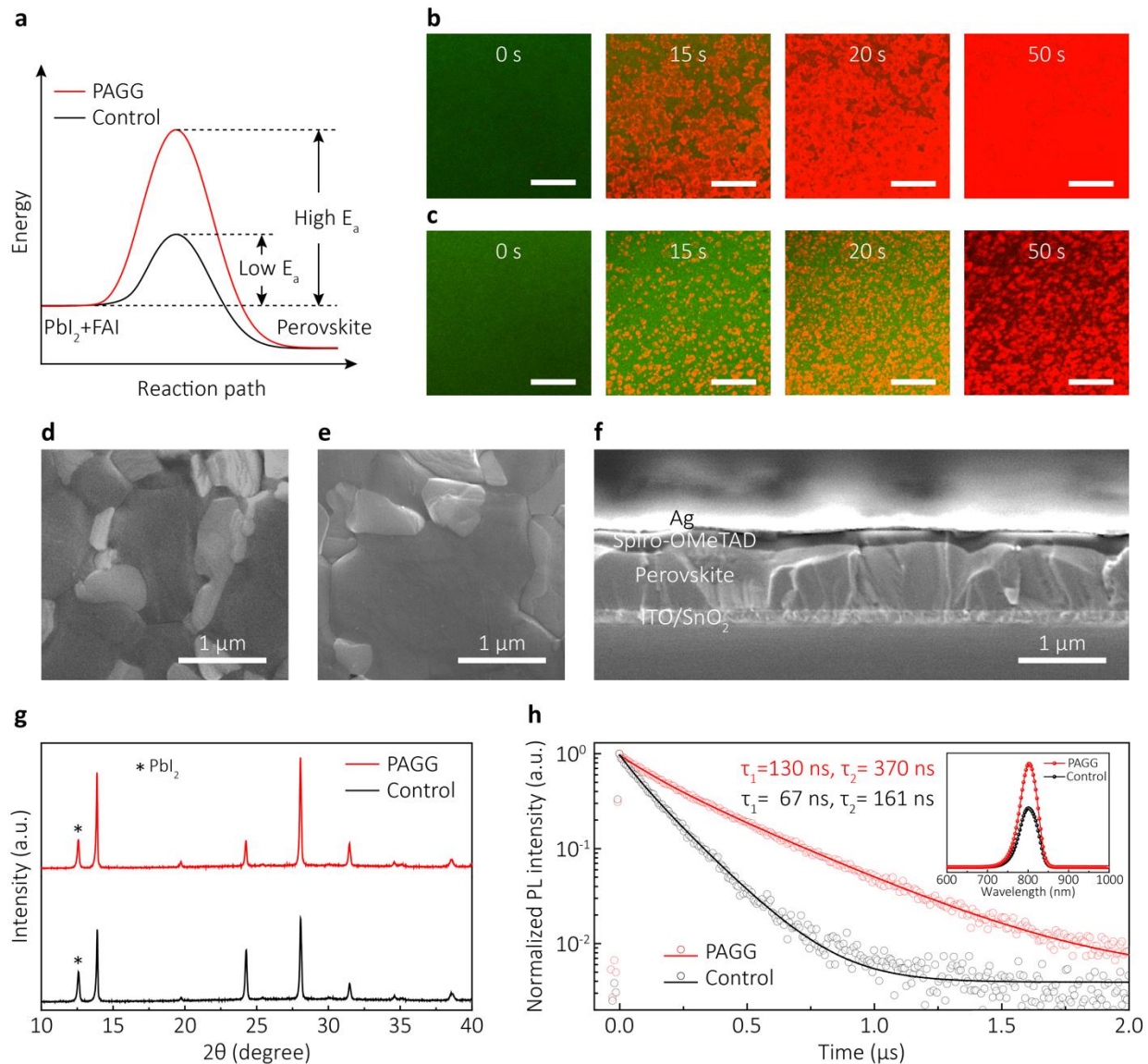


Figure 4.3 | Intermolecular exchanging grain growth and film properties. (a) Schematic diagrams of perovskite crystallization kinetics of PbI₂ films without (black) and with (red) PAGG process. (b,c) Confocal laser scanning fluorescence microscopy (CLSFM) images of PbI₂ films (b) without and (c) with PAGG process as a function of time (0s, 15s, 20s, 50s) of intermolecular exchanging process. The PbI₂ regions are shown in green while the perovskite phase is shown in red in the images. Scale bars indicate 10 μm. (d,e) Top-view scanning electron microscopy (SEM) images of perovskite film (d) without and (e) with PAGG process. (f) Cross-sectional SEM image

of the solar cell device with perovskite film with PAGG process. **(g)** X-ray diffraction spectra (XRD) of the perovskite films without (black) and with (red) PAGG process. **(h)** Time-resolved photoluminescence (PL) spectra (Inset: steady-state PL spectra) of the perovskite films without (black) and with (red) PAGG process.

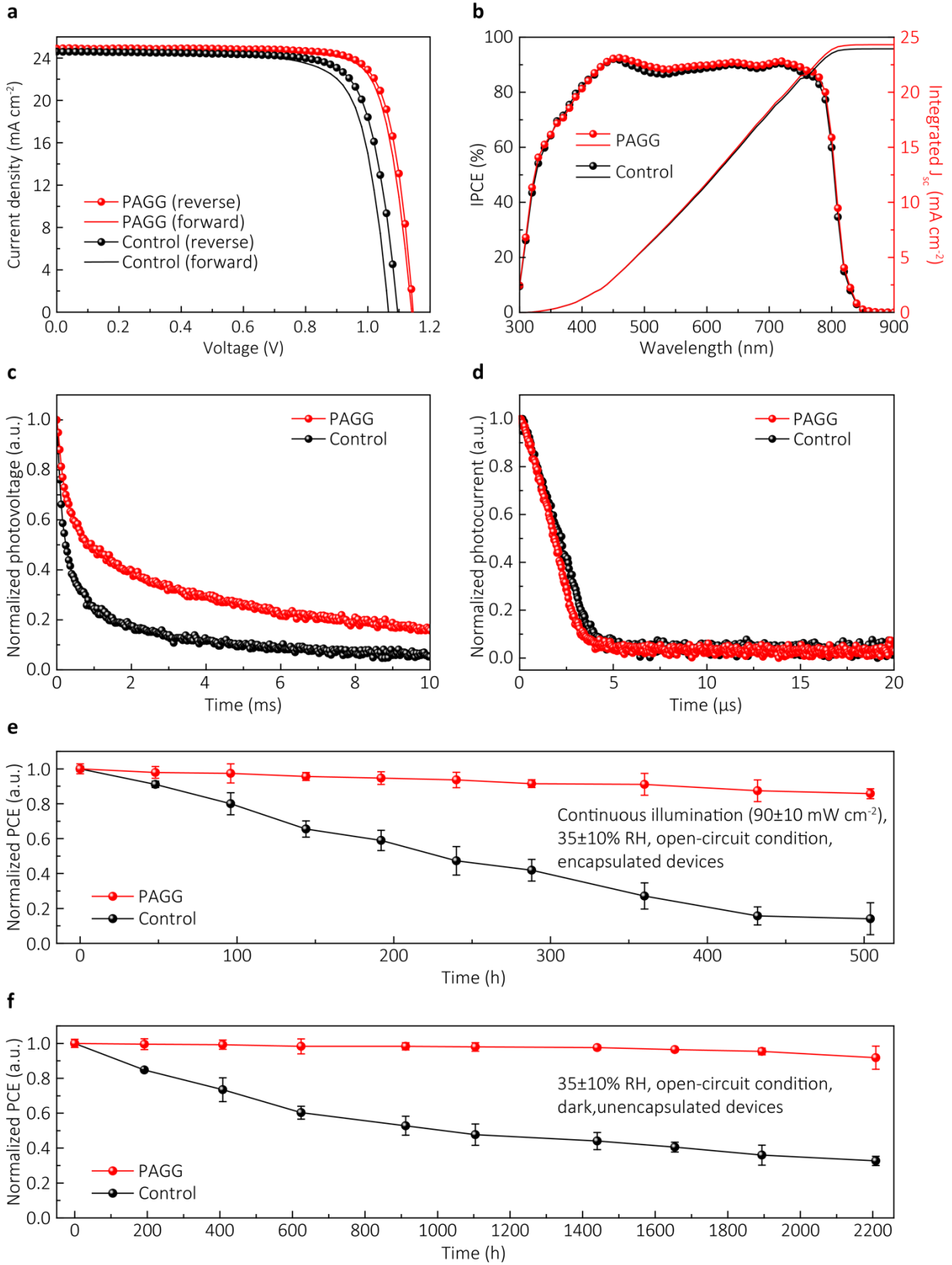


Figure 4.4 | Improved photovoltaic performance and stability using the PAGG strategy. (a) Current density–voltage (J–V) curves of perovskite solar cells without or with PAGG process. **(b)** IPCE curves of perovskite solar cells without (black) and with (red) PAGG process. **(c)** Transient photovoltage (TPV) decay of the perovskite solar cells without (black) and with (red) PAGG process. **(d)** Transient photocurrent (TPC) decay of the perovskite solar cells without (black) and with (red) PAGG process. **(e)** Evolution of the measured power conversion efficiencies (PCEs) of encapsulated perovskite solar cells without (black) and with (red) PAGG process under continuous illumination at open-circuit condition. **(f)** Evolution of the measured power conversion efficiencies (PCEs) of unencapsulated perovskite solar cells without (black) and with (red) PAGG process exposed to ambient atmosphere at open-circuit and dark condition.

Table 4.1 | Detailed photovoltaic parameters of champion perovskite solar cells with and without PAGG

Devices	Scan directions	V _{oc} (V)	J _{sc} (mA cm ⁻²)	FF (%)	PCE (%)
Control	Reverse	1.096	24.6	77.5	20.9
	Forward	1.065	24.6	75.8	19.9
PAGG	Reverse	1.145	24.9	80.8	23.0
	Forward	1.142	24.9	79.7	22.6

Chapter 5 Hermetic Seal for Perovskite Solar Cells: An Improved Plasma Enhanced Atomic Layer Deposition Encapsulation

5.1 Introduction of plasma enhanced atomic layer deposition encapsulation

Metallic halide perovskite materials have drawn great attention over the last decades for its high defect tolerance, long charge carrier diffusion length and high absorption coefficient⁹⁹. The perovskite solar cell research performed so far allowed a considerable enhancement in photoelectric conversion efficiency (PCE) of perovskite solar cells from 9.7%¹⁰⁰ to 25.2%.¹⁰¹ This achievement has promoted perovskite solar cell as a promising candidate to compete with the conventional silicon based solar cells. However, unlike to the breakthrough of the photovoltaic performance, the inferior stability and toxicity remain the main challenges in the commercialization of perovskite solar cell.¹⁰² Tremendous work has been done to improve the long-term stability of perovskite solar cells including interface engineering, compositional change and grain boundary passivation.¹⁰³⁻¹⁰⁵ However, these strategies did not change the fact that organometal halide materials are easily degraded by moisture, and the fabricated solar cells are still far from being able to withstand the practical application. Hence, efficient encapsulation of the device is necessary to prevent the perovskite solar cell devices from the moisture and elongate its operational duration in the outside environment.¹⁰⁶

Epoxy bonded cover is the most common encapsulation approach to ensure the long-term stability of organic electronics.¹⁰⁷ However, the damage caused by the UV radiation and heat released during the photocuring reaction will undermine the performance of the devices.¹⁰⁸⁻¹⁰⁹ Also, side penetration through the epoxy between the cover and substrate is also not negligible.¹¹⁰ For this reason, the epoxy-free thin film encapsulation, including atomic layer deposition (ALD),¹¹¹

magnetron sputtering,¹¹² and chemical vapor deposition,¹¹³ are intensively explored in organic light-emitting devices (OLEDs)¹¹⁴ and organic solar cells (OSCs).¹¹⁵ However, compared to OLEDs and OSCs, perovskite solar cells are more susceptible to damage. The high temperature (i.e. 80 °C) or large-power plasma required for an efficient thin film encapsulation for OLEDs are usually associated with major degradation of perovskite solar cells.¹¹⁶⁻¹¹⁷ Therefore, an effective encapsulation with moderate conditions are highly demanded for the application of perovskite solar cells.¹¹⁸ Recently, Lee et al. used thermal ALD to grow Al₂O₃ layer on the perovskite solar cells at 60 °C.¹¹⁹ The alternating lamellae of Al₂O₃ and organic components enhanced the long-term stability of perovskite solar cells, which maintained 90% of their initial efficiency after 300 hours under accelerated condition. However, as discussed in his article, the water vapor transmission rate (WVTR) of thermal ALD Al₂O₃ grown at 60 °C was a few hundred times higher than that grown at 90 °C, which indicated a great sacrifice in barrier properties. Similarly, Lv et al. reported an efficiency of 93% maintained for 1000 hours in ambient environment by using ALD Al₂O₃ encapsulation layers and TiO₂.¹²⁰ Impressively, these solar cell devices survived in deionized water for two hours. This work nicely emphasized the practical perspectives of ALD encapsulation strategy. However, the Al₂O₃ and TiO₂ were also grown by thermal ALD with H₂O as precursor and thus, the film quality still needed major improvements. Hence, developing an appropriate method to efficiently prepare thin film encapsulation with extremely low damaging perovskite solar cells during the encapsulation process is still a challenge.

Herein, we report a low damage alucone from ethylene glycol as a buffer layer to protect the devices from plasma-enhanced atomic layer deposition (PEALD). The buffer layer is obtained by molecular layer deposition (MLD) and followed PEALD was performed at 50 °C to prevent our metal halide perovskite solar cells from degradation. Methyl groups remained in the alucone

efficiently protected the perovskite solar cells against O₂ plasma in the PEALD process. To the best of our knowledge, this is the first report on a high water-preventing encapsulation film deposited on perovskite solar cells by PEALD. This MLD/PEALD approach leads to the lowest reported WVTR of $1.3 \times 10^{-5} \text{ g}\cdot\text{m}^{-2}\cdot\text{day}^{-1}$ under 80% relative humidity at 30 °C. The encapsulated standard MAPbI₃ perovskite solar cells maintained 96% of initial efficiency for over 2000 hours. Therefore, it can be stated that our research proposes a realistic solution to address the challenges raised by the long-term stability of perovskite solar cells when used in the outside environment.

5.2. Experimental methods

Materials

One mmol of CH₃NH₃I (Dyesol) and PbI₂ (99.999%, TCI) were dissolved in N,N-dimethylformamide (DMF, anhydrous, 99.8%, Sigma-Aldrich) to form the perovskite precursor solution, and using dimethyl sulfoxide (DMSO anhydrous, 99.7%, Sigma-Aldrich) as additive. SnCl₂·2H₂O (98%) for ETL was purchased from Sigma Aldrich. For hole transporting layer (HTL), spiro-MeOTAD was purchased from 1-Material, 4-tert-butylpyridine (96%) and Li-TFSI (99.95%) were purchased from Sigma Adrich. The solvents, acetonitrile and chlorobenzene (anhydrous, 99.8%), were also purchased from Sigma Aldrich. All ALD materials were purchased from Sigma-Aldrich and used as received, unless stated otherwise.

ALD procedure and preparation of perovskite solar cells

For the reaction processes, the precursor was injected into the chamber under high-purity Ar (99.999%) as carrier gas (100 sccm). The pressure in the chamber was set at 0.25 Torr.

Trimethyl aluminum (TMA, 99.9999%) and deionized water (H₂O, 99.99%) were used as precursors of the thermal ALD Al₂O₃. The TMA and H₂O were maintained at room-temperature. The optimal conditions for the growth of H₂O-based Al₂O₃ were as follows: TMA dose of 0.04 s, TMA purge of 80 s, H₂O dose of 0.1 s and H₂O purge of 120 s.

TMA and O₂ plasma were the precursors of the plasma enhanced ALD Al₂O₃. The TMA was maintained at room-temperature and O₂ plasma was generated using 15 sccm O₂ (99.999%) with a radio frequency power of 100 W. The optimal conditions for the growth of PEALD Al₂O₃ were as follows: TMA dose of 0.04 s, TMA purge of 80 s, O₂ plasma dose of 10 s and O₂ plasma purge of 120 s.

Trimethyl aluminum (TMA, 99.9999%) and ethylene glycol (EG, 99.8%) were used as precursors of MLD alucone. The TMA was maintained at room-temperature and EG was heated to 80 °C. The optimal conditions for the growth of alucone were as follows: TMA dose of 0.04 s, TMA purge of 80 s, EG dose of 4 s and EG purge of 120 s.

The substrates of the solar cell devices are made of 500 nm indium-tin-oxide (ITO) coated on 1 mm glass. The substrates are cleaned by sequential ultra-sonication in detergent, acetone and isopropanol for 30 min each. Cleaned ITO glass was treated by ultraviolet ozone for 25 min before the electron transport layer (ETL) deposition. ETL are formed by spin-coating 30 mM SnCl₂·2H₂O (98%) dissolved in ethanol (anhydrous, Sigma Aldrich) and then sequentially annealed at 150 and 180 °C, for 30 and 60 min, respectively, to obtain the SnO₂ film. The active layers of perovskite solar cells are fabricated by using a perovskite precursor solution made of 1 mmol of CH₃NH₃I, PbI₂ and DMSO dissolved in 500 mg of DMF. After 15 min UVO treatment of the substrates with ETL, the perovskite solution was spin coated on Glass/ITO/SnO₂. Diethyl ether (DE, 0.3 mL) was dropped during spin coating (after 10 s) of the perovskite

solution. The transparent adduct film was annealed at 65 °C for 1 min, and then at 100 °C for 30 min. The hole transport layer (HTL) of the solar cell devices are formed by spin-coating spiro-OMeTAD solution onto the perovskite film. Spiro-OMeTAD solution was prepared with the following composition: 85.8 mg of spiro-MeOTAD, 33.8 μL of 4-tert-butylpyridine (96%), and 19.3 μL of Li-TFSI (99.95%, 520 mg mL^{-1} in acetonitrile) in 1 mL of chlorobenzene (anhydrous, 99.8%). For the top electrode, 100 nm-thick Ag was thermally deposited at an evaporation rate of 0.5 A s^{-1} .

Films Characterization

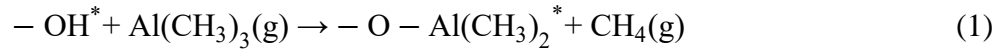
In-situ QMS and in-situ QCM (SQM160, INFICION) measurements were simultaneously implemented during film growth. atomic force microscopy (AFM, using ICON-PT, Bruker; contact mode) and scanning electron microscopy (SEM, JSM-7500F, JEOL; accelerating voltage of 5 kV) were used to analyze surface topography. The phase and crystallization of the films were determined by X-ray diffraction (XRD, model D/max 2400). Variable-angle spectroscopic ellipsometry (J.A. Woolam) and transmission electron microscopy (TEM) were used to determine film thickness. Alucone were deposited on KBr tablets for 300 cycles then subjected to Fourier transform infrared spectroscopy (FTIR, Perkin-Elmer Spectrum One) analysis to determine the chemical structure based on the bond vibration. The water vapor transmittances of encapsulation films were measured using Ca corrosion testing. The calcium was evaporated to a 1 cm \times 1 cm region with a thickness of 200 nm. The electrical conductance ($1/R$) of the Ca were measured using an Agilent B2902A Precision Source (Agilent Technologies, Inc., Santa Clara, CA, USA) under 80% relative humidity at 30 °C.

Device characterization

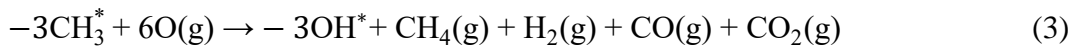
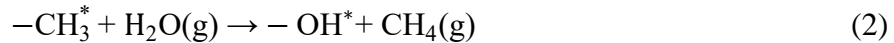
The current-voltage (J–V) characteristics of the perovskite devices were recorded under ambient temperature and air conditions with a digital source meter (Keithley model 2400, USA). A 450 W xenon lamp (Oriol, USA) was used as the light source for photovoltaic (J–V) measurements. The spectral output of the lamp was filtered using a Schott K113 Tempax sunlight filter (Präzisions Glas & Optik GmbH, Germany) to reduce the mismatch between the simulated and actual solar spectrum to less than 2%. The photo-active area of 0.1 cm² was defined using a dark-colored metal mask.

5.3 Damage to perovskite solar cells during encapsulation process

In ALD processes, the reactions between the functional groups of the substrate and precursors are decisive for the quality of the grown film.^{111, 113} In our case, as shown in Fig. 5.1, we injected trimethylaluminum (TMA), which reacted with the hydroxyl groups on the substrate surface to generate an intermediate product (reaction (1)).¹²¹



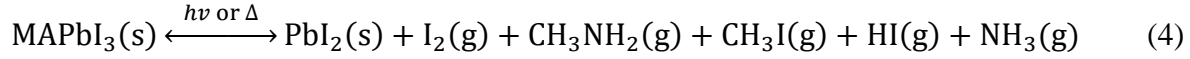
The resulted methyl groups became the new functional groups and subsequently reacted with the injected oxidant precursors, i.e. water (reaction (2)) and O₂ plasma (reaction (3)):¹²²



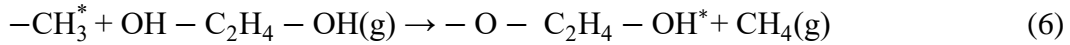
For the reaction (2), thermal energy from the substrate is the main source of activation energy due to the low activity of water.^{113, 123} Therefore, at a temperature below 100 °C, the thermal energy is not enough and the deposited film is far from being ideal.¹¹⁹ As shown in Fig. A5.1, the WVTR increase from 1.1 × 10⁻⁴ g·m⁻²·day⁻¹ at 110 °C to 2.2 × 10⁻³ g·m⁻²·day⁻¹ at 50 °C is an evidence of

a large decrease in water protection ability. On the other hand, it is acknowledged that a high temperature (i.e. above 70 °C) dramatically accelerated the decomposition of the metal halide perovskite structure and the degradation of spiro-MeOTAD.^{102, 117} This behavior is the main limitation of solar cell devices undergoing an ALD process. For the standard MAPbI₃ perovskite solar cells used herein, when the deposition of thin film encapsulation was performed at a temperature above 70 °C, the performance degradation became obvious in a short time (Fig. 5.1b). To overcome this shortcoming, we selected O₂ plasma with high activity as oxidant precursor. As the experimental results displayed in Fig. A5.2, a temperature decreased from 90 to 50 °C did not influence the WVTRs of PEALD Al₂O₃ films, which kept at the same value of $\sim 5 \times 10^{-5}$ g·m⁻²·day⁻¹. Hence, it is evident that the utilization of PEALD is an efficient and promising strategy for low-temperature encapsulation of organo-metallic halide perovskite solar cells. However, for the perovskite solar cells, O₂ plasma is harmful for the whole device structure. The decrease in the XRD intensity of the (110) and (220)¹²⁴ crystal planes of the perovskite layers after direct O₂ plasma treatment (Fig. 5.1c) indicated a degradation of the perovskite structure. This degradation was confirmed by the scanning electron microscope (SEM) images of the plasma-treated perovskite films (Fig. A5.3). When exposed to O₂ plasma, the MAPbI₃ decomposed into an amorphous Pb⁰ film (reaction (4) and (5)), and the violently released gas caused the appearance of “bubbles”.¹²⁵ As the treatment time increased, the film becomes thicker while the size of the bubbles increases. In addition, by comparing the atomic force microscope (AFM) images of spiro-MeOTAD layer before (Fig. 5.1d) and after (Fig. 5.1e) O₂ plasma treatment, it can be noticed that the plasma treatment can enormously increase the roughness of the film. Fig. A5.4 also shows that the silver electrodes are oxidized after plasma treatment. All these results clearly show that this

type of treatment is detrimental to the structural integrity of such devices and is thus not suitable for the encapsulation of perovskite solar cells.



To prevent the damage from the post plasma enhanced Al_2O_3 deposition, we further selected ethylene glycol (EG) as a precursor for the growth of an initial alucone encapsulation layer (reaction (6)).



Unlike the O_2 plasma-assisted and water-assisted treatments, the EG-treated MAPbI_3 perovskite films displayed negligible morphostructural changes, as displayed by the corresponding SEM images (Fig. 1f-i).

5.4 Strategy for the encapsulation of perovskite solar cells

In the light of these results, we constructed a novel barrier structure, as shown in Fig. 2. First, an alucone layer was deposited on perovskite solar cells at 50°C by MLD. Due to the low reactivity of EG and the moderate growth temperature, the perovskite solar cells preserved the initial performance after the deposition of alucone (Fig. A5.5). Besides, a large amount of methyl groups remained in the alucone because the growth temperature was lower than the ideal growth temperature of alucone.¹²⁶ Such methyl groups can effectively consume the O_2 plasma during the following PEALD process by the reaction (6). In conclusion, alucone can protect perovskite solar cells during the encapsulation procedure while the PEALD Al_2O_3 layer can prevent the penetration of water molecules in perovskite solar cells.

Indeed, *in-situ* quadrupole mass spectrometer (QMS) and *in-situ* quartz crystal microbalance (QCM) were used to monitor the growth of MLD alucone and PEALD Al₂O₃. Fig. 2c shows the evolution of the CH₄ by-product during the growth of alucone, which indicates that alucone achieved stable growth after 10 cycles. Based on the QCM and QMS, we designed a procedure to verify the reaction between O₂ plasma and methyl groups inside the alucone (Fig. A5.6). In order to avoid the influence of surface methyl groups, O₂ plasma was injected into the chamber after the EG precursor, when the surface exposes hydroxyl groups. The result is displayed in Fig. 5.2c. The identification of carbon dioxide (M/Z = 44) alongside with the mass gain pointed out that the methyl groups inside the film reacted with O₂ plasma. Also, Fourier-transform infrared spectroscopy (FTIR) shown a decrease in intensity of the bending and stretching vibration bands of C-H bonds (1192 - 1580 cm⁻¹)¹²⁶⁻¹²⁷ and an increase in intensity of the of bending and stretching vibration bands of Al-O bonds (459 - 950 cm⁻¹)¹²⁸⁻¹²⁹ in the alucone films after plasma treatment (Fig. 5.2d). These results certified the consumption of O₂ plasma by the alucone layer.

5.5 Properties of the encapsulation films

Fig. 3a shows a schematic diagram of the structure and cross-section SEM image of a perovskite solar cell with encapsulation layer. As mentioned above, the encapsulation layer was grown on a standard MaPbI₃ solar cell in the form of MLD-alucone/PEALD Al₂O₃. Fig. 3b illustrates the transmission electron microscopy (TEM) image of encapsulation film on the perovskite solar cells. To establish the ideal thickness of the alucone layer, we tested devices with different growing cycles of alucone (Fig. 5.3c). The results revealed an optimum protective layer of 20 cycles. The time required for the O₂ plasma to penetrate the alucone films was also tested. The results are shown in Fig. A5.7. Further, based on our previous research, we constructed an alternating

structure consisting of 20 cycles of alucone and PEALD Al₂O₃ (Fig. 5.3d). This organic-inorganic laminate structure rendered inert the defects in the inorganic Al₂O₃, which resulted in an enhanced water vapor barrier ability.¹³⁰⁻¹³¹ Leakage current testing demonstrated that this nanolaminate structure has only a few defects in comparison with the single-Al₂O₃ layers of the same thickness (Fig. 5.3e). This rationally designed alternating layer structure exhibited lower WVTR than the pure Al₂O₃ layer (Fig. 5.3f). The WVTR was calculated using the following formula:

$$\text{WVTR} = -n \cdot M_{(\text{H}_2\text{O})} / M_{(\text{Ca})} \cdot \delta_{\text{Ca}} \cdot \rho_{\text{Ca}} \cdot L / b \cdot d_{(1/R)} / d_t \quad (7)$$

where n is a stoichiometric coefficient ($n = 2$ for H₂O). $M_{(\text{H}_2\text{O})}$ and $M_{(\text{Ca})}$ correspond to the molar masses of H₂O and Ca. δ_{Ca} is the Ca resistivity, and ρ_{Ca} is the Ca density. L and b are the length and width of the Ca active layer respectively, and $(1/R)$ is the conductance measured during the tests.

In addition, the introduction of organic layer alucone increased the bending properties of the encapsulation film. The tensile properties of pure Al₂O₃ film and alternate layers on PET substrates were tested with diverse bending radiuses and a bending speed of 30 times per minute. The result is shown in Fig. A5.8. For the organic-inorganic alternating layers on PET, only slight streaks appeared at a bend radius of 5 mm. Fractures occurred when the bend radius was reduced to 3 mm. In contrast, the pure Al₂O₃ film was completely broken into multiple strips after being bent at a radius of 3 mm. Nano-scale thickness and organic composition made the alternating encapsulation layer superior in flexibility.

5.6 Application of the encapsulation on perovskite solar cells

As shown in Fig. 5.4a and Fig. 5.4b, when the optimized two-bilayers encapsulation was applied on 27 perovskite solar cells, only a 0.09% efficiency loss was noted. I-V curves of a representative

MAPbI₃ perovskite solar cell before and after the encapsulation is illustrated in Fig. A5.9. Due to the low activity of EG and O₂ plasma prevention from alucone, the performance was almost constant on both cases. In addition, perovskite solar cells with and without encapsulation immersed in water are displayed in Fig. A5.10. The devices without ALD barrier suffer from severe side penetration outside the electrodes. By contrary, the developed alternating barrier efficiently prevented the penetration of water from both the top and the sides of the devices due to the high conformality of ALD and MLD (Fig. A5.11),¹³²⁻¹³³ thus making a perfectly sealed solar cell device. Corresponding efficiency change is shown in Fig. 4c, the encapsulated devices maintained 95% the initial performance after 300 mins under water. To further prove the feasibility of outside application of the developed devices, we tested the performance of encapsulated solar cells under high-humidity atmosphere. As a result of encapsulation of the two-bilayer structure, the devices preserved 96% of initial efficiency after over 2000 hours exposure at 80% relative humidity and 30 °C (Fig. 5.4d). These performances reveal the promising prospect of this device for outside application and as a potential floating solar energy generator.

5.7 Conclusions

In summary, using MLD/PEALD, we have successfully encapsulated a metal halide perovskite solar cell at 50 °C. The protective alucone layer prepared by MLD effectively prevented the damage that O₂ plasma in PEALD could cause without changing the high performance of encapsulated devices. Therefore, the efficient plasma-assisted deposition method was groundbreaking grown on perovskite solar cells. As a result, the devices survived in high-humidity environment without decreasing the performance. We are confident that we provided a straightforward, efficient and simple method to grow high-quality thin film encapsulation useful

for developing highly sensitive devices such as metal halide perovskite, which alongside with the obtained insight, might boost a significant breakthrough in the commercialization of perovskite solar cells.

References

[1] I.S. Sang, M. Grätzel, N.G. Park

Methodologies toward Highly Efficient Perovskite Solar Cells

Small, 14 (2018) 1704177.

[2] H.S. Kim, C.-R. Lee, J.-H. Im, K.-B. Lee, T. Moehl, A. Marchioro, S.-J. Moon, R. Humphry-Baker, J.-H. Yum, J.E. Moser

Lead Iodide Perovskite Sensitized All-Solid-State Submicron Thin Film Mesoscopic Solar Cell with Efficiency Exceeding 9%

Sci. Rep., 2 (2012) 591.

[3] N.R.E. Laboratory

Cell Efficiency Chart

<https://www.nrel.gov/pv/cell-efficiency.html>.

[4] D. Wang, M. Wright, N.K. Elumalai, A. Uddin

Stability of perovskite solar cells

Sol. Energy Mater. Sol. Cells, 147 (2016) 255-275.

[5] R. Wang, J. Xue, L. Meng, J.-W. Lee, Z. Zhao, P. Sun, L. Cai, T. Huang, Z. Wang, Z.-K. Wang, Y. Duan, J.L. Yang, S. Tan, Y. Yuan, Y. Huang, Y. Yang

Caffeine Improves the Performance and Thermal Stability of Perovskite Solar Cells

Joule, 3 (2019) 1464-1477.

[6] M.B. Islam, M. Yanagida, Y. Shirai, Y. Nabetani, K. Miyano

Highly stable semi-transparent MAPbI₃ perovskite solar cells with operational output for 4000 h

Sol. Energy Mater. Sol. Cells, 195 (2019) 323-329.

[7] Y. Zheng, W. Shi, J. Kong, D. Huang, H.E. Katz, J. Yu, A.D. Taylor

A Cytop Insulating Tunneling Layer for Efficient Perovskite Solar Cells

Small Methods, 1 (2017) 1700244.

[8] R. Wang, M. Mujahid, Y. Duan, Z.-K. Wang, J. Xue, Y. Yang

A Review of Perovskites Solar Cell Stability

Adv. Funct. Mater., 0 1808843.

[9] E. Ramasamy, V. Karthikeyan, K. Rameshkumar, G. Veerappan

Glass-to-glass encapsulation with ultraviolet light curable epoxy edge sealing for stable perovskite solar cells

Mater. Lett., 250 (2019) 51-54.

[10] S. Ito, S. Tanaka, K. Manabe, H. Nishino

Effects of Surface Blocking Layer of Sb₂S₃ on Nanocrystalline TiO₂ for CH₃NH₃PbI₃ Perovskite Solar Cells

J. Phys. Chem. C, 118 (2014) 16995-17000.

[11] P. Castell, M. Wouters, H. Fischer, G. De With

Kinetic studies of a UV-curable powder coating using photo-DSC, real-time FTIR and rheology

J. Coat. Technol. Res., 4 (2007) 411-423.

[12] J.J. Michels, M. Peter, A. Salem, B. van Remoortere, J. van den Brand

A combined experimental and theoretical study on the side ingress of water into barrier adhesives for organic electronics applications

J. Mater. Chem. C, 2 (2014) 5759-5768.

[13] R.L. Puurunen

Growth Per Cycle in Atomic Layer Deposition: A Theoretical Model

Chem. Vap. Deposition, 9 (2003) 249-257.

[14] J.T. Gudmundsson, N. Brenning, D. Lundin, U. Helmersson

High power impulse magnetron sputtering discharge

J. Vac. Sci. Technol., A, 30 (2012) 35.

[15] S.T. Barry, A.V. Teplyakov, F. Zaera

The Chemistry of Inorganic Precursors during the Chemical Deposition of Films on Solid Surfaces

Acc. Chem. Res., 51 (2018) 800-809.

[16] D. Yu, Y.Q. Yang, Z. Chen, Y. Tao, Y.F. Liu

Recent progress on thin-film encapsulation technologies for organic electronic devices

Opt. Commun., 362 (2016) 43-49.

[17] E.G. Jeong, Y. Jeon, S.H. Cho, K.C. Choi

Textile-based washable polymer solar cells for optoelectronic modules: toward self-powered smart clothing

Energy Environ. Sci., (2019).

[18] B. Conings, J. Drijkoningen, N. Gauquelin, A. Babayigit, J. D'Haen, L. D'Olieslaeger, A.

Ethirajan, J. Verbeeck, J. Manca, E. Mosconi, F. De Angelis, H.G. Boyen

Intrinsic Thermal Instability of Methylammonium Lead Trihalide Perovskite

Adv. Energy Mater., 5 (2015) 8.

[19] N.J. Jeon, H. Na, E.H. Jung, T.-Y. Yang, Y.G. Lee, G. Kim, H.-W. Shin, S.I. Seok, J. Lee, J. Seo

A fluorene-terminated hole-transporting material for highly efficient and stable perovskite solar cells

Nat. Energy, 3 (2018) 682-+.

[20] F. Matteocci, L. Cina, E. Lamanna, S. Cacovich, G. Divitini, P.A. Midgley, C. Ducati, A. Di Carlo

Encapsulation for long-term stability enhancement of perovskite solar cells

Nano Energy, 30 (2016) 162-172.

[21] Y.I. Lee, N.J. Jeon, B.J. Kim, H. Shim, T.-Y. Yang, S.I. Seok, J. Seo, S.G. Im

A Low-Temperature Thin-Film Encapsulation for Enhanced Stability of a Highly Efficient Perovskite Solar Cell

Adv. Energy Mater., 8 (2018).

[22] Y.F. Lv, P.H. Xu, G.Q. Ren, F. Chen, H.R. Nan, R.Q. Liu, D. Wang, X. Tan, X.Y. Liu, H. Zhang, Z.K. Chen

Low-Temperature Atomic Layer Deposition of Metal Oxide Layers for Perovskite Solar Cells with High Efficiency and Stability under Harsh Environmental Conditions

ACS Appl. Mater. Interfaces, 10 (2018) 23928-23937.

[23] G.S. Higashi, C.G. Fleming

Sequential surface chemical reaction limited growth of high quality Al₂O₃ dielectrics

Appl. Phys. Lett., 55 (1989) 1963-1965.

[24] H. Wang, Y. Liu, H. Liu, Z. Chen, P. Xiong, X. Xu, F. Chen, K. Li, Y. Duan

Effect of Various Oxidants on Reaction Mechanisms, Self-Limiting Natures and Structural Characteristics of Al₂O₃ Films Grown by Atomic Layer Deposition

Adv. Mater. Interfaces, 5 (2018).

[25] H.B. Profijt, S.E. Potts, M.C.M. van de Sanden, W.M.M. Kessels

Plasma-Assisted Atomic Layer Deposition: Basics, Opportunities, and Challenges

J. Vac. Sci. Technol., A, 29 (2011).

[26] N.J. Jeon, J.H. Noh, Y.C. Kim, W.S. Yang, S. Ryu, S.I. Seok

Solvent engineering for high-performance inorganic–organic hybrid perovskite solar cells

Nature Materials, 13 (2014) 897.

[27] E.J. Juarez-Perez, L.K. Ono, M. Maeda, Y. Jiang, Z. Hawash, Y. Qi

Photodecomposition and thermal decomposition in methylammonium halide lead perovskites and inferred design principles to increase photovoltaic device stability

J. Mater. Chem. A, 6 (2018) 9604-9612.

[28] A.A. Dameron, D. Seghete, B.B. Burton, S.D. Davidson, A.S. Cavanagh, J.A. Bertrand, S.M.

George

Molecular layer deposition of alucone polymer films using trimethylaluminum and ethylene glycol

Chem. Mater., 20 (2008) 3315-3326.

[29] D.N. Goldstein, J.A. McCormick, S.M. George

Al₂O₃ Atomic Layer Deposition with Trimethylaluminum and Ozone Studied by in Situ

Transmission FTIR Spectroscopy and Quadrupole Mass Spectrometry

The Journal of Physical Chemistry C, 112 (2008) 19530-19539.

[30] N. Batra, J. Gope, Vandana, J. Panigrahi, R. Singh, P.K. Singh

Influence of deposition temperature of thermal ALD deposited Al₂O₃ films on silicon surface passivation

AIP Advances, 5 (2015) 067113.

[31] B.H. Lee, B. Yoon, V.R. Anderson, S.M. George

Alucone Alloys with Tunable Properties Using Alucone Molecular Layer Deposition and Al₂O₃ Atomic Layer Deposition

The Journal of Physical Chemistry C, 116 (2012) 3250-3257.

[32] W. Xiao, D.Y. Hui, C. Zheng, D. Yu, Y.Y. Qiang, C. Ping, C.L. Xiang, Z. Yi

A flexible transparent gas barrier film employing the method of mixing ALD/MLD-grown Al₂O₃ and alucone layers

Nanoscale Res. Lett., 10 (2015) 130.

[33] M. Park, S. Oh, H. Kim, D. Jung, D. Choi, J.-S. Park

Gas diffusion barrier characteristics of Al₂O₃/alucone films formed using trimethylaluminum, water and ethylene glycol for organic light emitting diode encapsulation

Thin Solid Films, 546 (2013) 153-156.

[34] M. Knez, K. Niesch, L. Niinistö

Synthesis and surface engineering of complex nanostructures by atomic layer deposition

Adv. Mater., 19 (2007) 3425-3438.

[35] O. Sneh, R.B. Clark-Phelps, A.R. Londergan, J. Winkler, T.E. Seidel

Thin film atomic layer deposition equipment for semiconductor processing

Thin Solid Films, 402 (2002) 248-261.

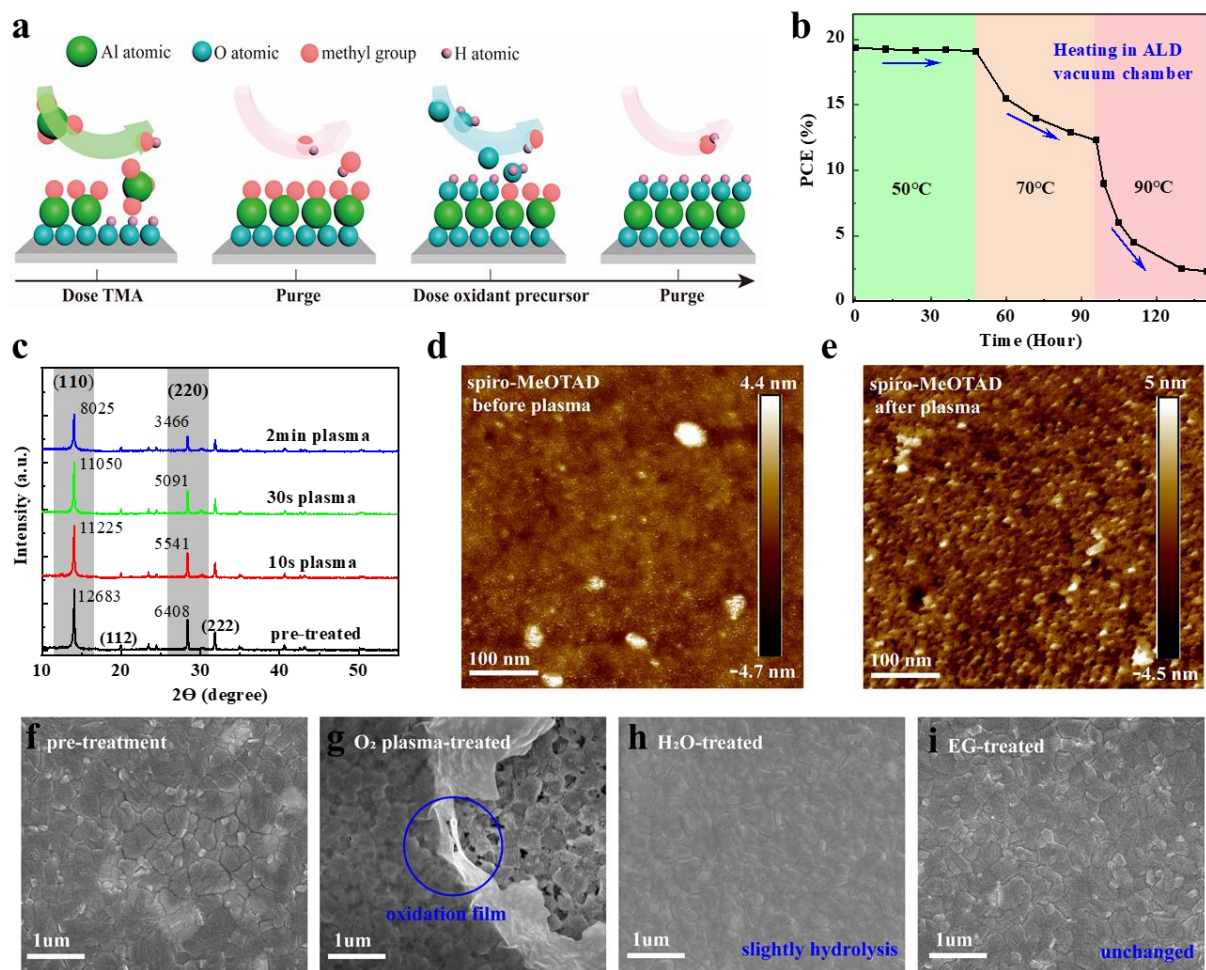


Figure 5.1. Damage of perovskite solar cells caused by the encapsulation temperature and precursors of atomic layer deposition. (a) Schematic diagram of the atomic layer deposition. (b) Degradation of perovskite solar cells caused by heating at different temperature. (c) XRD patterns of MaPbI_3 after O_2 plasma treatment for different intervals of time. AFM images of spiro-MeOTAD (d) before and (e) after O_2 plasma treatment. SEM images of the MaPbI_3 films (f) before and after the treatment with (g) O_2 plasma, (h) H_2O , and (i) EG.

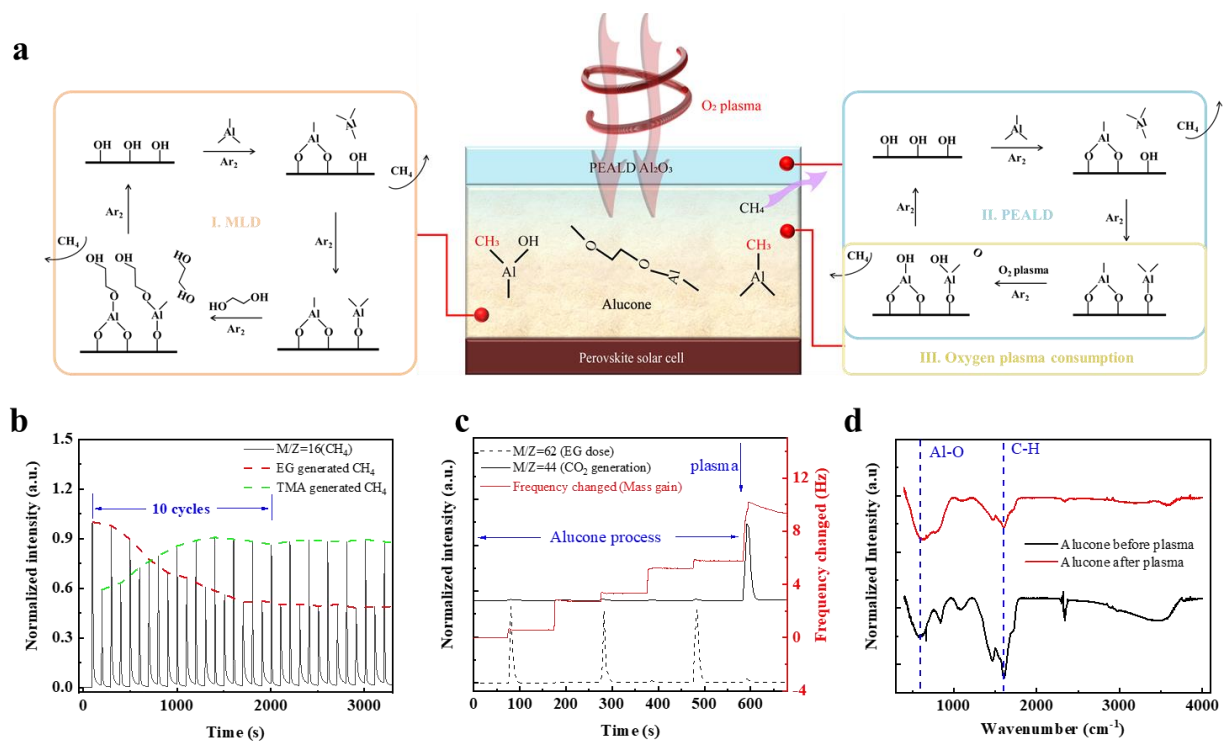


Figure 5.2. Improved encapsulation strategy and its verification. (a) Schematic diagram of the encapsulation process: (I) molecular layer deposition of alucone on the perovskite solar cell, (II) plasma-assisted atomic layer deposition of Al_2O_3 on the alucone and (III) methyl groups in the alucone consumed the O_2 plasma generated by the PEALD process and protected the perovskite solar cells. (b) Time evolution of the methane by-product during the initial growth of MLD alucone monitored by *in-situ* QMS. (c) *In-situ* QCM and QMS results for the reaction between alucone and O_2 plasma. (d) Fourier-transform infrared spectra of alucone films before and after O_2 plasma treatment.

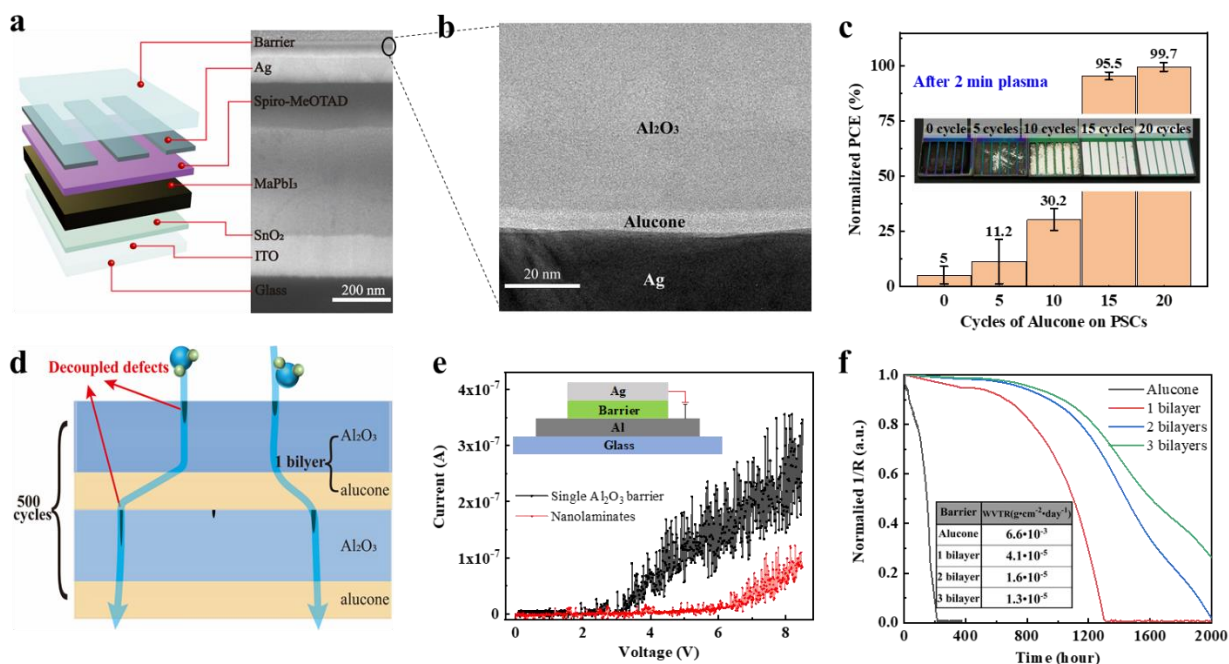


Figure 5.3. Characterization of the properties of encapsulation films. (a) Structure schematic diagram of the perovskite solar cell and cross-section SEM image of perovskite solar cell with encapsulation layer. (b) TEM image of barrier layer on the perovskite solar cells. (c) Remained efficiencies of perovskite solar cells with different cycles of alucone after O₂ plasma treatment. (d) Schematic diagram of the organic-inorganic nanolaminate structure showing the passivation of the defects and protection against water vapor permeation. (e) Leakage current of barrier layers as a function of voltage. (f) Water vapor transmission rate of different encapsulation structures under the same cycle number.

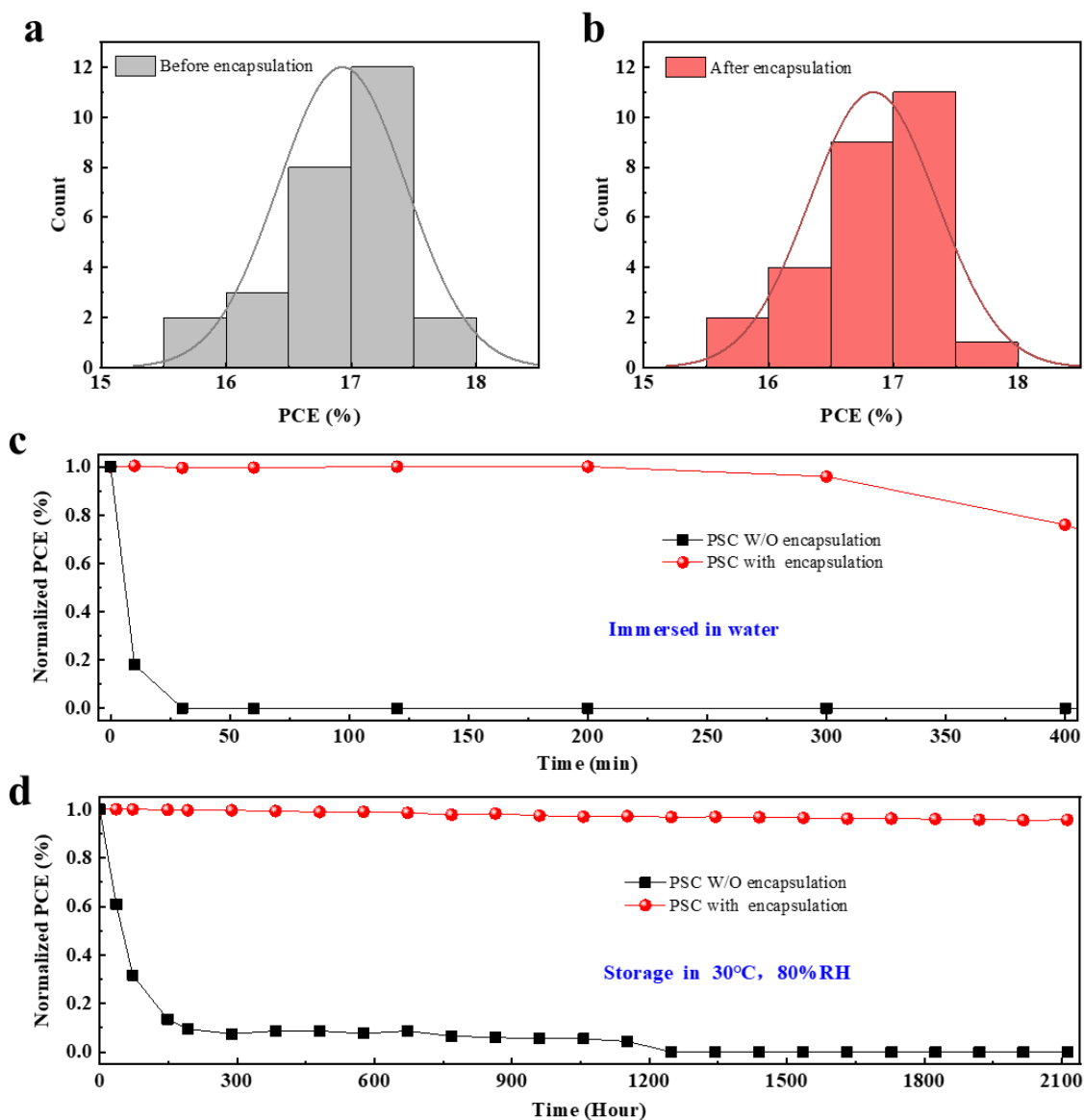


Figure 5.4. Stability tests of the encapsulated perovskite solar cells. Efficiency of 27 perovskite solar cells (a) before and (b) after encapsulation. Time evolution of normalized PCE for the perovskite solar cells with and without encapsulation (c) in water and (d) under a high-humidity environment.

Appendix A

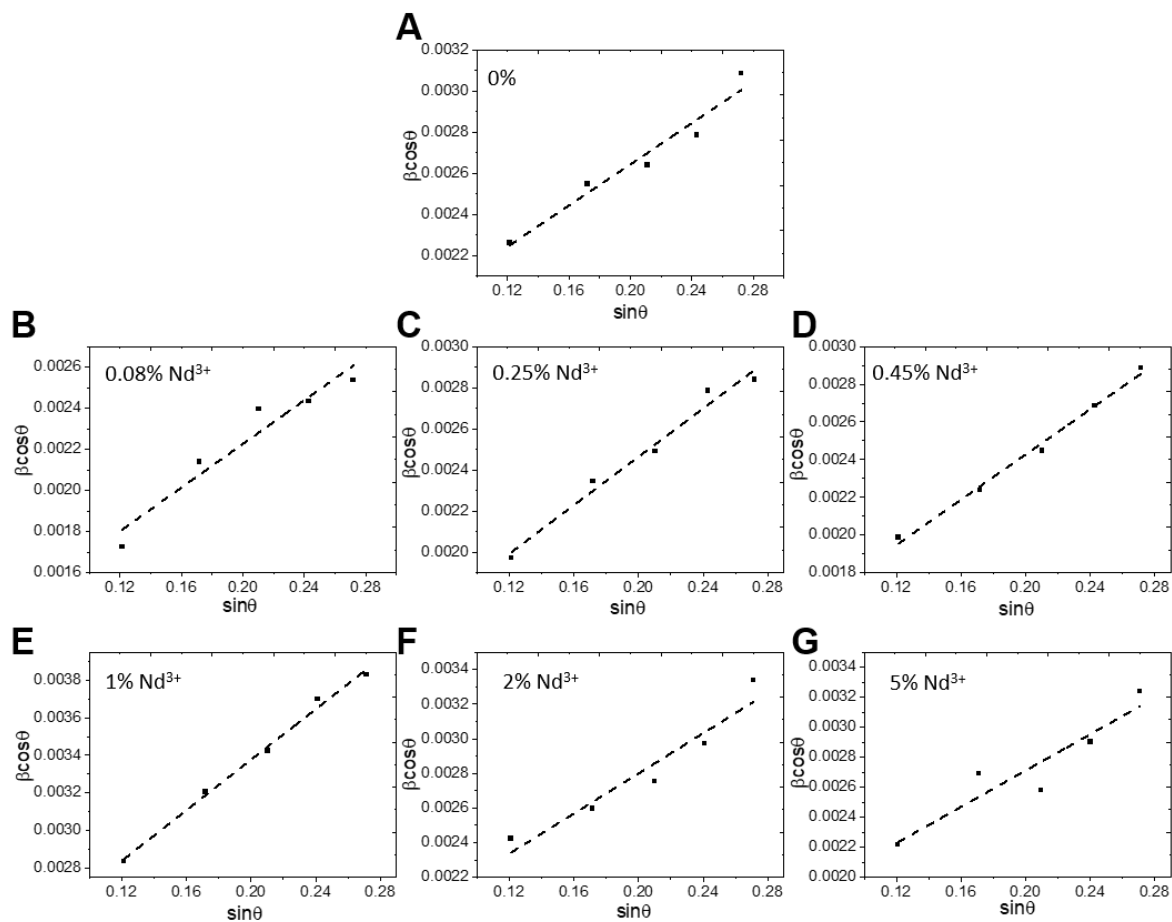


Figure A2.1 | Williamson-Hall analysis of a-FAPbI₃ with Nd³⁺ doping concentration from 0% to 5%. The filled squares are measured data and dashed lines are fitted lines.

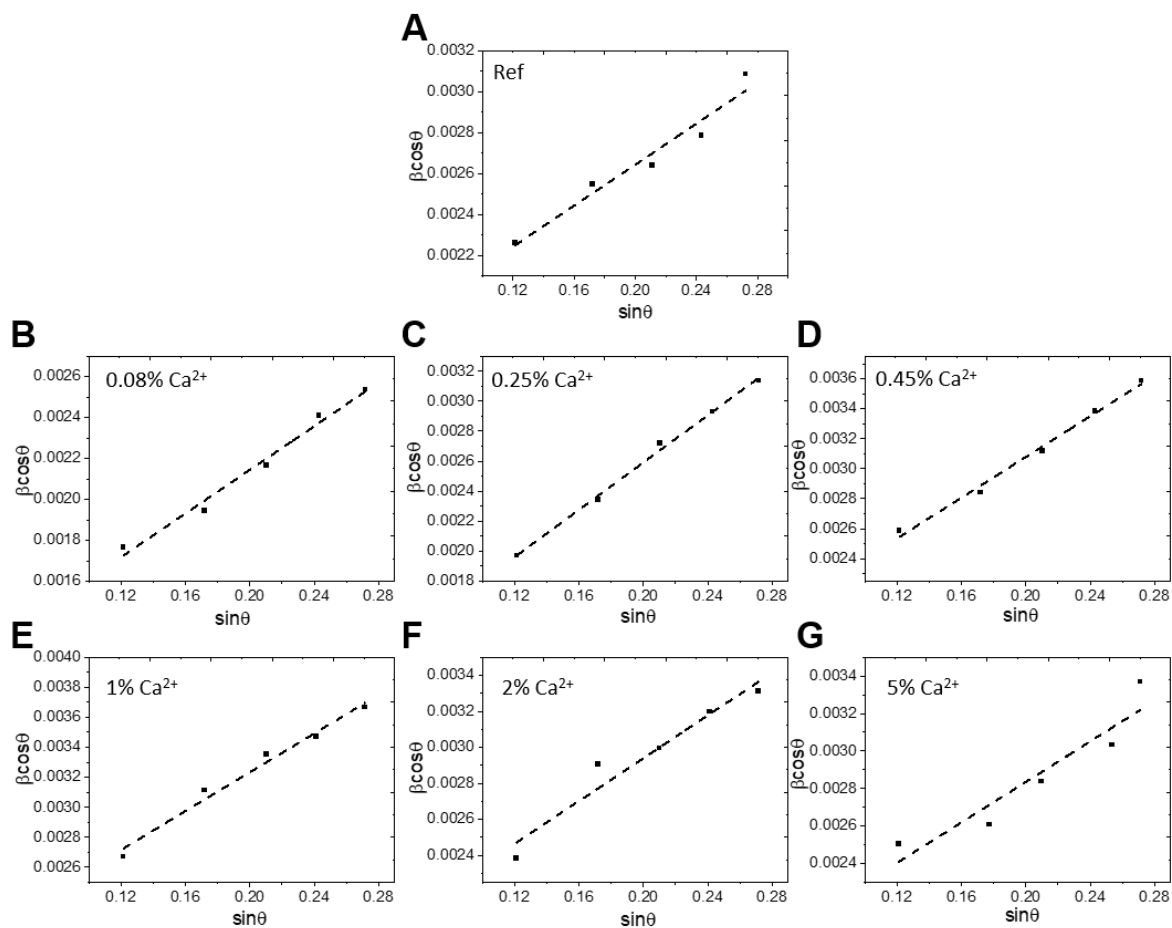


Figure A2.2 | Williamson-Hall analysis of a-FAPbI₃ with Ca²⁺ doping concentration from 0% to 5%. The filled squares are measured data and dashed lines are fitted lines.

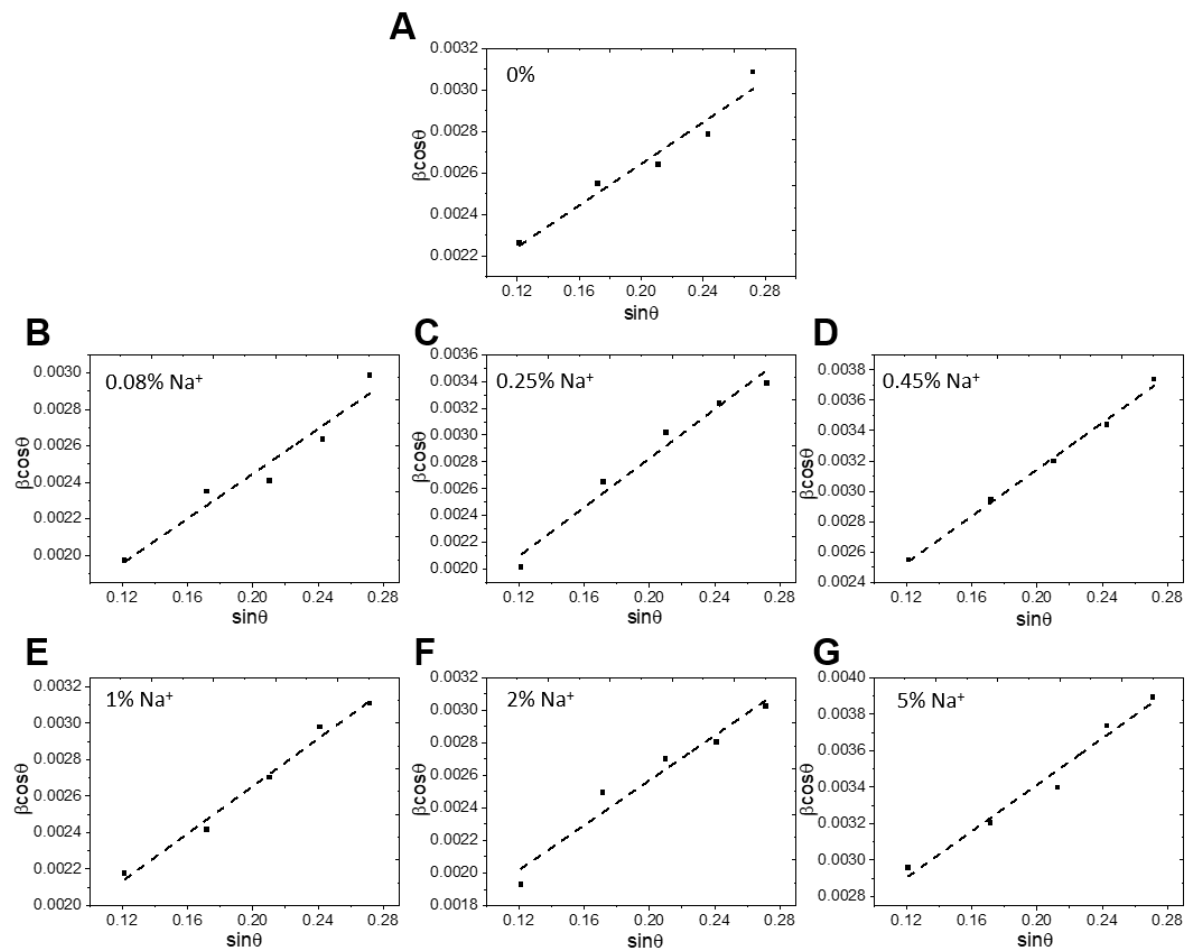


Figure A2.3 | Williamson-Hall analysis of a-FAPbI₃ with Na⁺ doping concentration from 0% to 5%. The filled squares are measured data and dashed lines are fitted lines.

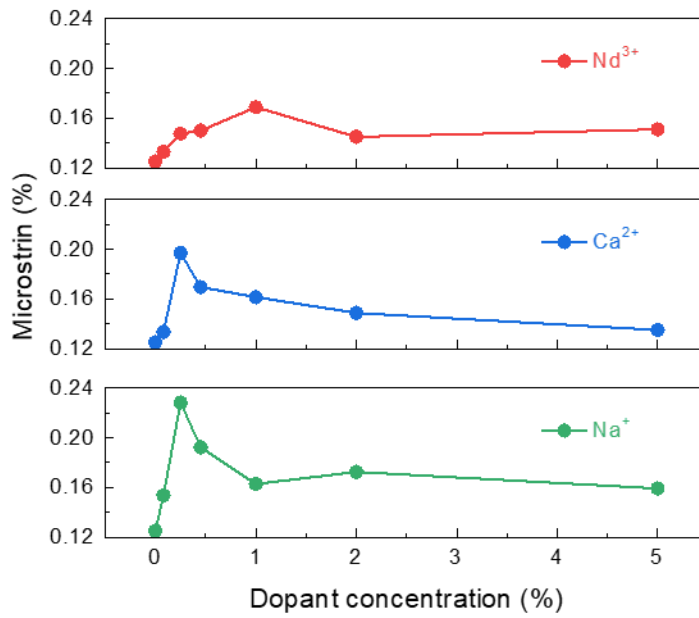


Figure A2.4 | Microstrain of the a-FAPbI₃ with Nd^{3+} , Ca^{2+} , Na^+ and doping concentration from 0% to 5%.

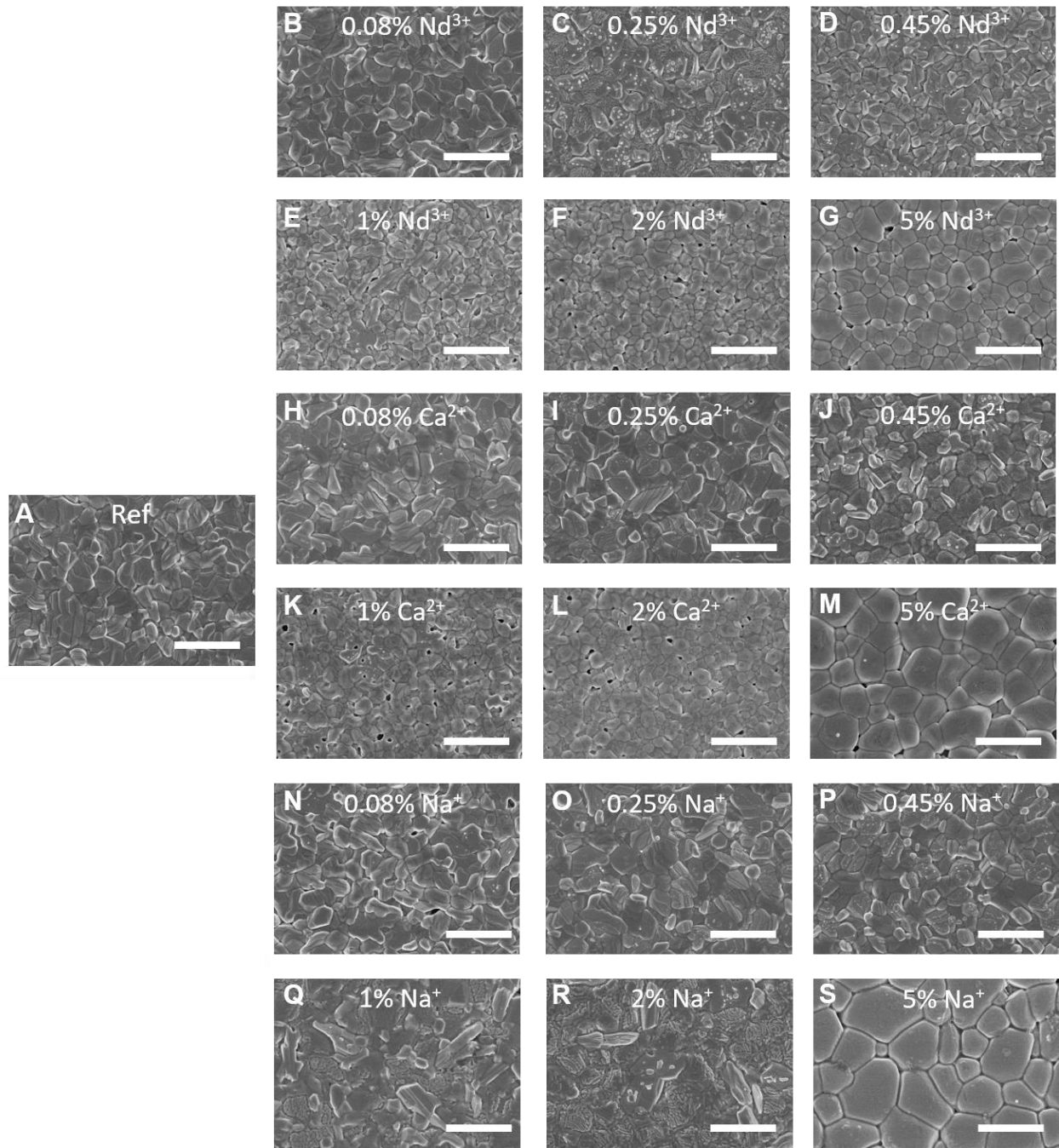


Figure A2.5 | SEM images of the perovskite films without (A) and with Nd³⁺ doping concentration from 0% to 5% (B to G); B. Ca²⁺ doping concentration from 0% to 5% (H to M); and C. Na⁺ doping concentration from 0% to 5% (N to S).

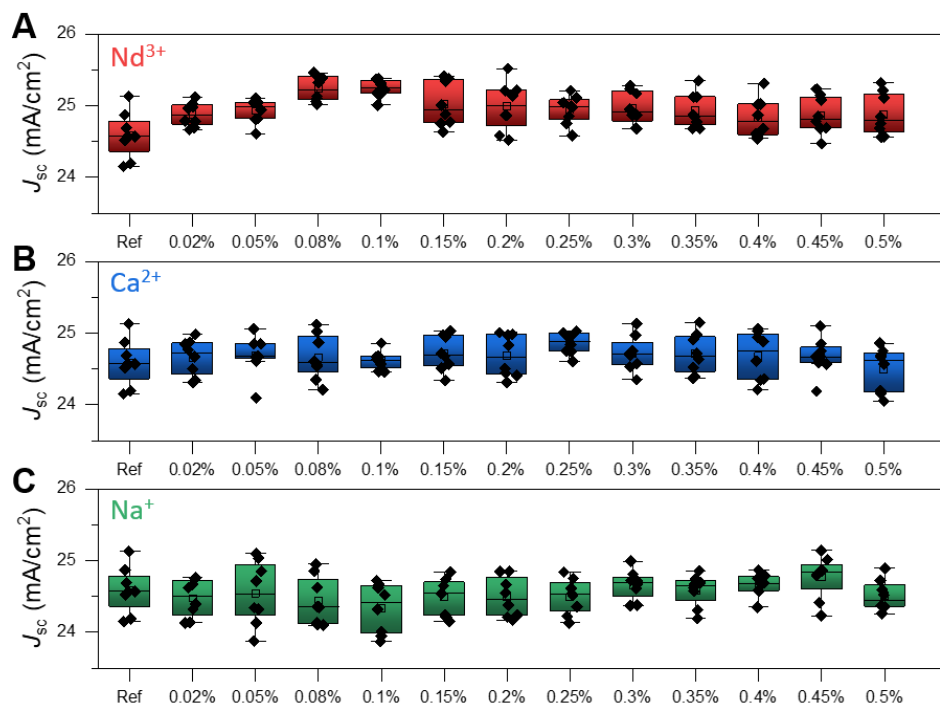


Figure A2.6 | Statistical short-circuit currents (J_{sc}) of devices with different concentrations of Nd^{3+} , Ca^{2+} , or Na^{+} incorporation.

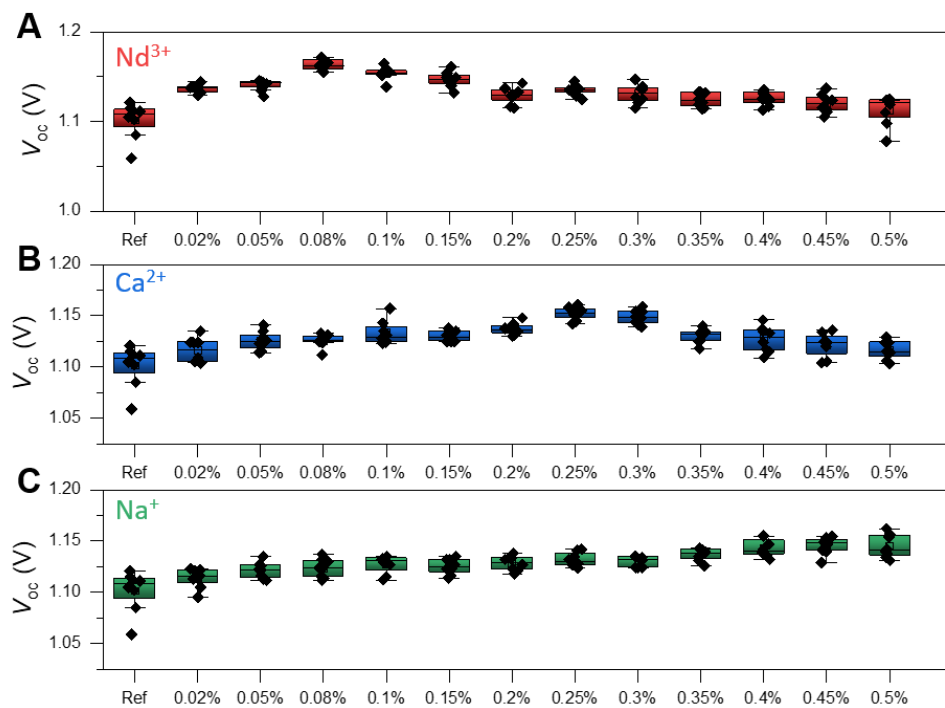


Figure A2.7 | Statistical open-circuit voltages (V_{oc} s) of devices with different concentrations of Nd^{3+} , Ca^{2+} , or Na^{+} incorporation.

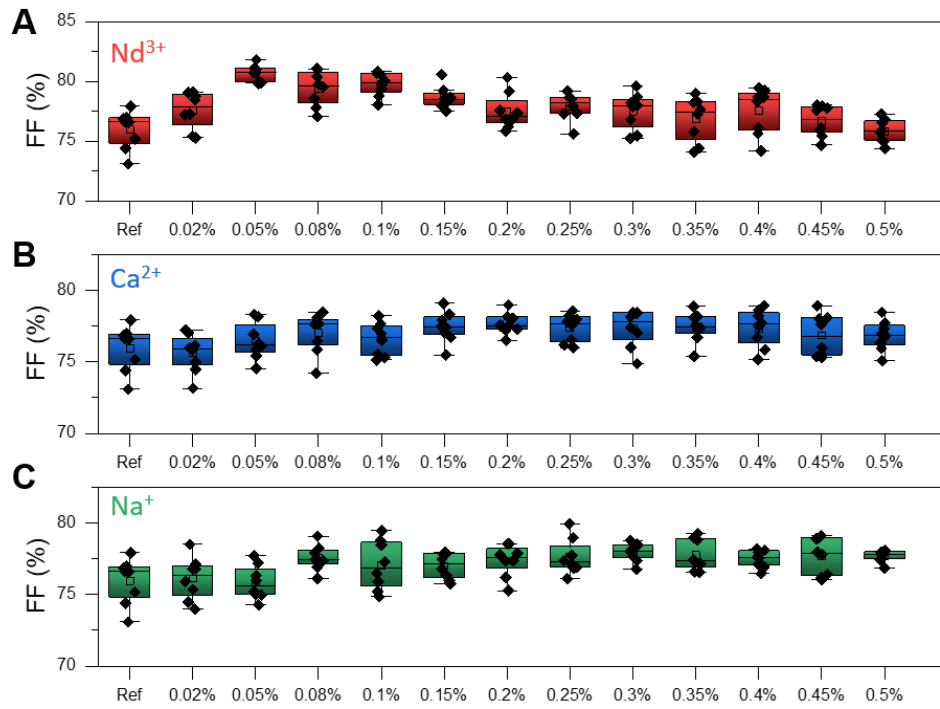


Figure A2.8 | Statistical fill factors (FFs) of devices with different concentrations of Nd^{3+} , Ca^{2+} , or Na^{+} incorporation.

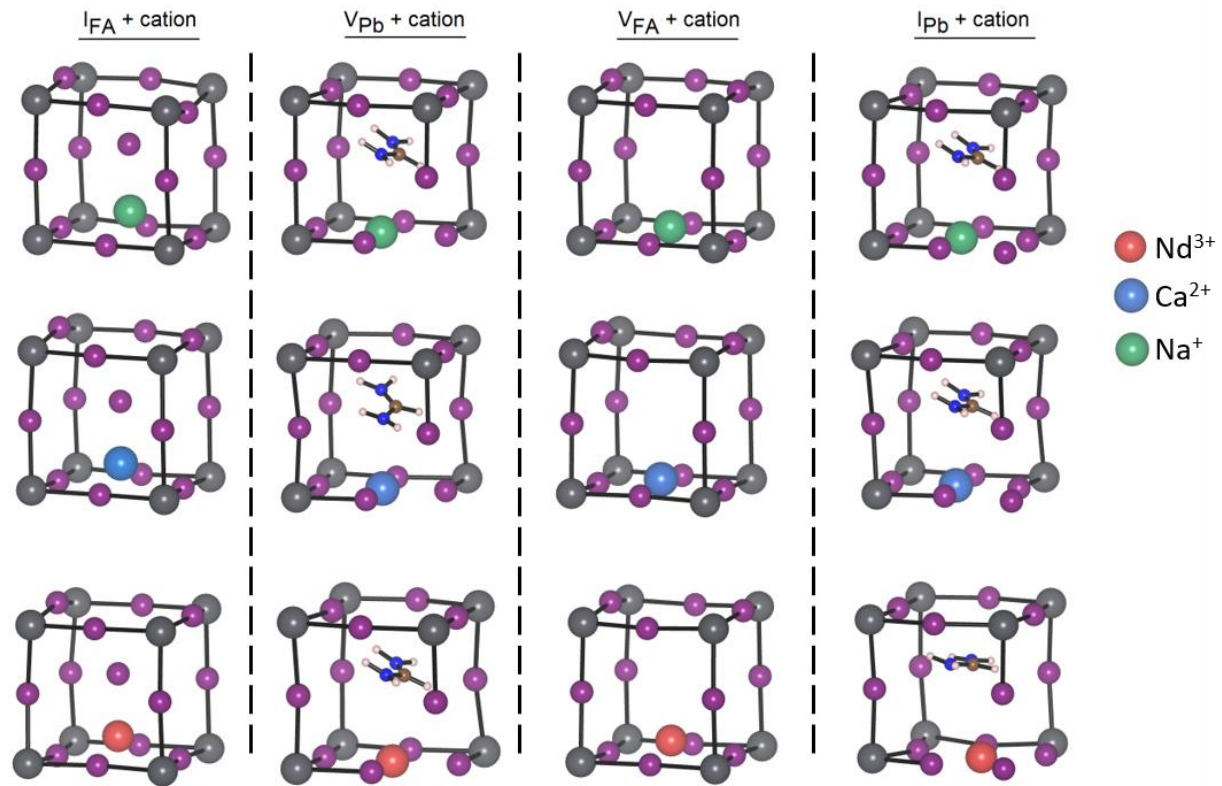


Figure A2.9 | Graphical illustrations of the cations interacting with the point defects.

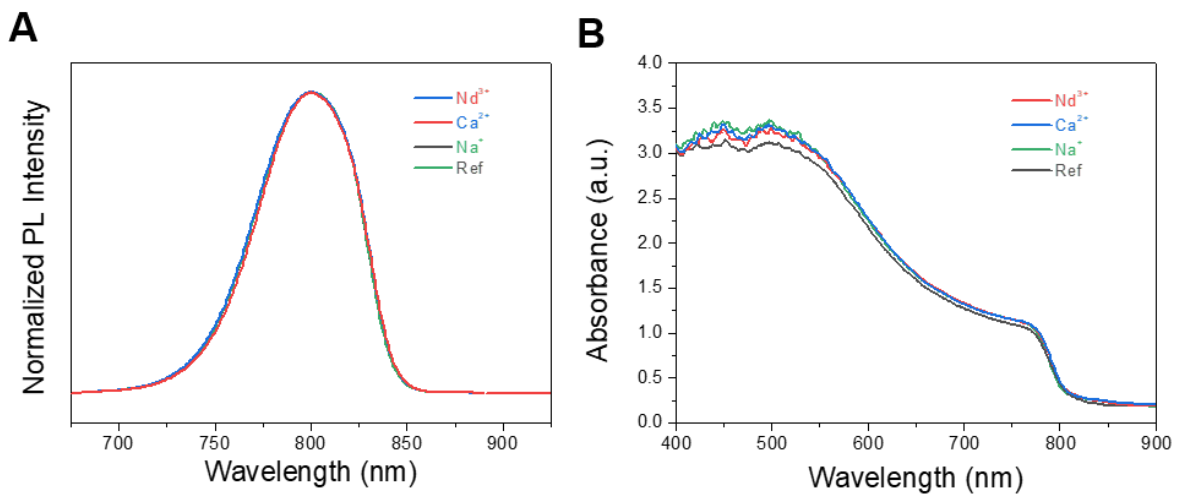


Figure A2.10 | (A) Normalized PL and (B) UV-vis spectra of perovskite films without or with the optimal cation doping concentrations.

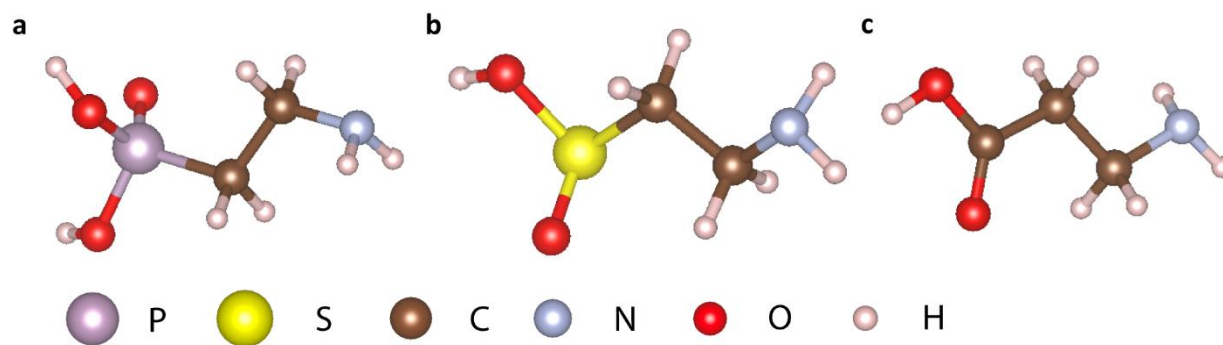


Figure A3.1 | Molecular structures of a) 2-aminoethylphosphonic acid, b) hypotaurine, and c) β -alanine.

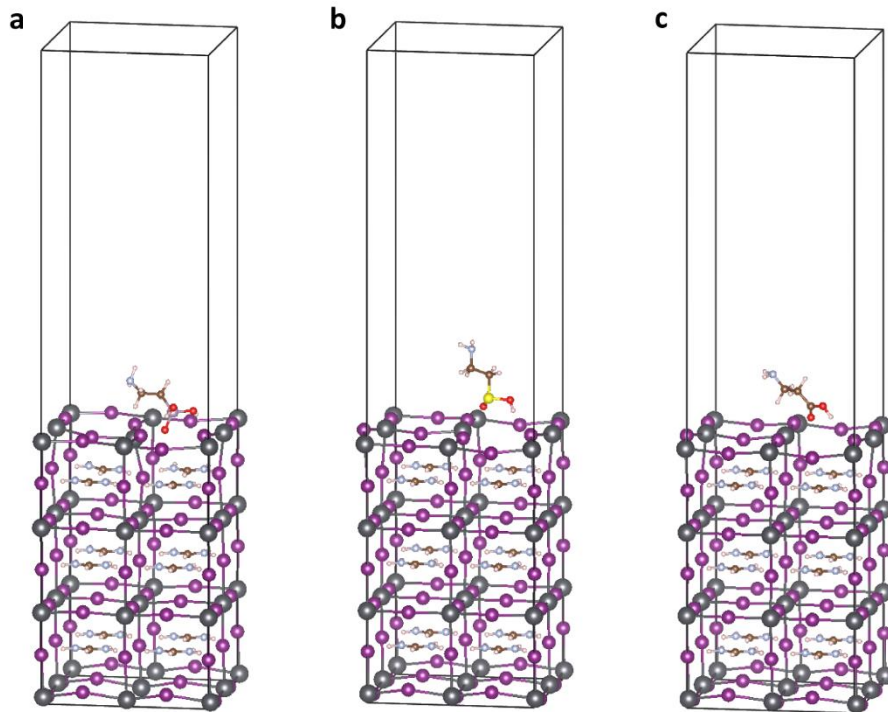


Figure A3.2 | Side views of theoretical models of perovskite with molecular surface passivation of V₁ defects with a). 2-aminoethylphosphonic acid, d). hypotaurine, and g). β-alanine.

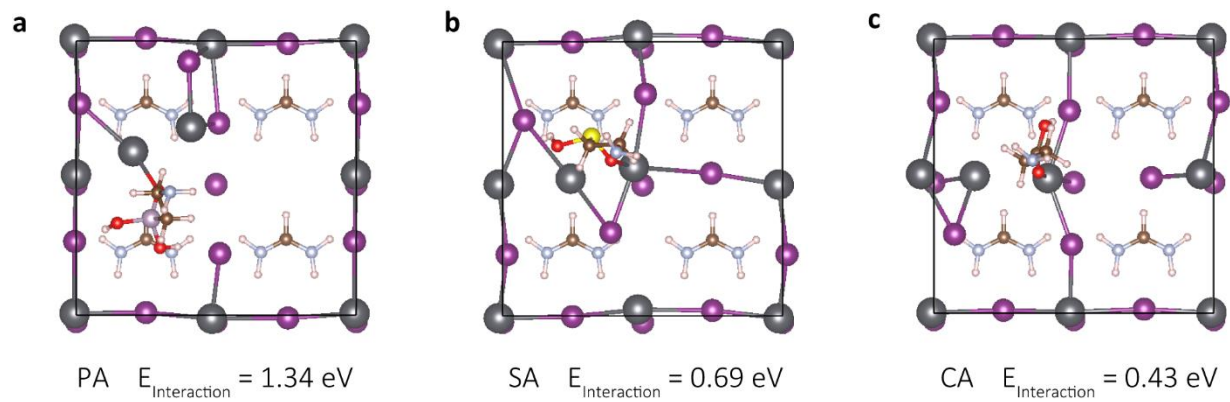


Figure A3.3 | Side views of theoretical models of perovskite with molecular surface passivation of Pb_I defects with a). 2-aminoethylphosphonic acid (PA), d). hypotaurine (SA), and g). β -alanine (CA).

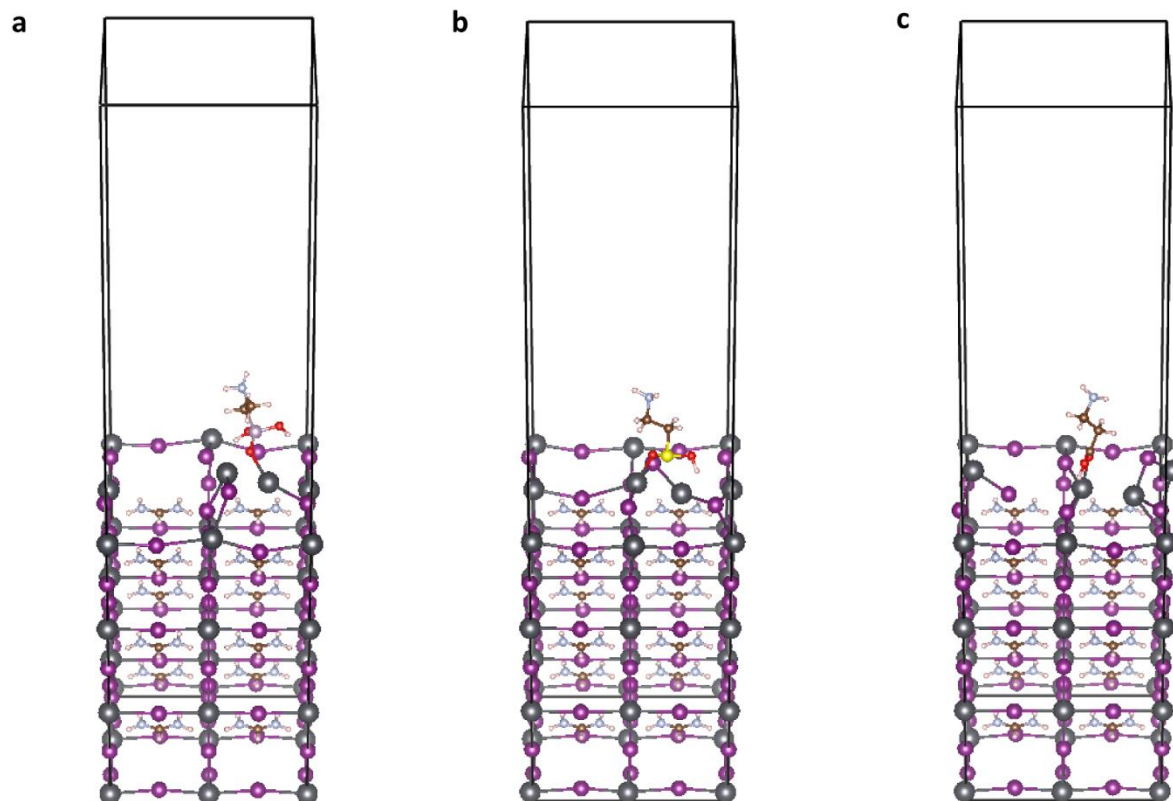


Figure A3.4 | Side views of theoretical models of perovskite with molecular surface passivation of Pb_I defects with a). 2-aminoethylphosphonic acid, d). hypotaurine, and g). β -alanine.

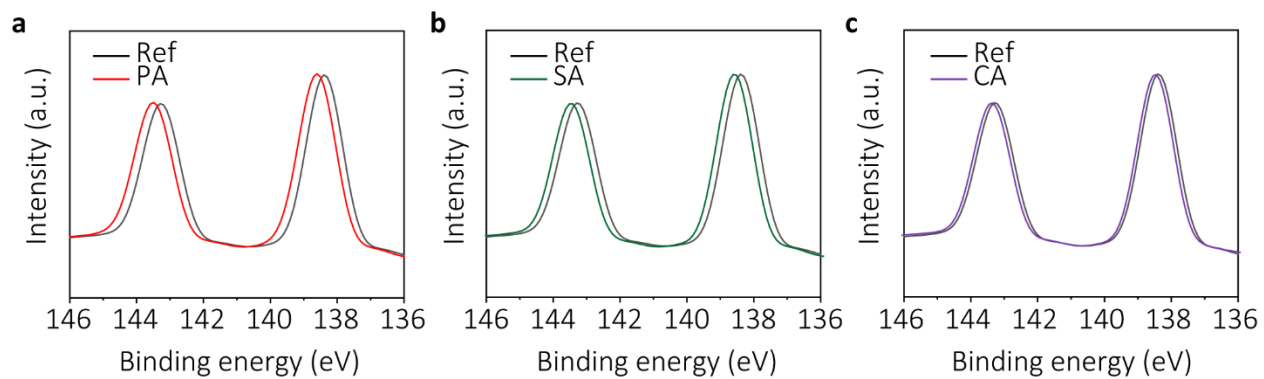


Figure A3.5 | XPS data for Pb 4f 7/2 and Pb 4f 5/2 core-level spectra in perovskite films with or without additives.

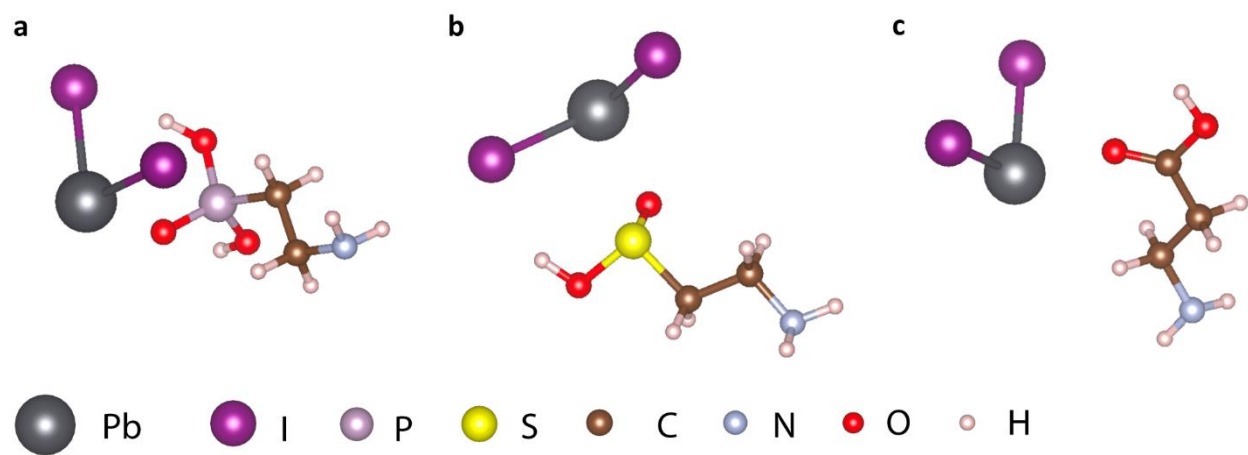


Figure A3.6 | Adduct formation of PbI_2 molecules with a) 2-aminoethylphosphonic acid, b) hypotaurine, and c) β -alanine.

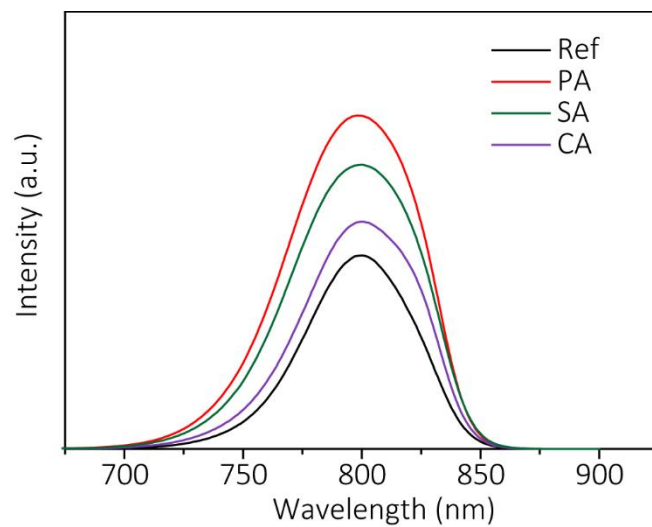


Figure A3.7 | Steady-state photoluminescence (PL) spectra of perovskite films with different molar ratios of additives.

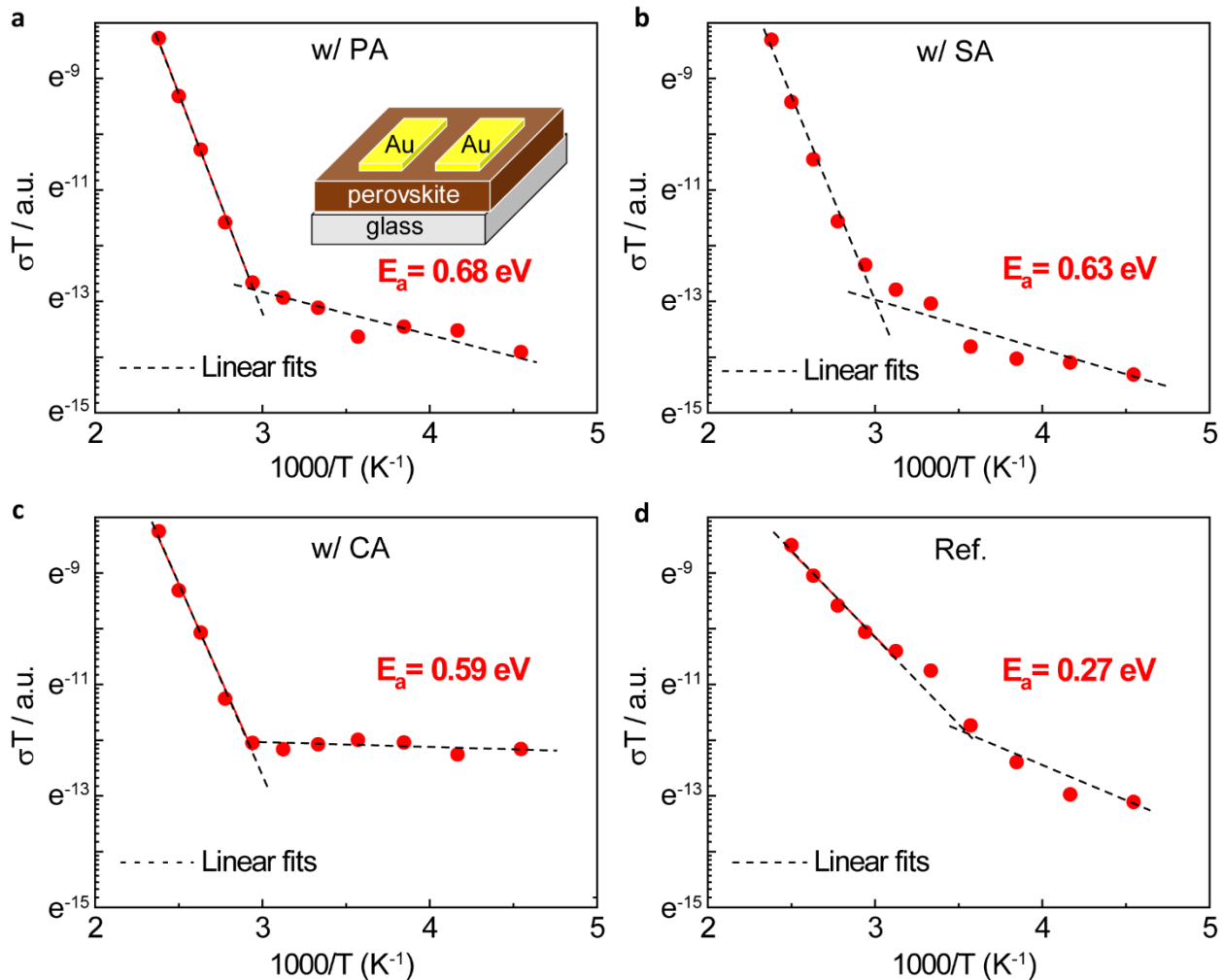


Figure A3.8 | a)-d). Temperature-dependent conductivity of the lateral devices with 2-aminoethylphosphonic acid (PA), hypotaurine (SA) and β -alanine additives (CA) or without additives.

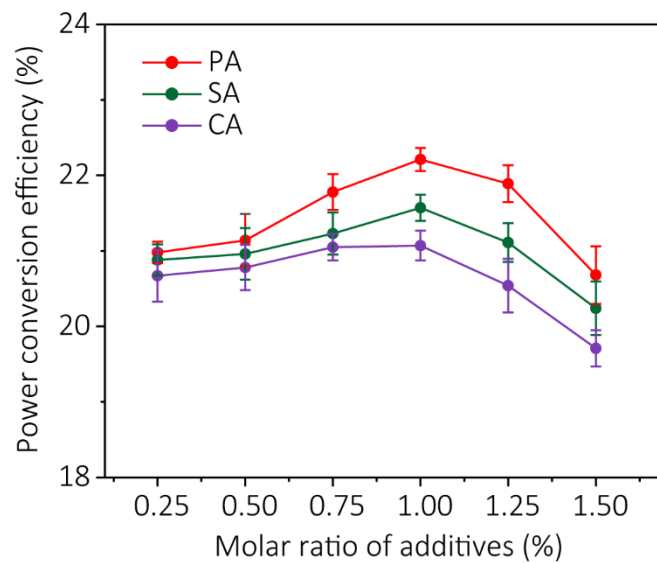


Figure A3.9 | Power conversion efficiencies of devices with different molar ratios to PbI_2 in the precursor solutions.

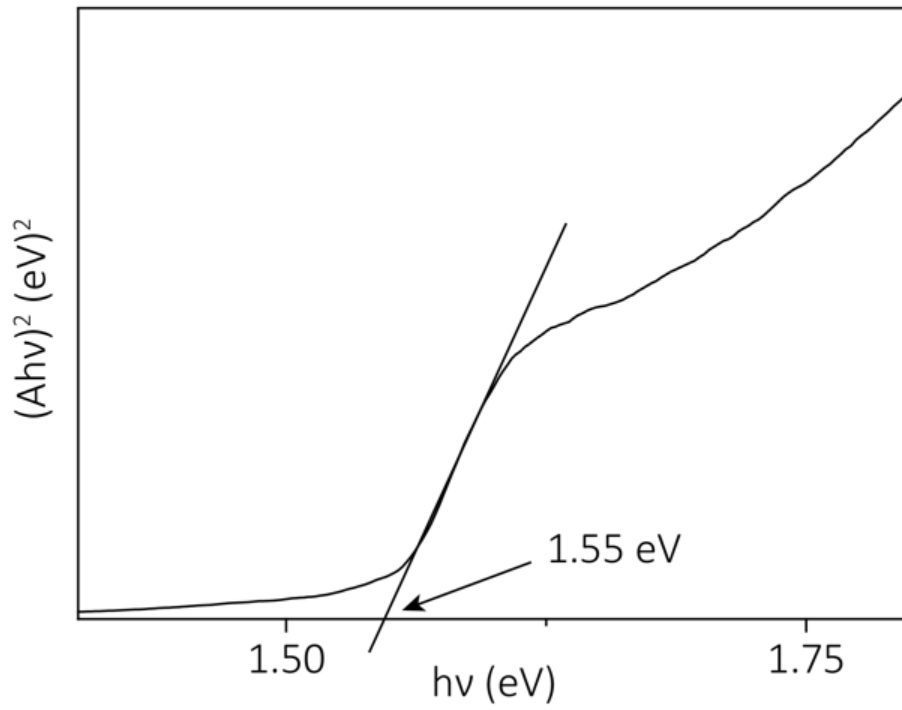


Figure A4.1. Tauc plot of perovskite thin film. The line indicates a bandgap of about 1.55 eV.

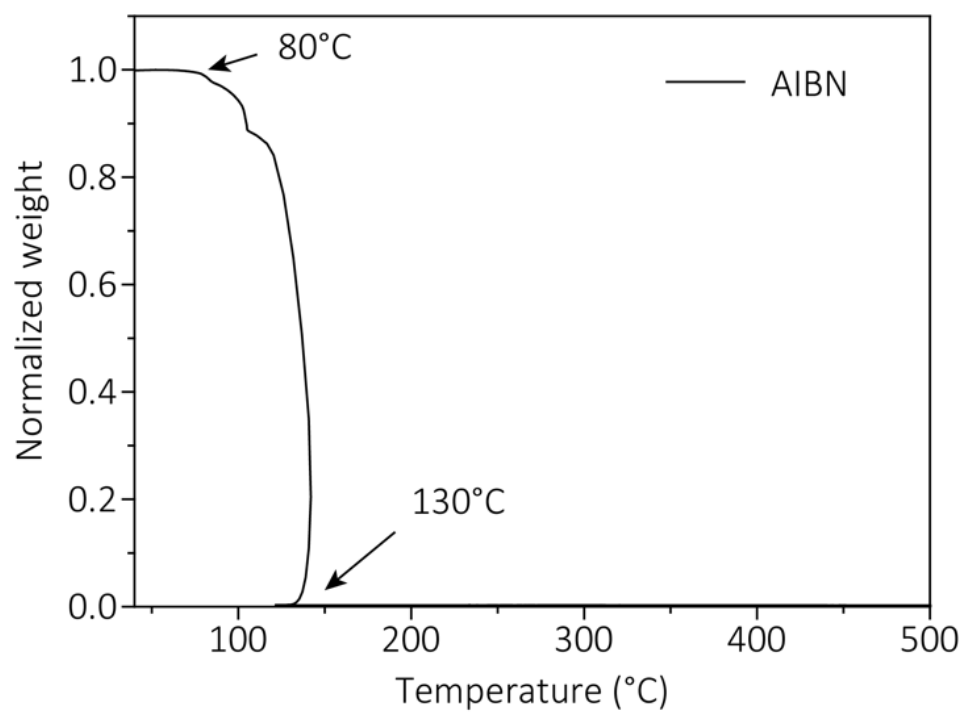


Figure A4.2. Thermogravimetric analysis (TGA) of the initiator (AIBN).

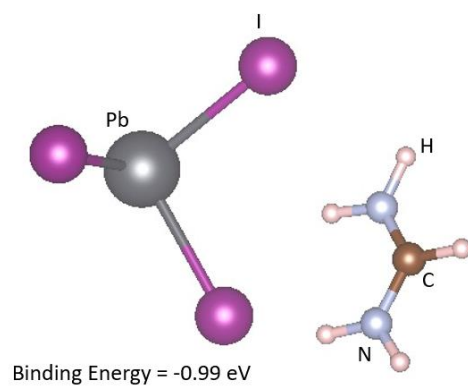


Figure A4.3. computational study of most favorable molecular configurations and binding energies between the PbI₂ molecule and FAI.

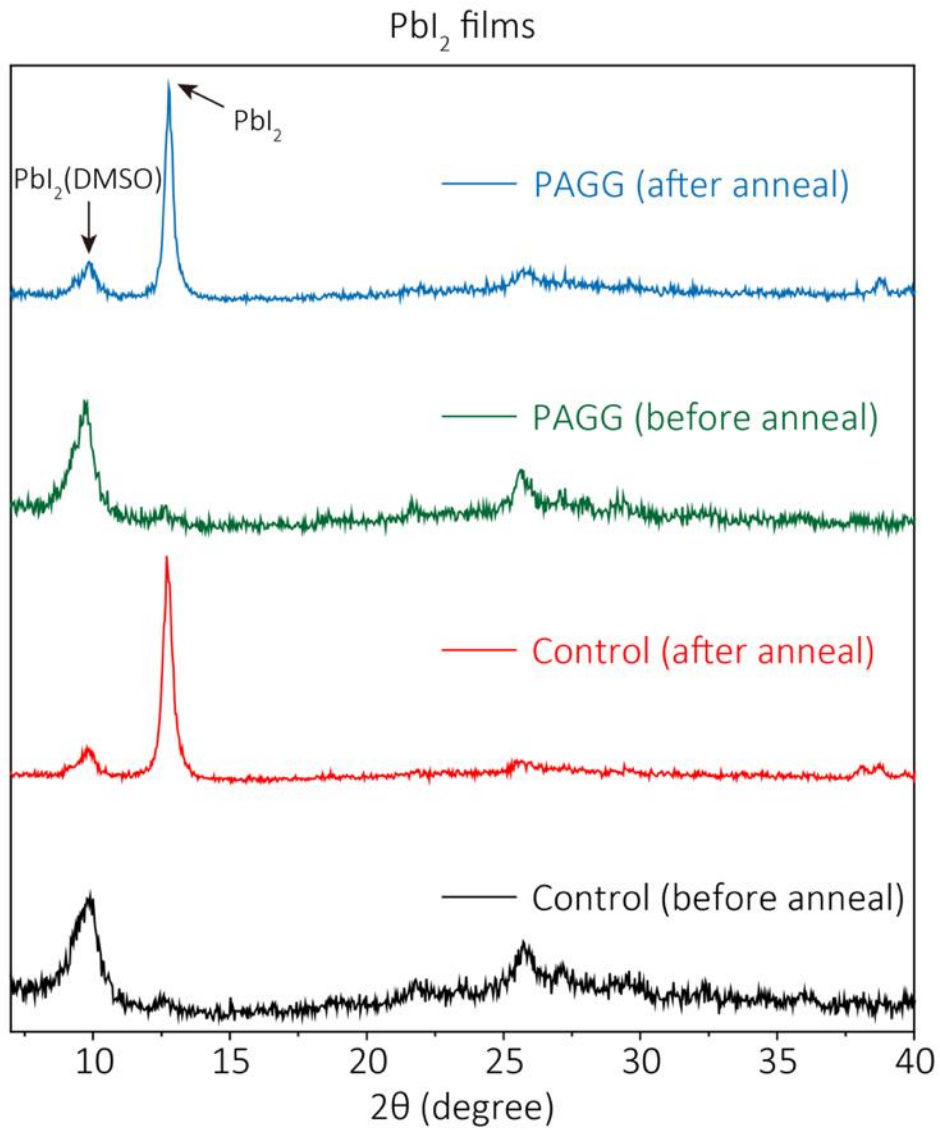


Figure A4.4. XRD spectra of control and target PbI_2 films before and after annealing.

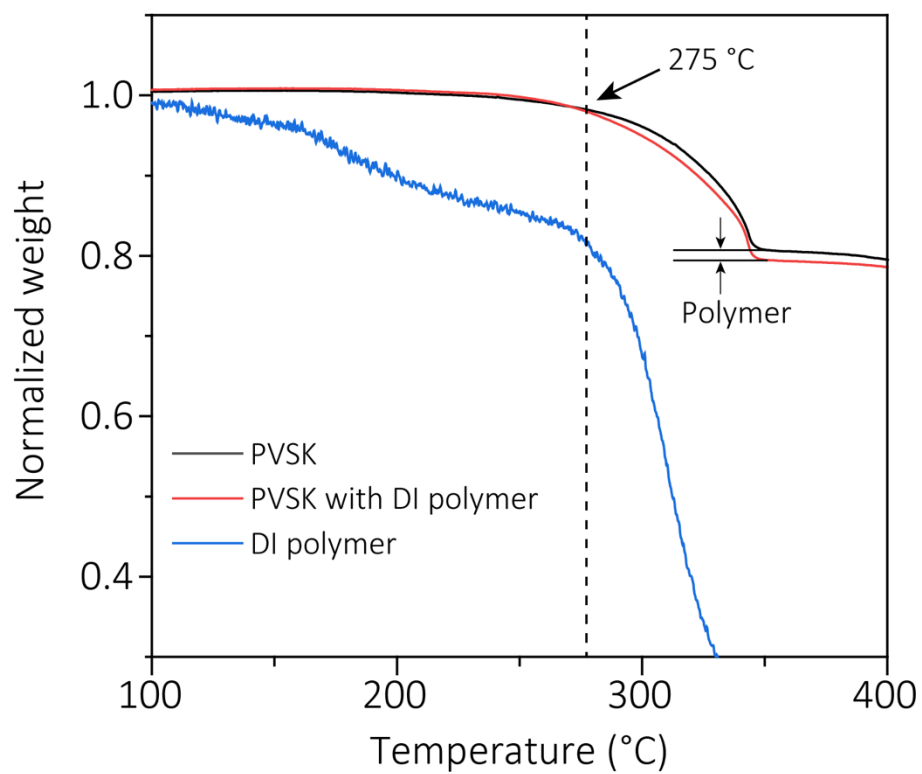


Figure A4.5. Thermogravimetric analysis (TGA) of pure DI polymer, perovskite and perovskite-DI polymer powder.

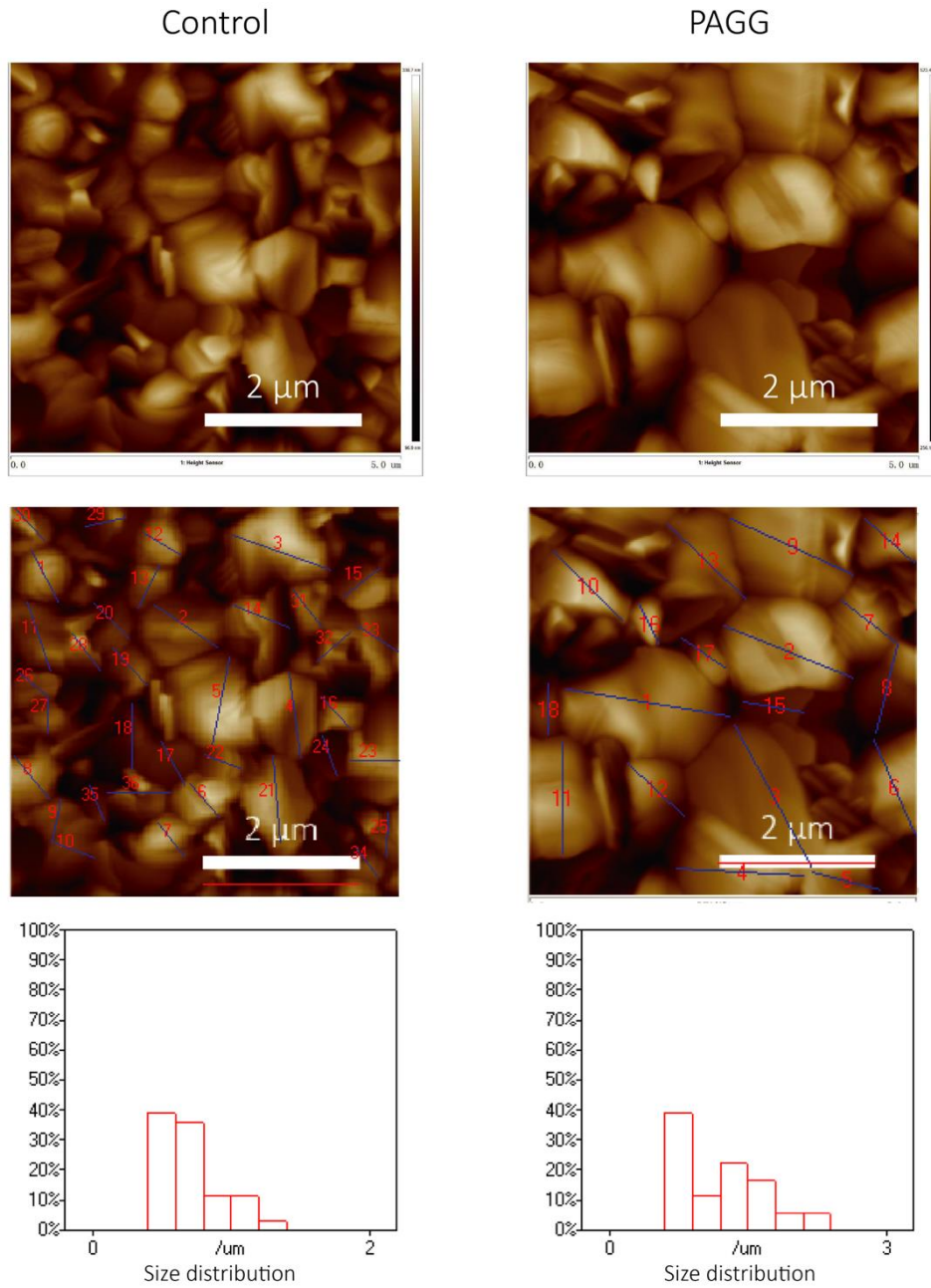


Figure A4.6. Atomic force microscope (AFM) images and size distribution of perovskite films fabricated without and with PAGG process.

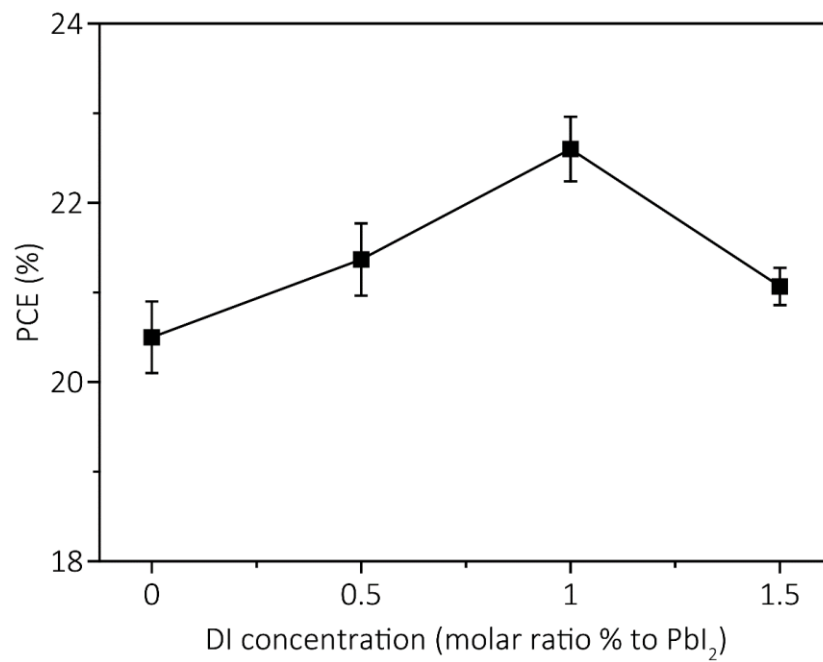


Figure A4.7. Power conversion efficiency (PCE) distribution of perovskite solar cells with different DI monomer concentrations.

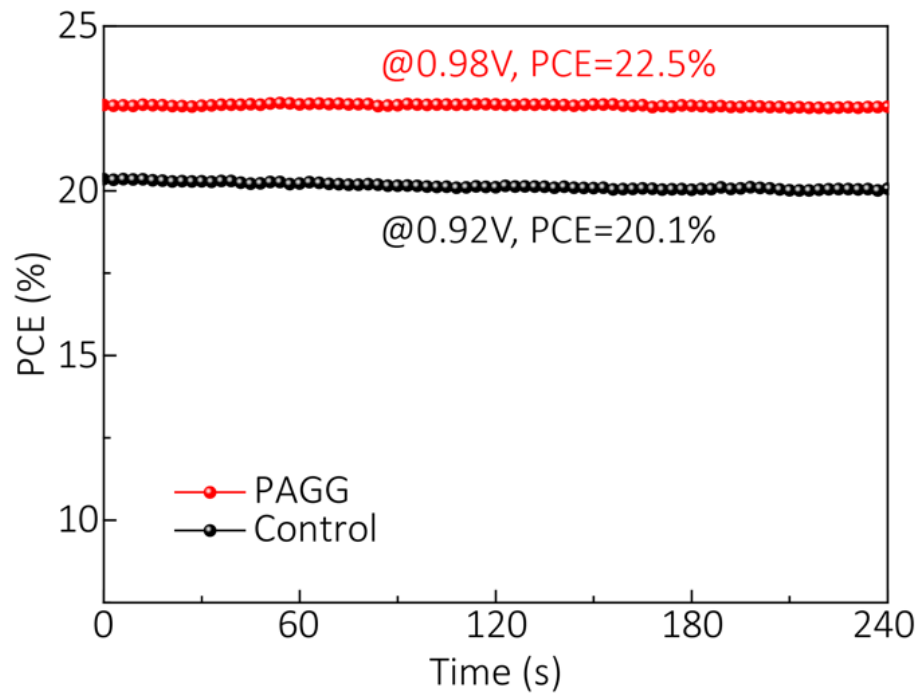


Figure A4.8. Stabilized maximum power output at maximum power point as a function of time for the best performing perovskite solar cells with or without PAGG.

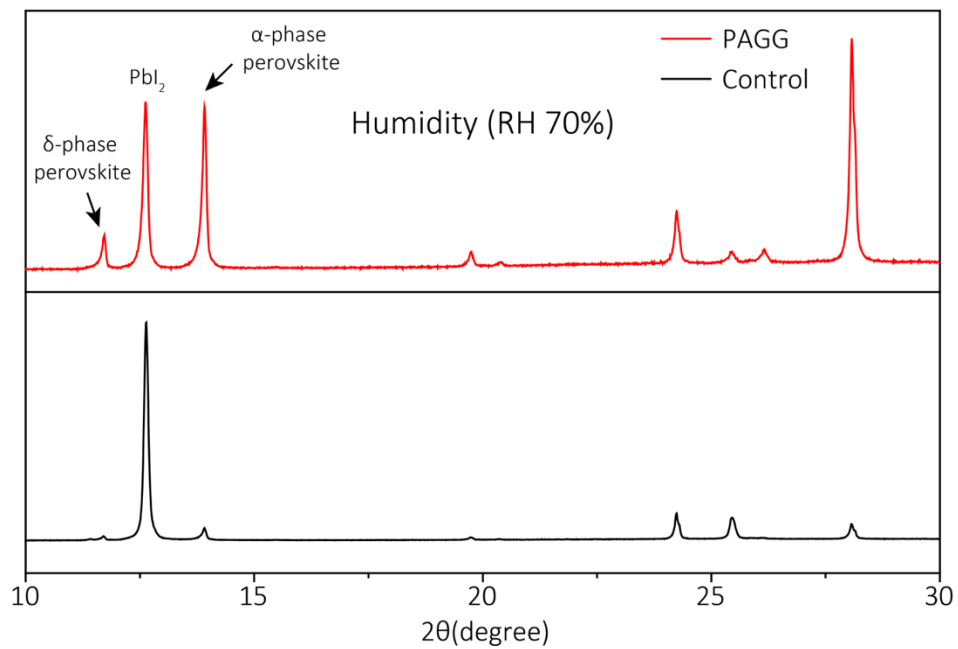


Figure A4.9. X-ray diffraction (XRD) spectra of perovskite films without and with PAGG process exposed to humidity (RH~70%) for 250 hours.

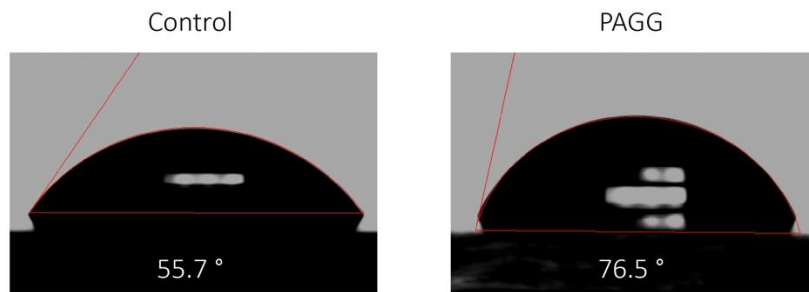


Figure A4.10. The contact angle between perovskite films (control and PAGG) and water droplets.

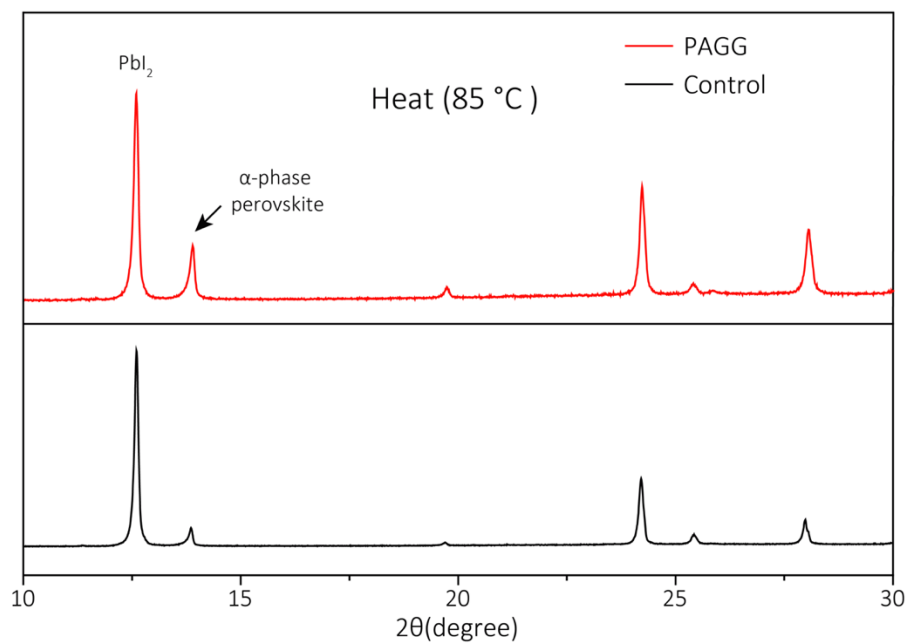


Figure A4.11. X-ray diffraction (XRD) spectra of perovskite films without and with PAGG process exposed to heat (85°C) for 350 hours.

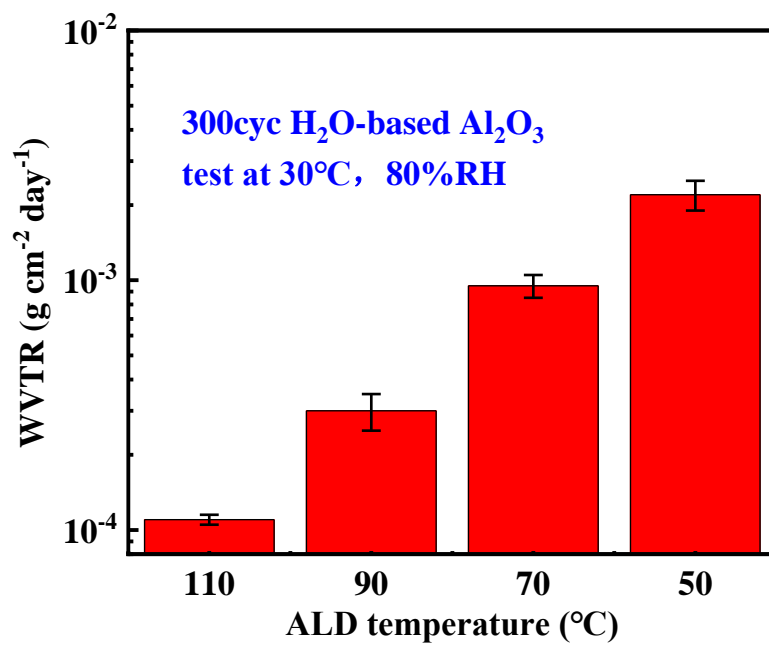


Figure A5.1. Water vapor transmission rate of atomic layer deposited Al₂O₃ film at different temperatures.

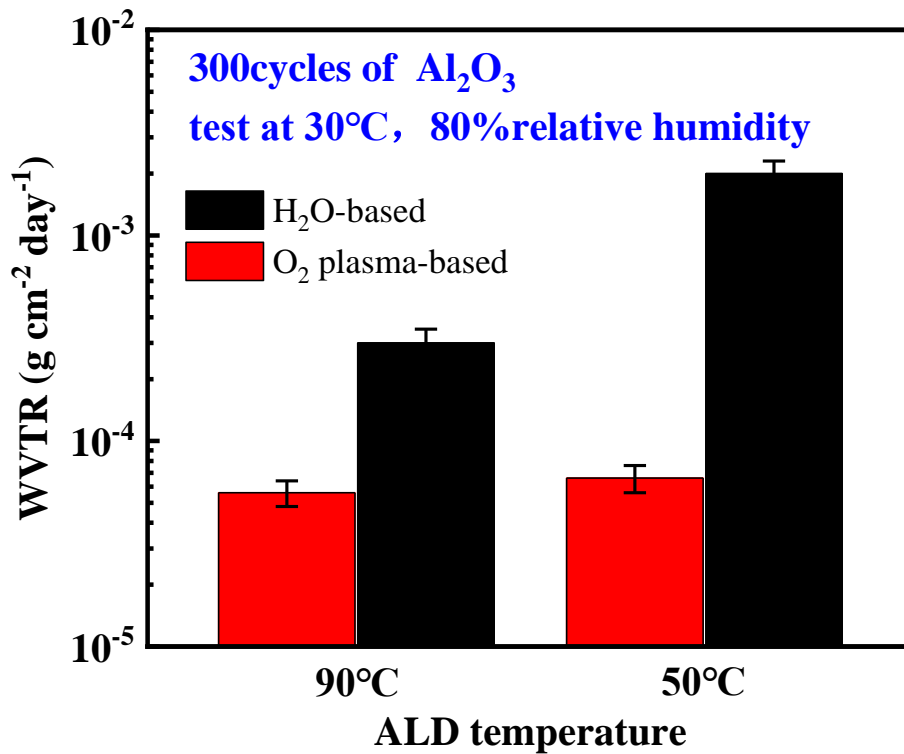


Figure A5.2. Comparison of WVTR between H₂O-based and O₂ plasma-based Al₂O₃ grown at 50 and 90 °C.

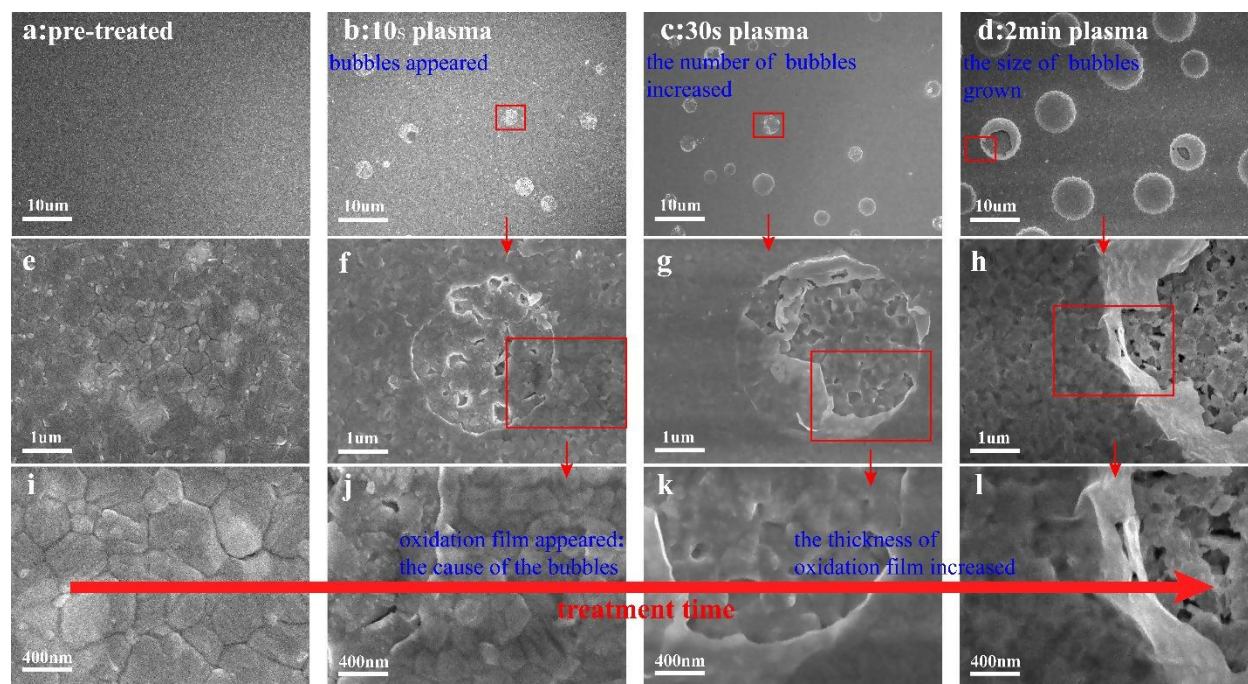


Figure A5.3. SEM images of MaPbI_3 after O_2 plasma treatment at various intervals of time.

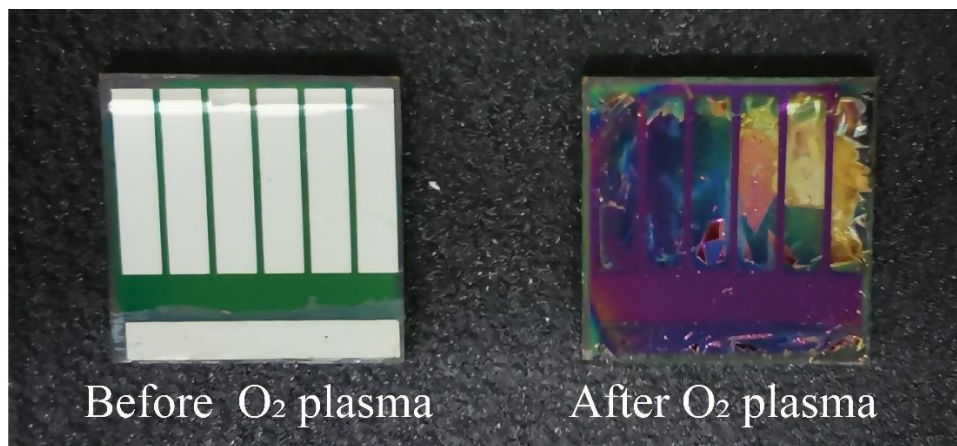


Figure A5.4. Perovskite solar cells before and after 2 minutes O₂ plasma treatment.

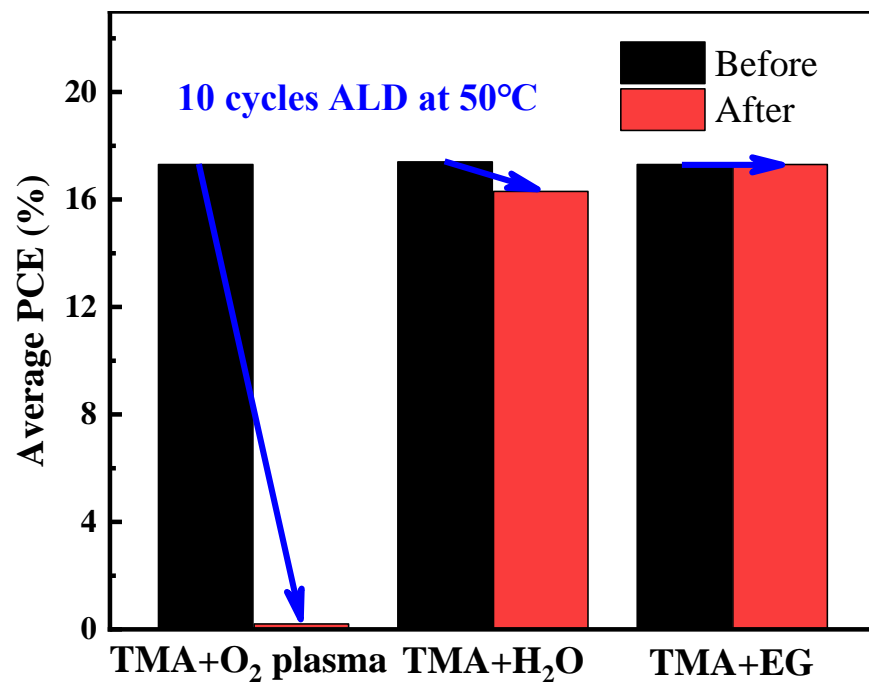


Figure A5.5. Changing of the efficiency of perovskite solar cells after PEALD Al₂O₃, H₂O-based Al₂O₃, and alucone growth at 50 °C.

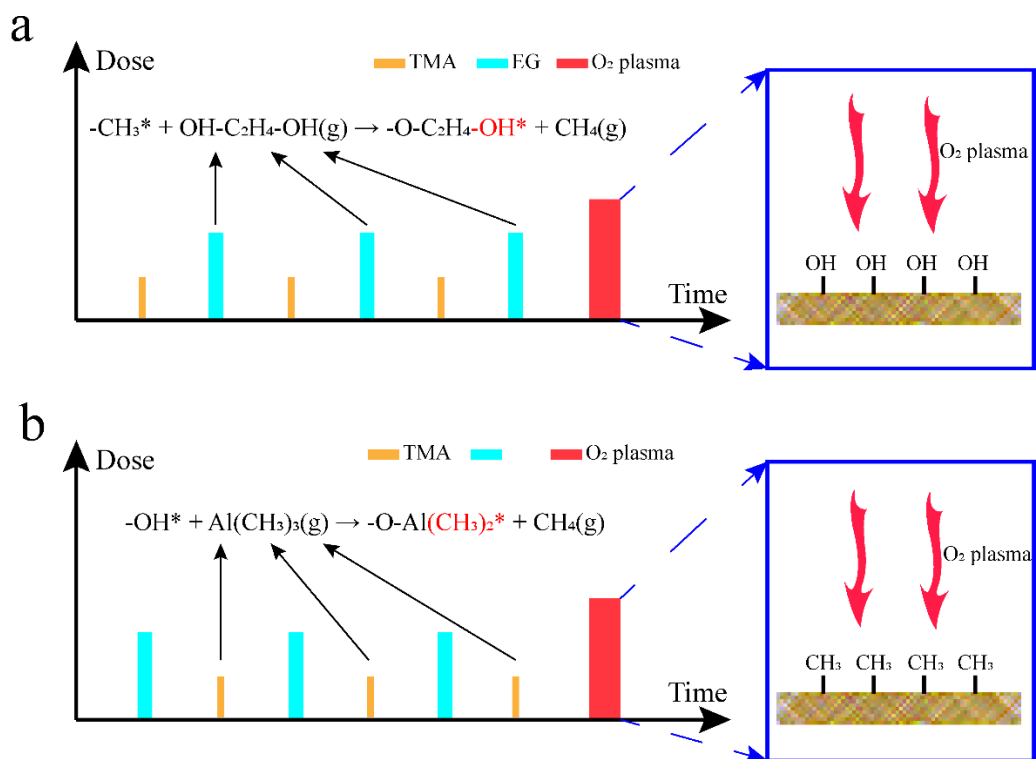


Figure A5.6. In order to avoid the interference of surface methyl groups during **a** monitoring the O₂ plasma consumption by the MLD alucone, the O₂ plasma was dosed after the EG pulse. At that moment, the substrate surface groups were hydroxyl groups which do not react with the O₂ plasma. By contrary, in the **b** actual encapsulation procedure, the O₂ plasma was dosed after the TMA pulse and reacted with the surface methyl groups. Perovskite solar cells were protected by alucone during the PEALD process.

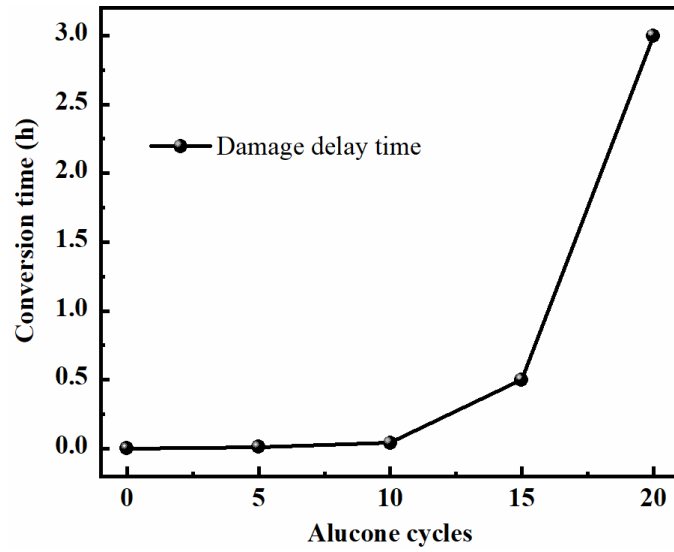


Figure A5.7. Time required for full conversion of alucone with diverse thickness. The results were determined base on the oxidation and conductivity changes of the Ag films after O₂ plasma treatment.

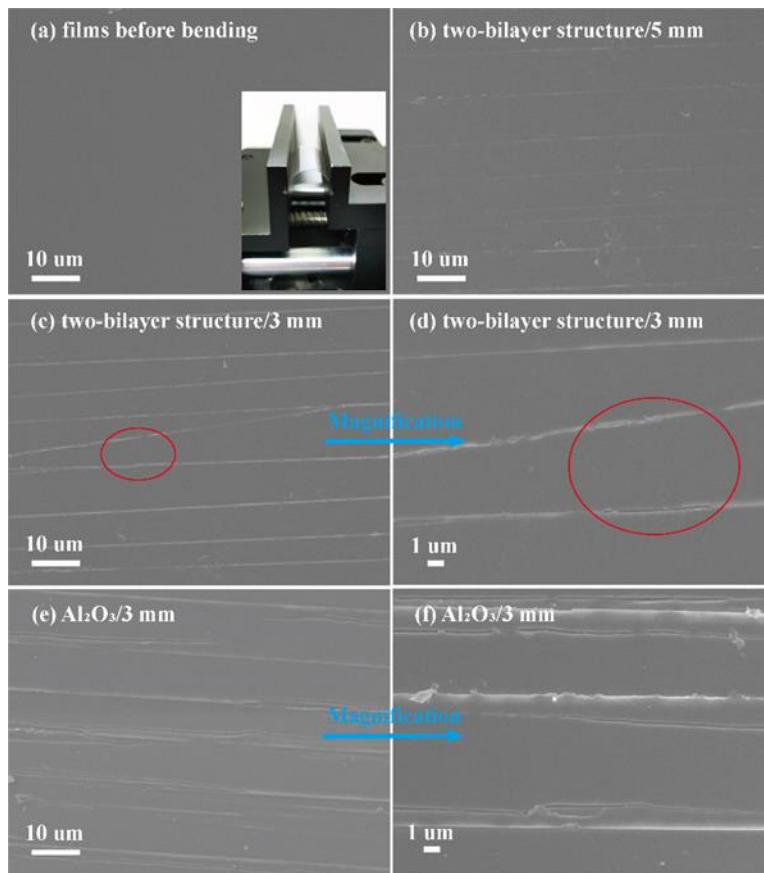


Figure A5.8. (a)-(f) SEM images of the encapsulation layers on PET substrate after 500 times of bending. The inset in (a) is the bending test machine.

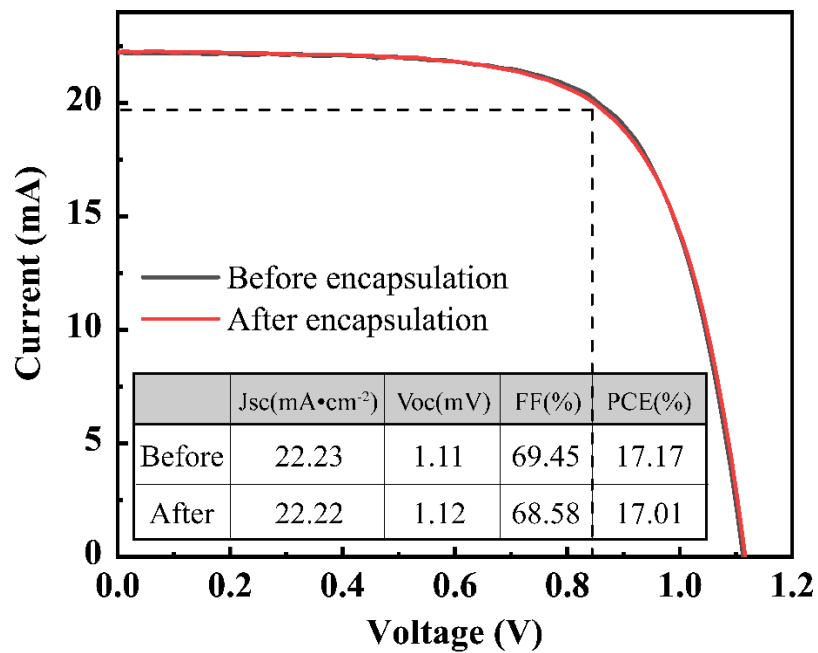


Figure A5.9. I-V curves of a represent perovskite solar cell before and after encapsulation.

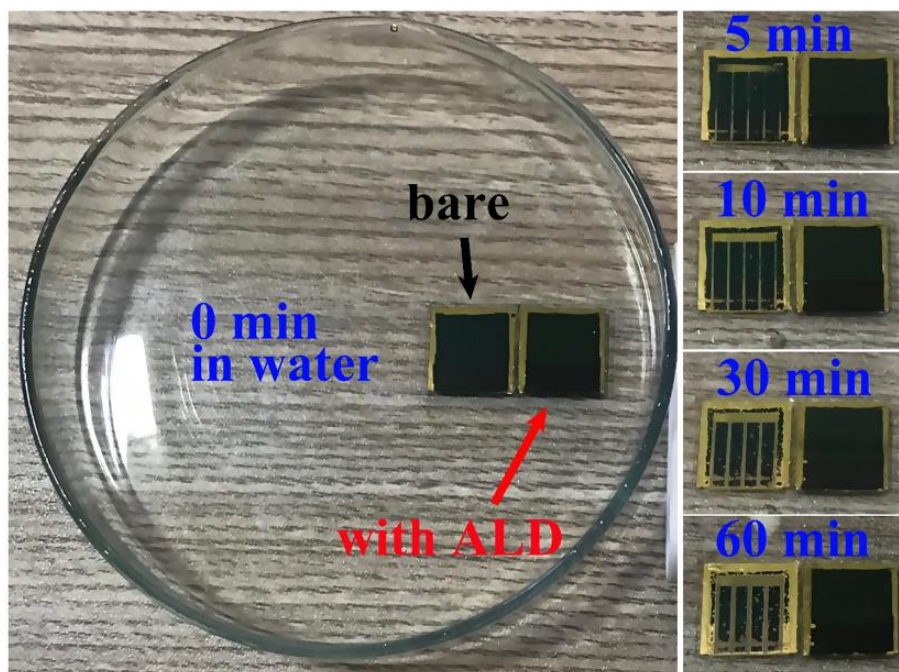


Figure A5.10. Transformation suffered by water of perovskite solar cells with and without encapsulation.

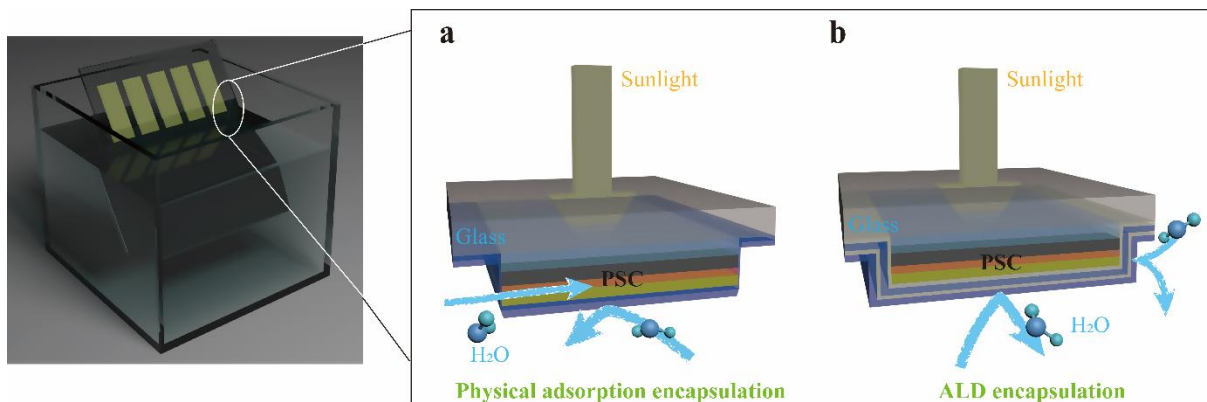


Figure A5.11. Commonly used **a** physical adsorption encapsulation, i.e. sputtering and chemical vapor deposition, showing the side penetration as in the case of the cover encapsulation. Atomic layer deposition **b** has a high conformality and ensures the growth of an efficient barrier on the side of the perovskite solar cells.

Appendix B

Table B1.1 | Fitted parameters for the data in Supplementary Fig. S1. The strain was calculated based on the function described in Supplementary Note 2.

Films	Intercept	Slope	Strain (%)
0%	0.00164	0.00501	0.125
0.08% Nd³⁺	0.00137	0.00517	0.133
0.25% Nd³⁺	0.00128	0.00590	0.148
0.45% Nd³⁺	0.00102	0.00615	0.150
1% Nd³⁺	0.00210	0.00675	0.169
2% Nd³⁺	0.00164	0.00580	0.145
5% Nd³⁺	0.00150	0.00604	0.151

Table B1.2 | Fitted parameters for the data in Supplementary Fig. S2. The strain was calculated based on the function described in Supplementary Note 2.

Films	Intercept	Slope	Strain (%)
0%	0.00164	0.00501	0.125
0.08% Ca²⁺	0.00108	0.00534	0.134
0.25% Ca²⁺	0.00102	0.00788	0.197
0.45% Ca²⁺	0.00172	0.00678	0.170
1% Ca²⁺	0.00194	0.00646	0.162
2% Ca²⁺	0.00175	0.00595	0.149
5% Ca²⁺	0.00176	0.00540	0.135

Table B1.3 | Fitted parameters for the data in Supplementary Fig. A2.3. The strain was calculated based on the function described in Supplementary Note 2.

Films	Intercept	Slope	Strain (%)
0%	0.00164	0.00501	0.125
0.08% Na³⁺	0.00122	0.00615	0.154
0.25% Na³⁺	0.00100	0.00913	0.228
0.45% Na³⁺	0.00161	0.00769	0.192
1% Na³⁺	0.00135	0.00651	0.163
2% Na³⁺	0.00119	0.0069	0.173
5% Na³⁺	0.00214	0.00637	0.159

Table B1.4 | Averaged photovoltaic parameters of perovskite solar cells with Nd³⁺ doping concentration from 0% to 0.5%.

Devices	V_{oc} (V)	J_{sc} (mA cm⁻²)	FF (%)	PCE (%)
Reference	1.101 ± 0.019	24.59 ± 0.30	75.95 ± 1.49	20.56 ± 0.45
w/ 0.02% Nd³⁺	1.136 ± 0.004	24.88 ± 0.16	77.55 ± 1.45	21.92 ± 0.43
w/ 0.05% Nd³⁺	1.141 ± 0.006	24.93 ± 0.16	80.64 ± 0.65	22.93 ± 0.24
w/ 0.08% Nd³⁺	1.164 ± 0.007	25.24 ± 0.16	79.39 ± 1.38	23.31 ± 0.28
w/ 0.1% Nd³⁺	1.154 ± 0.007	25.24 ± 0.12	79.75 ± 0.93	23.23 ± 0.34
w/ 0.15% Nd³⁺	1.147 ± 0.008	25.02 ± 0.29	78.63 ± 0.88	22.56 ± 0.19
w/ 0.2% Nd³⁺	1.129 ± 0.009	24.99 ± 0.32	77.50 ± 1.42	21.86 ± 0.37
w/ 0.25% Nd³⁺	1.135 ± 0.006	24.94 ± 0.19	77.88 ± 1.06	22.04 ± 0.31
w/ 0.3% Nd³⁺	1.131 ± 0.010	24.97 ± 0.22	77.48 ± 1.43	21.87 ± 0.28
w/ 0.35% Nd³⁺	1.124 ± 0.007	24.93 ± 0.23	76.84 ± 1.74	21.53 ± 0.44
w/ 0.4% Nd³⁺	1.125 ± 0.007	24.83 ± 0.26	77.53 ± 1.84	21.66 ± 0.61
w/ 0.45% Nd³⁺	1.120 ± 0.010	24.87 ± 0.25	76.67 ± 1.21	21.35 ± 0.37
w/ 0.5% Nd³⁺	1.113 ± 0.016	24.88 ± 0.28	75.82 ± 0.92	20.99 ± 0.42

Table B1.5 | Averaged photovoltaic parameters of perovskite solar cells with Ca²⁺ doping concentration from 0% to 0.5%.

Devices	V_{oc} (V)	J_{sc} (mA cm⁻²)	FF (%)	PCE (%)
Reference	1.101 ± 0.019	24.59 ± 0.30	75.95 ± 1.49	20.56 ± 0.45
w/ 0.02% Ca²⁺	1.116 ± 0.011	24.66 ± 0.24	75.60 ± 1.27	20.81 ± 0.45
w/ 0.05% Ca²⁺	1.125 ± 0.009	24.69 ± 0.26	76.44 ± 1.22	21.24 ± 0.53
w/ 0.08% Ca²⁺	1.125 ± 0.006	24.66 ± 0.30	77.00 ± 1.33	21.37 ± 0.45
w/ 0.1% Ca²⁺	1.133 ± 0.011	24.62 ± 0.12	76.57 ± 1.08	21.36 ± 0.22
w/ 0.15% Ca²⁺	1.130 ± 0.005	24.72 ± 0.23	77.42 ± 1.02	21.63 ± 0.42
w/ 0.2% Ca²⁺	1.137 ± 0.005	24.68 ± 0.27	77.65 ± 0.70	21.80 ± 0.39
w/ 0.25% Ca²⁺	1.152 ± 0.006	24.87 ± 0.14	77.35 ± 0.92	22.17 ± 0.40
w/ 0.3% Ca²⁺	1.149 ± 0.006	24.71 ± 0.23	77.34 ± 1.23	21.95 ± 0.29
w/ 0.35% Ca²⁺	1.130 ± 0.007	24.71 ± 0.27	77.42 ± 0.99	21.62 ± 0.32
w/ 0.4% Ca²⁺	1.127 ± 0.012	24.68 ± 0.32	77.33 ± 1.25	21.51 ± 0.49
w/ 0.45% Ca²⁺	1.122 ± 0.011	24.67 ± 0.24	76.84 ± 1.37	21.26 ± 0.43
w/ 0.5% Ca²⁺	1.116 ± 0.008	24.49 ± 0.29	76.82 ± 0.98	21.00 ± 0.39

Table B1.6 | Averaged photovoltaic parameters of perovskite solar cells with Na⁺ doping concentration from 0% to 0.5%.

Devices	V_{oc} (V)	J_{sc} (mA cm⁻²)	FF (%)	PCE (%)
Reference	1.101 ± 0.019	24.59 ± 0.30	75.95 ± 1.49	20.56 ± 0.45
w/ 0.02% Na⁺	1.114 ± 0.009	24.47 ± 0.24	76.11 ± 1.39	20.74 ± 0.36
w/ 0.05% Na⁺	1.122 ± 0.007	24.55 ± 0.41	75.83 ± 1.11	20.87 ± 0.26
w/ 0.08% Na⁺	1.124 ± 0.008	24.43 ± 0.32	77.50 ± 0.83	21.29 ± 0.37
w/ 0.1% Na⁺	1.127 ± 0.008	24.34 ± 0.33	77.04 ± 1.60	21.13 ± 0.32
w/ 0.15% Na⁺	1.125 ± 0.007	24.49 ± 0.24	76.99 ± 0.84	21.21 ± 0.29
w/ 0.2% Na⁺	1.128 ± 0.007	24.49 ± 0.26	77.36 ± 1.06	21.38 ± 0.34
w/ 0.25% Na⁺	1.132 ± 0.006	24.50 ± 0.23	77.61 ± 1.17	21.52 ± 0.34
w/ 0.3% Na⁺	1.130 ± 0.005	24.66 ± 0.19	77.93 ± 0.62	21.72 ± 0.22
w/ 0.35% Na⁺	1.137 ± 0.006	24.58 ± 0.21	77.74 ± 1.02	21.72 ± 0.19
w/ 0.4% Na⁺	1.143 ± 0.008	24.66 ± 0.15	77.49 ± 0.57	21.84 ± 0.22
w/ 0.45% Na⁺	1.146 ± 0.008	24.78 ± 0.29	77.66 ± 1.23	22.05 ± 0.18
w/ 0.5% Na⁺	1.145 ± 0.011	24.51 ± 0.20	77.67 ± 0.37	21.79 ± 0.16

Table B1.7 | Photoluminescence lifetimes and defect density of the films without or with the optimal cation doping concentrations. Corresponding photovoltaic parameters of champion perovskite solar cells with or without dopants. The PCE values in the parenthesis are the stabilized power out (SPO) of the devices.

Devices	PL				
	lifetime (μs)	V_{oc} (V)	J_{sc} (mA cm^{-2})	FF (%)	PCE (%)
Reference	1.68	1.121	24.87	76.58	21.35 (19.56)
w/ Nd^{3+}	7.75	1.173	25.38	79.55	23.68 (23.10)
w/ Ca^{2+}	5.47	1.162	25.01	78.56	22.83 (22.23)
w/ Na^{+}	4.78	1.148	24.93	77.96	22.31 (21.81)

Table B4.1. Detailed PL parameters of perovskite films with and without PAGG process.

Conditions	τ_1 (ns)	A_1 (%)	τ_2 (ns)	A_2 (%)	τ_{avg} (ns)
Control	67	24	161	76	150
PAGG	130	28	370	72	341

$$\tau_{avg}=(A_1*\tau_1^2+A_2*\tau_2^2)/(A_1*\tau_1+A_2*\tau_2)$$